

POLITECNICO DI TORINO

Collegio di Ingegneria Energetica

**Corso di Laurea Magistrale
in Ingegneria Energetica e Nucleare**

Tesi di Laurea Magistrale

Integrated modelling of fusion plasma discharges with application to the JT-60SA tokamak



Relatori

Prof. Fabio Subba

Dott. Gerardo Giruzzi

Dott. Jean-Francois Artaud

Candidata

Valeria Ostuni

Host institute:

Institut de Recherche sur la Fusion par confinement Magnetique

Commissariat à l'énergie atomique et aux énergies alternatives.

Centre de Cadarache

Ottobre 2019

Abstract

A worldwide energy shortfall is predicted within the next few decades. The nuclear energy source potential to contribute to power sector decarbonisation is significant. To make a relevant contribution worldwide, fusion should aim at generating 1TW on average of electricity respected to the predicted demand of 10TW. Therefore, at least several hundred nuclear plants have to be build during the course of the 22nd century. The pragmatic approach on fusion energy is based on a realistic demonstration that fusion is able to produce electricity. In order to reach the goal, the ITER project is the essential step towards energy production and DEMO is the single step between ITER and the commercial fusion power plant design. ITER will be the first magnetic confinement device to produce a net surplus of fusion energy. It is designed to generate 500 MW fusion power and a fusion gain of 10 (as the injected power will be 50MW). To mitigate the risk of ITER failure, JT-60SA has been designed to satisfy all of the central research needs for ITER and to prepare the physics scenarios of DEMO. In order to do that, three main scenarios (corresponding to the main scenarios of ITER) will be tested during the operation phases. Once the parameters of all the scenarios have been determined, theoretical models and simulation codes have been validated in order to establish a solid basis for the design of the scenarios. The aim of this study consists of optimizing some of the JT-60SA scenarios. This means that the values of the main parameters established for each scenarios, a discharge duration time of 100s and the respect of coils current, voltage and force limits have been reached at the same time. Integrated modelling of burning plasma is an essential task for the realization of a nuclear fusion reactor, especially for the ITER program. Therefore, for the first time, in order to reproduce a full tokamak discharge simulation, a fast integrated tokamak modelling tool for scenario design (METIS) is coupled with a quasi-static free-boundary equilibrium code (FEEQS). The first code is able to compute at each time the plasma equilibrium, the plasma current, density and pressure profiles. These outputs are given to the second code that provides the best coils currents in order to reach a given plasma shape. In this thesis, the whole process of optimization is carried on. It includes: an explication of all the codes needed for the optimization; the validation of the FEEQS code used in inverse magnetostatic mode; the results obtained running for the first time the coupled codes; the benchmark of FEEQS code used in inverse Poynting mode; the results obtained using the two codes in order to optimize the JT-60SA scenarios. The analysis is important not only to ensure a well-programmed discharge and to avoid disruption and damage to the machine, but also to find the most challenging aspects of the scenario development.

Abstract

Un deficit energetico mondiale è previsto entro i prossimi decenni. Il potenziale della fonte di energia nucleare per contribuire alla decarbonizzazione del settore energetico è significativo. Per dare un contributo rilevante in tutto il mondo, la fusione dovrebbe mirare a generare in media 1TW di elettricità rispetto una domanda predetta di 10TW. Pertanto, almeno alcune centinaia di centrali nucleari devono essere costruite nel corso del 22° secolo. L'approccio pragmatico all'energia di fusione si basa su una dimostrazione realistica che la fusione è in grado di produrre elettricità. Per raggiungere l'obiettivo, il progetto ITER è il passo fondamentale verso la produzione di energia e DEMO è il singolo step tra ITER e la progettazione di centrali elettriche commerciali a fusione. ITER sarà il primo dispositivo di confinamento magnetico a produrre un surplus netto di energia di fusione. È progettato per generare una potenza di fusione di 500 MW e un guadagno di fusione di 10 (poiché la potenza iniettata sarà di 50 MW). Per mitigare il rischio di fallimento di ITER, JT-60SA è stato progettato per soddisfare tutte le esigenze di ricerca centrali di ITER e per studiare i possibili scenari di DEMO. Per fare ciò, tre scenari principali (corrispondenti ai tre scenari di ITER) saranno testati durante le fasi operative. Una volta che i parametri di tutti gli scenari saranno stati decisi, i modelli teorici e i codici di simulazione dovranno essere convalidati al fine di stabilire una base solida per gli scenari sperimentali. Lo scopo di questo studio è ottimizzare alcuni degli scenari di JT-60SA. Ciò significa che i valori dei principali parametri stabiliti per ogni scenario, una scarica di plasma di 100 s e il rispetto dei limiti delle correnti dei magneti vengono raggiunti contemporaneamente. La modellizzazione integrata per la scarica del plasma è un aspetto essenziale per la realizzazione di un reattore a fusione nucleare, in particolare per il programma ITER. Pertanto, per la prima volta, al fine di riprodurre un'intera simulazione di scarica di tokamak, un codice veloce di modellazione integrata per la progettazione di scenari (METIS) è accoppiato con un codice quasi-statico di equilibrio magnetico a frontiera libera (FEEQS). Il primo codice è in grado di calcolare per ogni passo temporale il profilo di equilibrio del plasma, la densità di corrente e la pressione del plasma. Questi dati in uscita sono passati al secondo codice, che fornisce le migliori correnti nei magneti per raggiungere una data forma del plasma. In questa tesi, l'intero processo di ottimizzazione eseguito viene descritto. Questo include: una spiegazione di tutti i codici necessari per l'ottimizzazione; la validazione del codice FEEQS utilizzato in modalità magnetostatica inversa; i risultati ottenuti eseguendo per la prima volta i codici accoppiati; la validazione del codice FEEQS utilizzato in modalità Poynting inversa; i risultati ottenuti usando i due codici al fine di ottimizzare gli scenari di JT-60SA. L'analisi è importante non solo per garantire una scarica ben controllata ed evitare disruzioni e danni alla macchina, ma anche per trovare i punti più difficili dei futuri scenari sperimentali.

Index

1. Introduction

1.1 need for fusion energy	5
1.2 What is a tokamak?	6
1.3 The way for fusion	10
1.4 JT-60SA	12
1.5 Scenarios and objectives	14

2. Codes for integrated tokamak modelling

2.1 Reconstruction of plasma equilibrium	19
2.2 CRONOS code	22
2.3 METIS code	23
2.4 FEEQS code	29

3. Case of Study

3.1 FEEQS in inverse magnetostatic mode plasma breakdown	33
3.2 METIS and FEEQS for JT-60SA operational scenarios	38
3.3. Operational Scenario	56
3.3.1. Scenario #2	68
3.3.2. Scenario #4-2	86

4. Conclusion 100

Bibliography 102

1. Introduction

1.1 Need for fusion energy

A worldwide energy shortfall is predicted within the next few decades due to the combination of steadily increasing demand and decreasing available energy sources. This shortfall must be covered by alternative sources of energy. Energy sources available referred to 2005 with advantages and disadvantages are listed in figure 1.1. [\[1\]](#)

Energy Source	Availability	Advantages	Disadvantages
Coal	220 years	<ul style="list-style-type: none"> Abundant 	<ul style="list-style-type: none"> Burns dirty Causes acid rain, air pollution, CO₂
Oil	35 years	<ul style="list-style-type: none"> Flexible fuel source with many derivatives 	<ul style="list-style-type: none"> Finite supply Causes air pollution, Produces CO₂
Natural Gas	60 years	<ul style="list-style-type: none"> Burns cleanly 	<ul style="list-style-type: none"> Finite supply Produces CO₂
Fission	45 years (2,700 years-breeder)	<ul style="list-style-type: none"> Transportable Clean, no CO₂ Does not produce immediate pollution 	<ul style="list-style-type: none"> Waste disposal is difficult Safety concerns
Hydroelectric	Mostly utilized	<ul style="list-style-type: none"> Clean, no CO₂ 	<ul style="list-style-type: none"> Dam construction destroys habitats Geographically limited
Wind	Low utilization	<ul style="list-style-type: none"> Clean, no CO₂ 	<ul style="list-style-type: none"> Large numbers of windmills required for adequate power generation Geographically limited
Geothermal	Low utilization	<ul style="list-style-type: none"> Clean, no CO₂ 	<ul style="list-style-type: none"> Geographically limited
Solar	Underutilization	<ul style="list-style-type: none"> Clean, no CO₂ 	<ul style="list-style-type: none"> Large number of solar cells required for adequate power generation Geographically limited

Figure 1.1 - First column lists the existing energy sources. Second column shows the availability of each resources. The third and the last column reports advantages and disadvantages of sources respectively. [\[1\]](#) The number given in the table referred to fission energy source does not take into account the thorium/U233 cycle, therefore the availability is more than 2.700 years-breeder. [\[2\]](#)

The solution to the energy problem can come by a portfolio of options that includes improvements in energy efficiency, renewable energy, nuclear energy and carbon capture techniques.

Figure 1.2 shows a projected electricity production and contribution by different existing technologies in 2050 according to scenarios 6°C (6DS) and 2°C (2DS) increases in the global temperature. All of the predicted scenarios show a large and essential growth in low-carbon generation. [\[3\]](#)

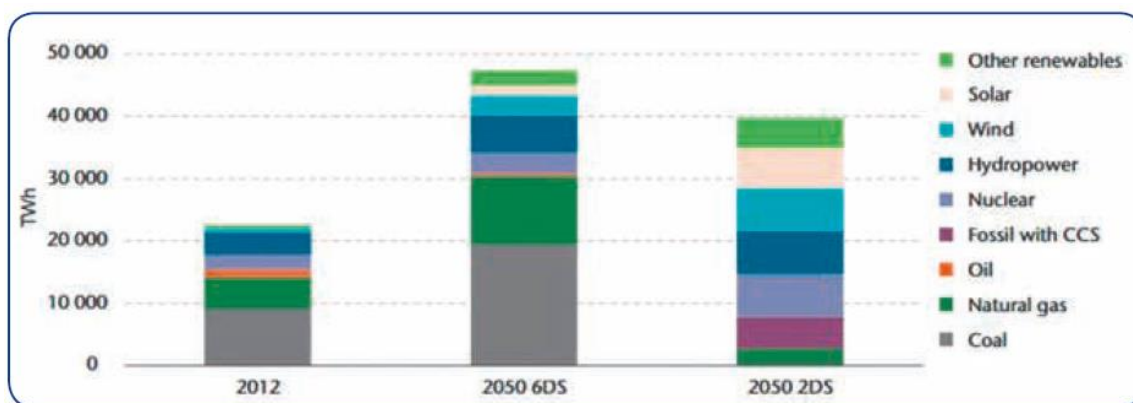


Figure 1.2 - First graph shows the actual electricity production; the other two graphs represent the predicted electricity production up to 2050 for scenarios 2DS and 6DS compared to present energy production. [\[4\]](#)

Although renewable energy sources such as solar, wind and geothermal energy are attractive from an ecological point of view, they are not able to produce the necessary energy production density. As the potentials of hydro, biomass or geothermal energy are limited in many countries, wind power and solar photovoltaics (PV) play an increasing role. However, the main problem of the renewable energy is due to their intermittent availability and the difficulty to store electricity. In fact, electricity generation from wind and solar PV plants is variable and it depends on exogenous weather conditions, the time of day, season, and location. In addition, the potential temporal mismatch of supply and demand raises two fundamental questions: how to deal with variable renewable energy at times when there is too much supply, and how to serve demand at times when supply is scarce. [5] If suitable storage methods can be advanced, intermittent renewable energy sources, hydro and geothermal power can replace fossil fuels in a sustainable energy grid. Economically viable storage of energy requires conversion of electricity and storage in some other energy form, which can then be converted back to electricity when needed. [6]

At the same time, fission-based nuclear power has historically been one of the largest contributors of carbon-free electricity globally. Their potential to contribute to power sector decarbonisation is significant. In many jurisdictions nuclear power has trouble competing against other, more economic alternatives, such as natural gas or modern renewables. [7] Concerns over safety and broader public acceptance also remain an obstacle to development. However, to make a relevant contribution worldwide, fusion should aim at generating, for instance, ~10% of the world expected electricity demand, say 1TW of electricity on average. This would typically correspond to several hundred fusion plants available worldwide in the course of the 22nd century. [4] It is not mentioned in the figure 1.1 since it is not yet a commercially available energy source, but a fusion-power nuclear reactor would offer significant advantages. In particular, fusion needs hydrogen isotopes to work and the abundance of this lead to a negligible fuel supply problem. Fusion would produce no air pollution or greenhouse gases during normal operation. The risk of accident for a fusion reactor is much lower than for fission reactor and in particular the risk to have external contamination. This is mainly due to the negligible residual power during the shutdown of the reactor and low inventory of radioactive combustible. In addition, radioactive materials produced can be safely disposed and all the materials used could be reassembled in another future plant after a few decades. Hence, for these reasons, many techniques have been studied in various parts of the world to develop this kind of energy source and to make fusion a credible energy option. [1]

1.2 What is a tokamak?

In a fusion reaction a deuterium nucleus (one proton and one neutron) and a tritium nucleus (one proton and two neutrons) combine to form a helium nucleus (two protons and two neutrons) and a free energetic neutron (14.1MeV), while producing excess heat because of the thermalisation of the helium nucleus energy by collisions with nuclei and electrons of the deuterium-tritium mixture. The excess heat sustains additional fusion reactions, while the energy of the free neutrons can be converted into heat and then into electrical energy. Figure 1.3 shows a typical fusion reaction that can occur in a fusion reactor.

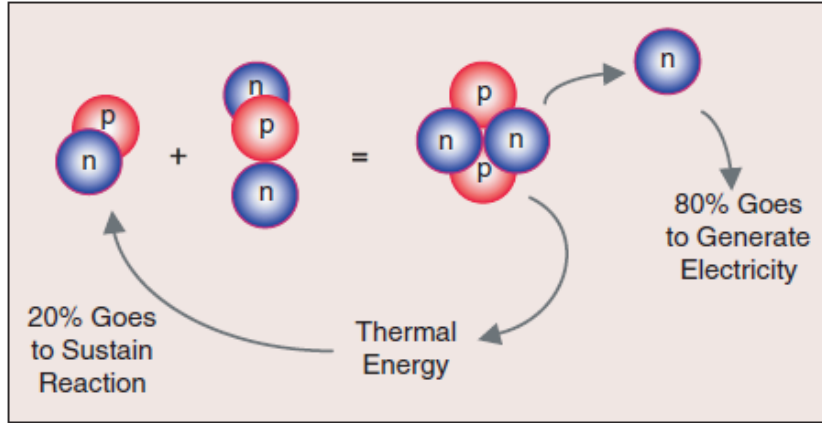


Figure 1.3 - Typical fusion reaction occurring into a tokamak. A deuterium nucleus combines to a tritium nucleus to form a helium nucleus and an energetic neutron. The 20% of the thermal energy produced is used to sustain the reaction, while the other part is used to generate electricity. [3]

Deuterium is widely available, while tritium exists only in tiny quantities. It is possible to produce it through the reaction between a neutron and a lithium nucleus. Also the lithium is abundant on Earth.

Atomic nuclei are positively charged and so they repel each other. The only possibility to fuse is colliding so fast to overcome the repelling Coulomb force. This is the reason why the fusion fuel has to be heated to about 200 million of degrees. At this temperature, atoms are split into nuclei and electrons forming a gas of charged particles known as plasma. [3]

Other possible fusion reactions could be used to generate energy (see figure 1.4), but they require so higher temperatures their use would result impractical with present technologies.

Reagents			Products			
${}^2_1\text{D}$	+	${}^3_1\text{T}$	\longrightarrow	${}^4_2\text{He}$ (3.5 MeV)	+	${}^1_0\text{n}$ (14.1 MeV)
${}^2_1\text{D}$	+	${}^2_1\text{D}$	\longrightarrow	${}^3_1\text{T}$ (1.01 MeV)	+	${}^1_1\text{p}$ (3.02 MeV)
			\longrightarrow	${}^3_2\text{He}$ (0.82 MeV)	+	${}^1_0\text{n}$ (2.45 MeV)
${}^2_1\text{D}$	+	${}^3_2\text{He}$	\longrightarrow	${}^4_2\text{He}$ (3.6 MeV)	+	${}^1_1\text{p}$ (14.7 MeV)
${}^1_1\text{p}$	+	${}^6_3\text{Li}$	\longrightarrow	${}^4_2\text{He}$ (1.7 MeV)	+	${}^3_2\text{He}$ (2.3 MeV)
${}^1_1\text{p}$	+	${}^7_3\text{Li}$	\longrightarrow	$2{}^4_2\text{He}$ (17.3 MeV)		
			\longrightarrow	${}^7_4\text{Be}$	+	${}^1_0\text{n}$ - (1.6 MeV)
${}^1_1\text{p}$	+	${}^{11}_5\text{B}$	\longrightarrow	$3{}^4_2\text{He}$ (8.7 MeV)		

Figure 1.4 - Main reaction of nuclear fusion: the problem of the second reaction is related to the production of ${}^3_1\text{T}$ that is radioactive; the third reaction is difficult to obtain due to the absence of ${}^3_2\text{He}$ of the earth and, in addition, it is not completely aneutronic due to the parasitic D+D reaction; a $p+{}^7_3\text{Li}$ has the cross section too low; $p+{}^{11}_5\text{Be}$ reaction is completely aneutronic and will be the best one from the point of view of radioactivity but is very difficult to use due to the high plasma temperature required (~ 250 keV).

The primary challenge of fusion is to confine this ionized gas while it is heated up and its pressure increases, in order to initiate and sustain fusion reactions. There are three ways to confine the plasma: gravitational confinement, typical of the stars, inertial confinement and magnetic confinement.

Nowadays, the last method is the most promising one and it has led to the tokamak machine concept. In a tokamak, the magnetic fields produced by currents in large coils are used to confine the charged particles into a fixed volume. In fact, ions and electrons follow a magnetic field line, and are forced by the Lorentz force to follow a helical trajectory. As the force acts only in the perpendicular plane (with respect to the magnetic field), in the parallel direction the particle is free to move. For this reason, the best way to enclose the field lines is to create a toroidal geometry. The currents in external coils that surround the toroidal chamber generate a toroidal magnetic field. However, this is not sufficient to confine the particles that would drift vertically. Therefore, other coils are placed in the center of the tokamak, acting like the primary of a transformer, where the secondary circuit is the plasma itself. The Ohmic current induced in the plasma (which has a finite resistance), generates an additional magnetic field, called poloidal field. These two magnetic fields produce helical magnetic field lines that provide a path for the plasma particles, which tend to remain in the torus (see figure 1.5). The plasma is contained in a vacuum vessel. It is created by letting in a small puff of gas, which is then heated by driving a current through it.

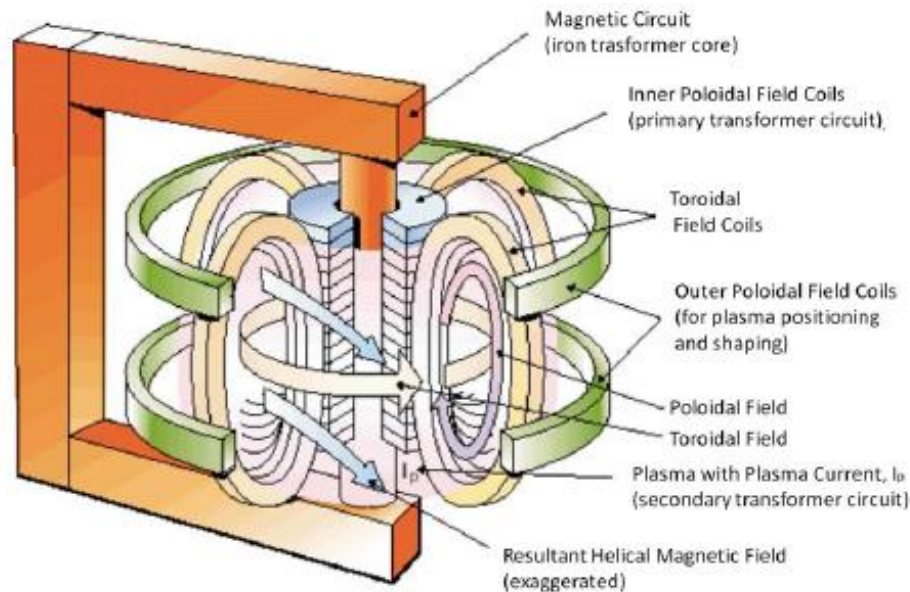


Figure 1.5 - Main tokamak components. Poloidal and toroidal field coils, together with the plasma current, generate a spiraling magnetic field that confines the plasma. [\[8\]](#)

At present, existing tokamaks are pulsed devices, so the plasma is maintained for only a few seconds to several minutes. The main parameters of a typical discharge are shown in figure 1.6 and are characterized by a well defined sequence of events. The time duration of the discharge corresponds to the time in which the plasma is present in the tokamak. The toroidal field coil current is brought up early in order to create a constant magnetic field to confine the plasma when it is initially created. Also the deuterium gas is puffed into the plasma chamber before plasma forming. At $t=0$, the ohmic heating coil current is driven down in order to produce a large electric field within the torus, able to accelerate free electrons which collide and produce the ionized plasma. Collisions between electrons

and ions cause the plasma to be resistive, which causes the plasma to heat due to Joule's effect (Ohmic heating). The central solenoid supplies magnetic flux and it is used to control the ramp-up of the plasma current until the reaching of the flattop level. The separate time intervals in which the plasma current is increasing, constant and decreasing are named as ramp-up, flat-top and ramp-down phases.

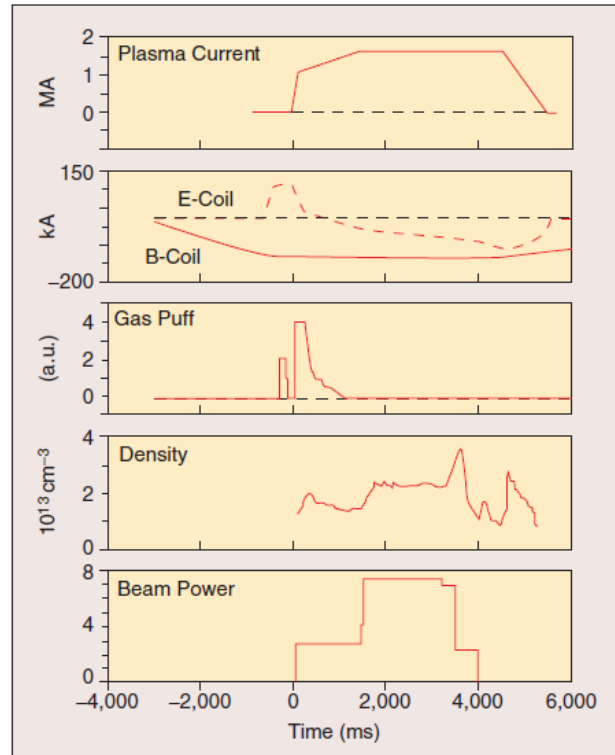


Figure 1.6 - Typical tokamak plasma discharge: plasma current is initiated and sustained by the ohmic heating coil, while the toroidal field coil provides the primary magnetic field for confinement. Deuterium gas is puffed into the containment vessel near the beginning of the discharge to provide the fuel needed to form the plasma. Neutral beams used to heat the plasma have the side effect of introducing additional deuterium into the vacuum chamber. [9]

Plasma behaves like a perfect gas, so its pressure P is proportional to the product of density and absolute temperature. However, the plasma is not homogenous, in fact it is hotter and denser in the center than in the external region.

A main problem is related to the plasma heating because the ohmic heating is not sufficient. In fact, as the electron temperature increases, the plasma resistance decreases and the ohmic heating becomes less and less effective. A frequently used method is the injection of a beam of neutral particles (NBI). These particles are able to cross the magnetic field lines and penetrate into the plasma. Colliding with particles already present, they ionize and at the same time increase the plasma temperature. The ions are produced in the plasma source. After extraction, they are accelerated to a high energy before crossing a charge exchange cell where they are neutralized. The neutralization is only partial and the remaining ions are deflected magnetically and sent to a dump. There are two types of NBI depending on the particle charge that is used for their acceleration: positive-NBI (P-NBI) and negative-NBI (N-NBI). When ions cross the neutralization cell, each one has a neutralization probability that increases with the length of the neutralization gas cell. At energies higher than 100keV, neutralization efficiency for positive ions is lower than 50% and falls under 10% at energies

of 300keV. While negative ions have efficiency almost constant of 65% through all energies between 100keV and 2MeV. This is because of the cross section for losing electron through collisions. N-NBI is schematically equal to P-NBI. Nevertheless, there are some principal differences between them, because the ion source must produce negative ions, which is harder to do, and N-NBI operate at much higher energy. [\[10\]](#)

Another method is radio-frequency (RF) heating or electromagnetic (EM) waves with a frequency able to excite plasma resonances with electrons (electron cyclotron resonance heating: ECRH) or with ions (ion resonance heating). [\[9\]](#) Since there are two main species in the plasma and the two resonance frequencies differ by inverse of the square root of the mass, the frequency ranges from radio frequency to microwave. The ion cyclotron frequency falls within the RF range (approximately 40–500 MHz) and the electron cyclotron frequency falls within the microwave range (approximately 50–300 GHz). For the ion cyclotron heating, once the resonance characteristics in the machine are identified, one can design a transmission line and an appropriate launching antenna to be located close to the edge of the plasma. For electron heating in the plasma, the fundamental and second harmonic electron resonance frequencies that fall within the microwave range for magnetic fields ranging from approximately 1 T to 5 T are used. ECH is very effective and coupling is simple, since the launcher system requires only a small area relative to the large antenna area required for ICRH heating. [\[11\]](#) Also the lower hybrid resonant frequencies (LH) belong to RF heating. They consist of an hybrid of electron and ion cyclotron resonance heating and they lie between 1 and 8 GHz.

1.3 The way for fusion

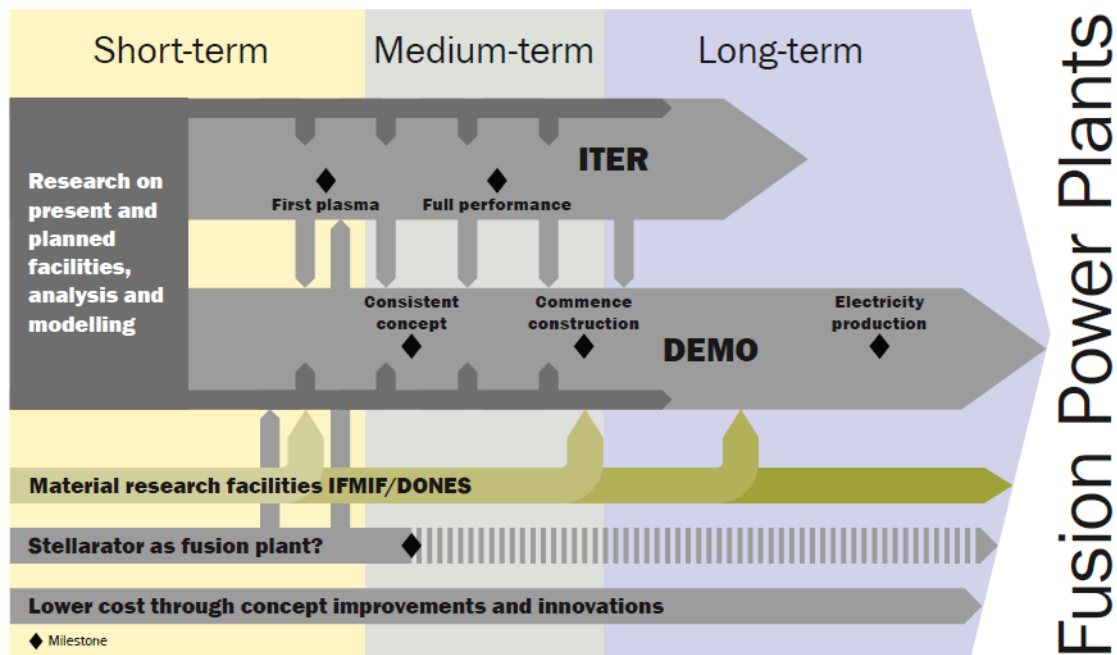


Figure 1.7 - EU strategy to achieve a fusion power plant. [\[4\]](#)

The pragmatic approach on fusion energy is based on a realistic demonstration that fusion is able to produce electricity. In order to reach the goal three main elements are necessary:

- The ITER project as the essential step towards energy production;
- A single step between ITER and the commercial fusion power plant design, DEMO;
- The International Fusion Materials Irradiation Facility (IFMIF) for materials qualification under intense neutron irradiation.

ITER is the key facility of the fusion energy. ITER will be the first magnetic confinement device to produce a net surplus of fusion energy. It is designed to generate 500 MW fusion power for discharges lasting ~400 s. As the injected power will be 50MW, this corresponds to a fusion gain $Q=10$. ITER will also demonstrate the main technologies for a fusion power plant. It is currently being built in Cadarache (France), in the framework of a collaboration between China, Europe, India, Japan, Korea, Russia and the USA. [3]

The milestones for ITER and the related EU strategy are explained in *The European Research Roadmap to the Realization of Fusion Energy* (Ref [4]). The roadmap is based on eight missions and the Mission 1 and 2 are in particular connected to the tokamak program.

Mission 1 is based on the tokamak configuration and has to provide the basis for plasma regimes of operations. ITER has to achieve the headline missions of $Q=10$ (inductive regime) and $Q=5$ (steady-state regime). In order to mitigate the risk of ITER failure, accompanying scientific programmes on small and medium sized tokamaks are necessary. In addition, two very large tokamaks (still smaller than ITER) are or will be exploited in the framework of the EU fusion research: JET, the Joint European Torus located at the Culham Center near Oxford, is used to validate the inductive regimes and operation with D-T, while JT-60SA, located at the Naka Fusion Institute in Japan (but jointly funded and exploited by Japan and EU), is mainly devoted to steady-state regimes.

Mission 2 consists of reducing the heat load on the divertor targets by radiating a sufficient amount of power from the plasma and by producing “detached” divertor conditions. A dedicated test on specifically upgraded existing facilities or on a dedicated Divertor Tokamak Test (DTT) facility will be necessary.

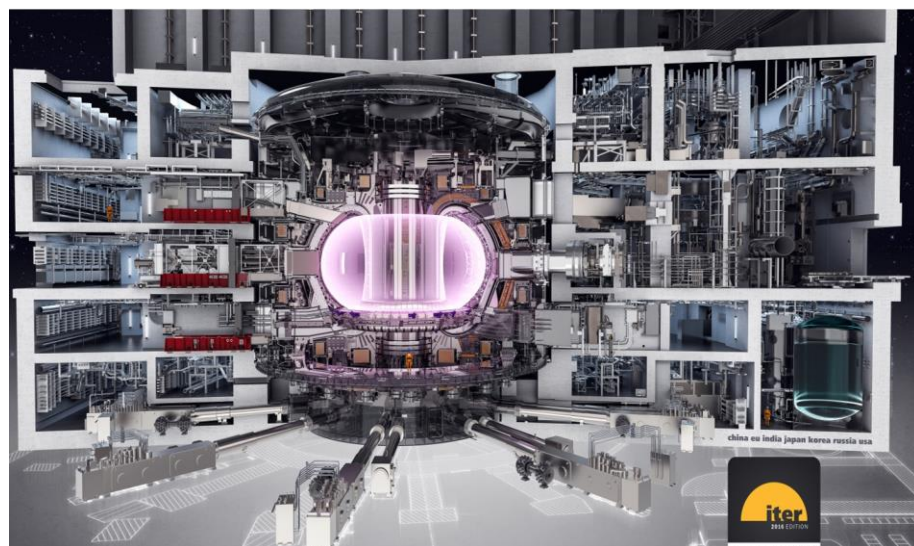


Figure 1.8 - design of ITER.

1.4 JT-60SA

JT-60SA is a superconducting tokamak under construction in the Naka Fusion Institute of the National Institute of Quantum and Radiological Science and Technology. [13] It will support the ITER experimental program realizing a stable steady-state operation. In order to achieve this objective disruptions have to be avoided and mitigated, ELMs have to be controlled and a radiative divertor is installed to reduce the heat load. Disruptions consists of rapid losses of a large fraction of the plasma thermal energy due to uncontrolled growth of some large-scale plasma instability. In most case, they lead to complete termination of the plasma current and therefore of the discharge. [14] The edge localized modes (ELMs) are periodic fast collapse of the edge pressure that lead to a sudden loss of the confinement and a subsequent release of heat and particles onto plasma facing component. They are a consequence of the discovery of the High confinement mode (H-mode). This particular regime is characterized by the formation of a transport barrier at the edge of the plasma. It creates a strong pressure gradient called the edge pedestral. H-mode increases the plasma energy confinement time by around a factor of 2 compared to Low confinement time (L-mode) and this is the reason why H-mode is chosen for the future facilities. [15]

Moreover, JT-60SA will provide key information for the design of DEMO scenarios that should be operated in a higher normalized beta regime ($\beta_N = \beta \frac{aB_T}{I_p} \sim 4 - 5$, where $\beta = \frac{\langle p \rangle}{\frac{B^2}{2\mu_0}}$, $\langle p \rangle$ is the mean plasma pressure, B the mean toroidal field, a is the minor radius, B_T the toroidal magnetic field and I_p the plasma current).

Therefore, JT-60SA has several characteristics to guarantee flexible operation in a wide range of plasma parameters. One of them is the value of the shape factor $S = \frac{q_{95}I_p}{aB_t}$ which quantifies the shaping of the plasma cross section. Other parameters are reported in the table 1.1.

Table 1.1 - Main parameters of JT-60SA. [16]

Parameter	Value
Plasma current (I_p)	5.5 MA
Toroidal field (B_T)	2.25 T
Major radius (R)	2.96 m
Minor radius (a)	1.18 m
Plasma volume (V_p)	133 m ³
Elongation (k)	1.95
Triangularity (d)	0.53
Aspect ratio (A)	2.5
Shape parameters (S)	6.7
Flattop duration	100 s
Heating and current drive power	41 MW

N-NBI	10 MW
P-NBI	24 MW
ECRH	7MW
Tolerable divertor heat load	15 MW m ⁻²

The magnetic system of JT-60SA is composed by 18 toroidal field coils (TF), 6 poloidal equilibrium field coils (EF) and 4 identical central solenoid coils (CS) (see figure 1.9). TF coils have a height of 7.4 m, a width of 4.5, are fabricated in NbTi strand with a rectangular shaped steel-jacketed NbTi cable in conduit conductors (CICC). One conductor is wound to form one D-shaped double pancake, six pancakes together form a winding pack that is enclosed in a coil casing. The EF coils are made of NbTi CICC and have different sizes: EF1 outer diameter of 12 m, EF2 9.6m, EF3 4.4m (located in the upper mid-plane), EF4 4.4 m, EF5 8.1m and EF6 10.5m (located below the mid-plane). CS coils are made of Nb₃Sn and have an outer diameter of 1.99m and an inner diameter of 1.60m. They are formed by six octa-pancakes and one quadra-pancake.

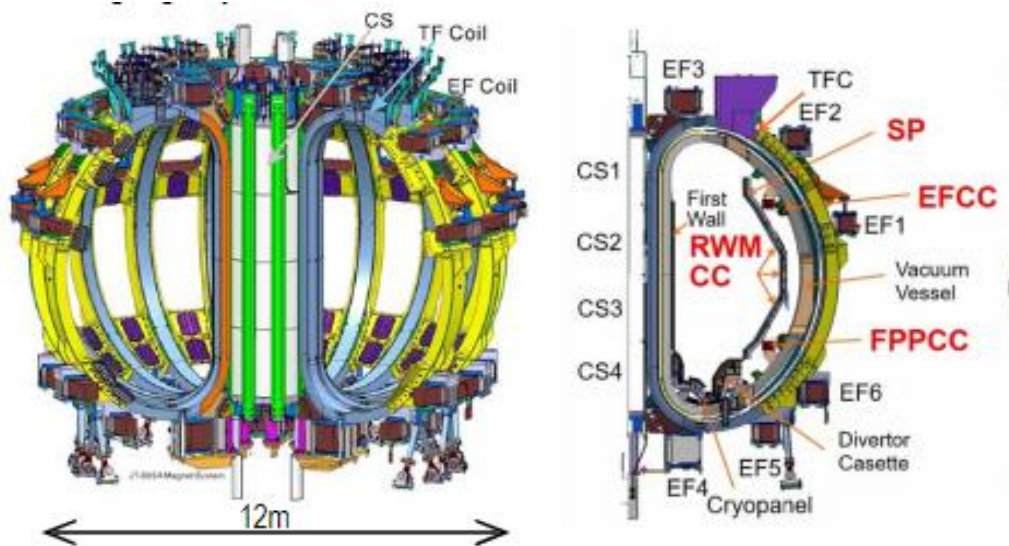


Figure 1.9 - Left: Magnet system of JT-60SA. Right: layout of in-vessel coils. [16]

Concerning the auxiliary heating system, JT-60SA has a NBI system and an ECRH system for long pulse operation (see figure 1.10). The NBI system includes 12 units of perpendicular and tangential positive-NBI (85KeV, 24MW in total) and 2 units of off-axis negative-NBI (500KeV, 10MW in total). They will all be used for pressure profile control, while N-NBI will also drive toroidal current and tangential P-NBI is used for plasma rotation control. The ECRH system consists of 9 gyrotron delivering a total power of 7MW and able to operate at 110 and 138 GHz depending on the tokamak magnetic field used.

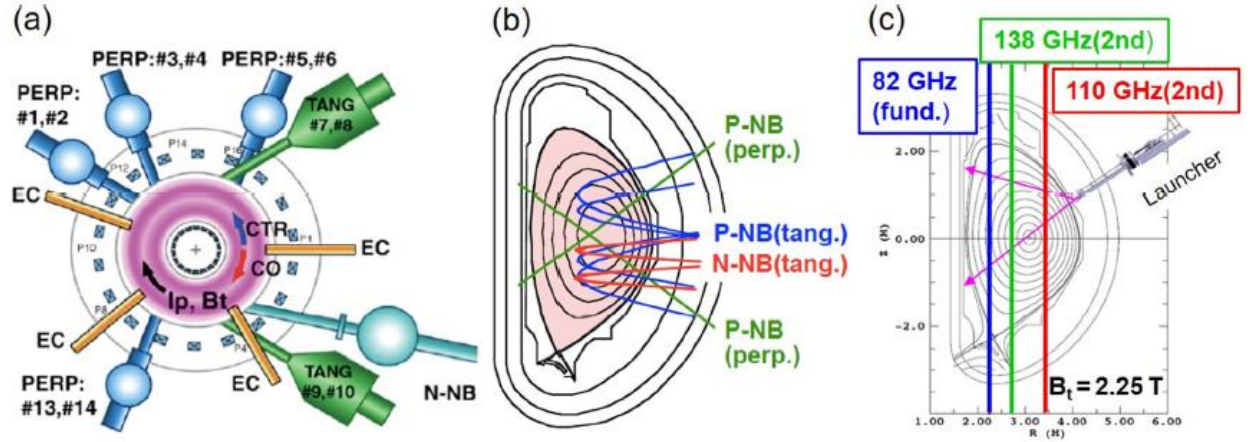


Figure 1.10 - a) top view of NBI and ECRH systems; b) NBI trajectories; c) ECRH resonance position. [16]

The JT-60SA objectives and strategies are reported in the JT-60SA Research Plan (see Ref [17]). In order to achieve them, three research phases are defined: initial research phase, integrated research phase and extended research phase. The first phase includes the first plasma using hydrogen, an upper divertor made of simple plates, two gyrotron and a basic set of indispensable diagnostics. The maximum plasma current is 2.5 MA and the nominal toroidal field of 2.25 T. Physics experiments start after the installation of the lower carbon divertor target, in-vessel coils, stabilizing plates, active cooling of in-vessel components and vacuum vessel, divertor pumping, 8 units of P-NBI, 2 units of N-NBI, other 2 gyrotron, pellet injectors, massive gas injectors and additional diagnostics. The aim is to reach a plasma current of 5.5MA. At the end of the first phase, also deuterium is used and the heating power will be 20MW for P-NBI, 10MW for N-NBI and 3MW for ECRH. The second phase is used to demonstrate high power long pulse discharges with full carbon mono-block lower single null divertor target. The capability of ECRH will be increased up to 7 MW. At the middle of the second phase, the divertor target will be changed with a tungsten-coated carbon one. Finally, during the third phase the capability of JT-60SA will be extended to higher heating power of 41 MW with single-null or double-null configurations and possibly using mono-block tungsten components in the high heat flux parts of the divertors. [15] [16]

1.5 Scenarios and objectives

JT-60SA has been designed to satisfy all of the central research needs for ITER; in order to do that, three main scenarios (corresponding to the main scenarios of ITER) will be tested during the operations phases.

The first one consists of the standard H-mode operation scenario. It could be run at currents from 4.6 MA to 5.5 MA and it is tabled in the Research Plan (Ref. [17]) as scenario #2. The total heating power available is of 41MW divided into 7MW of ECRH, 10MW of N-NBI and 24MW if P-NBI. The main parameters of the scenario #2 are reported in table 1.2.

Table 1.2 - Typical parameters of scenario #2.

Plasma current I_p (MA)	5.50
Toroidal magnetic field B_T (T)	2.25
Major radius R (m)	2.96
Minor radius a (m)	1.18
Elongation	1.87
Triangularity	0.50
Safety factor q_{95}	3.00
Shape parameter	6.30
Volumetric averaged temperature (KeV)	6.30
Volumetric averaged electron density ($10E20/m^3$)	0.56
Thermal averaged confinement time τ_E(s)	0.54
H factor	1.30
Current diffusion time (s)	32.7
Normalized beta β_N	3.10
Non inductive fraction	0.50
Plasma volume (m^3)	131

The second scenario is the advance inductive (also called hybrid) operation scenario, known as scenario #4-2. It explores the q_{95} domain around 4 at plasma current between 4.6 MA and 3.5 MA and the H factor between 1.1 and 1.2. The total heating power available is of 37MW divided into 7MW of ECRH, 10MW of N-NBI and 20MW if P-NBI. The main parameters of the scenario #4-2 are reported in table 1.3.

Table 1.3 - Typical parameters of scenario #4-2.

Plasma current I_p (MA)	3.30
Toroidal magnetic field B_T (T)	2.28
Major radius R (m)	2.93
Minor radius a (m)	1.14
Elongation	1.80
Triangularity	0.41
Safety factor q_{95}	4.40
Shape parameter	5.90
Volumetric averaged temperature (KeV)	3.70

Volumetric averaged electron density (10E20/m³)	0.62
Thermal averaged confinement time τ_E(s)	0.36
H factor	1.20
Current diffusion time (s)	14.6
Normalized beta β_N	3.00
Non inductive fraction	0.58
Plasma volume (m³)	122

The third scenario is the steady-state operation scenario, or #5-1. The total heating power available is of 37MW divided into 7MW of ECRH, 10MW of N-NBI and 20MW if P-NBI. The main parameters of the scenario #5-1 are reported in table 1.4. [\[17\]](#)

Table 1.4 - Typical parameters of scenario #5-1.

Plasma current I_p (MA)	2.30
Toroidal magnetic field B_T (T)	1.72
Major radius R (m)	2.97
Minor radius a (m)	1.11
Elongation	1.90
Triangularity	0.47
Safety factor q_{95}	5.80
Shape parameter	7.00
Volumetric averaged temperature (KeV)	3.40
Volumetric averaged electron density (10E20/m³)	0.42
Thermal averaged confinement time τ_E(s)	0.23
H factor	1.30
Current diffusion time (s)	12.6
Normalized beta β_N	4.30
Non inductive fraction	1
Plasma volume (m³)	124

Once the parameters of all the scenarios have been defined, theoretical models and simulations codes have been validated in order to establish a solid basis for the designed scenarios. Considerable progress has been made with detailed modelling and the simulation of plasma evolution, control, stability and its impact on plasma facing materials. More detailed information about progress on JT-

60SA will be available into “Advances in the physics studies for the JT-60SA tokamak exploitation and research plan” that will be publish in Plasma Physic Control Fusion (2019).

The aim of this study consists of optimizing some of the JT-60SA scenarios. This means that the value of the main parameters in the tables, a discharge duration time of 100s and the respect of coils current limits have been reached at the same time.

Direct simulation means a simulation that shows only how the plasma will evolve for certain given control inputs. However, what are the control parameters that ensure that the plasma evolves through certain prescribed states? The evolution of the plasma equilibrium is a non-linear process that is coupled in time through induction of currents in passive structures and coils. All existing approaches for finding feedforward control rely on inverse static equilibrium simulations and interpolation between two successive equilibria.

For the first time, in order to reproduce a full tokamak discharge simulation, a fast integrated tokamak modelling tool for scenario design (METIS) is coupled with a quasi-static free-boundary equilibrium code (FEEQS). Starting from a set of input parameters, the first code is able to compute at each time the plasma equilibrium, the current and the pressure plasma profiles. These outputs are given to the second code that provides the best coils currents in order to obtain a given plasma shape.

In the following work, the whole process of optimization is carried out. In chapter 2 all of the codes needed for the optimization are introduced and explained. Chapter 3 is divided in three parts: the first one concerns the verification of the FEEQS code used in inverse magnetostatic mode; the second part shows the benchmark of the FEEQS code used in inverse Poynting mode; the last part shows the results obtained using the two codes in order to optimize the JT-60SA scenarios. The analysis is important not only to ensure a well-programmed discharge and to avoid disruption and damage to the machine, but also to find the trickiest points in the simulation and propose improvements.

2. Codes for integrated tokamak modelling

Integrated modelling of burning plasma is an essential task for the realization of a nuclear fusion reactor, especially for the ITER program. The existence of a reliable computer code having as input the same control parameters used to pilot the machine and able to predict the full time evolution of a tokamak discharge, is mandatory. These type of codes are called simulators. They have to include sophisticated physics models and to be validated using experimental models since nuclear fusion reactors are a completely new type of device. [18]

An overview of the scenario optimization tools used in the study is shown in the figure 2.1.

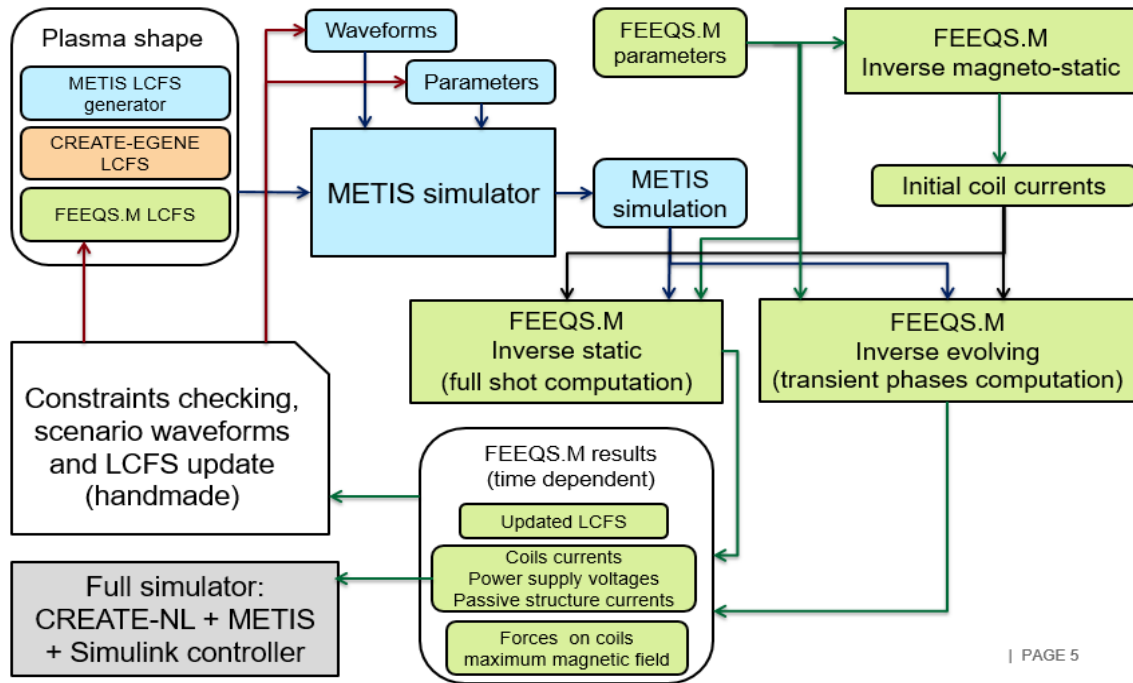


Figure 2.1 - Tools for scenario optimization. Figure shows how three codes are used together in order to simulate a whole tokamak discharge. How METIS, FEEQS and CREATE-EGENE interact each other are stressed.

As it is possible to notice from figure 2.1, FEEQS and METIS codes are used to optimize two scenarios of JT-60SA because they are able to simulate a full tokamak discharge. In particular, METIS provides current and pressure plasma profiles to FEEQS that computes the best coils currents in order to reach a given plasma shape.

Figure 2.1 shows also a third code, CREATE-NL. It solves the free boundary dynamic plasma equilibrium problem using first order finite element method (FEM). It is able to generate a new equilibrium and modifies an existing one by changing the poloidal field coil currents, boundary flux and shape parameters. A next step in the development of a combined simulator is to couple CREATE-NL and METIS in order to simulate a full tokamak discharge. In fact, using as constraints the METIS prediction for plasma current (I_p), I_i and β_p , CREATE-NL provides the last closed flux surface (LCFS) shape to METIS for the flattop.

The codes used to carry out the optimization of various scenarios of JT60-SA, which is the aim of the study, are briefly described in this chapter.

2.1 Reconstruction of plasma equilibrium

The reconstruction of the equilibrium of a plasma in a tokamak is a free boundary problem described by the Grad-Shafranov equation in axisymmetric configuration. The Grad-Shafranov equation is the equilibrium equation in ideal magnetohydrodynamics (MHD) for a two dimensional plasma. This equation is a two-dimensional, nonlinear, elliptic partial differential equation obtained from the reduction of the ideal MHD equations to two dimensions.

Starting from the momentum equation for the plasma, it is possible to reconstruct the equilibrium in a tokamak:

$$\rho \frac{du}{dt} + \nabla P = j \times B$$

Where ρ is the mass density, u the mean velocity of the particles, P the kinetic pressure, j the plasma current density and B the magnetic field. The first term can be neglected compared to the pressure gradient and the equilibrium becomes:

$$\nabla P = j \times B$$

This means that at each time the Lorentz force balances the force due to the kinetic pressure. From the equation it is clear that $B \cdot \nabla P = 0$ and $j \cdot \nabla P = 0$. Therefore, field lines and current lines lie on adiabatic surfaces, called magnetic surfaces. The inner one degenerates into a closed curve, called magnetic axis, while the outer one corresponds to the plasma boundary (surface in contact with limiter or magnetic separatrix LCFS). Inside the LCFS (last closed flux surface), the flux lines are closed in vacuum chamber, outside the LCFS the flux lines are open.

The equilibrium of the plasma in the presence of a magnetic field is described taking into account the magnetostatic Maxwell's equations:

$$\mu_0 j = \nabla \times B$$

$$\nabla \cdot B = 0$$

Where μ_0 is the magnetic permeability of the vacuum.

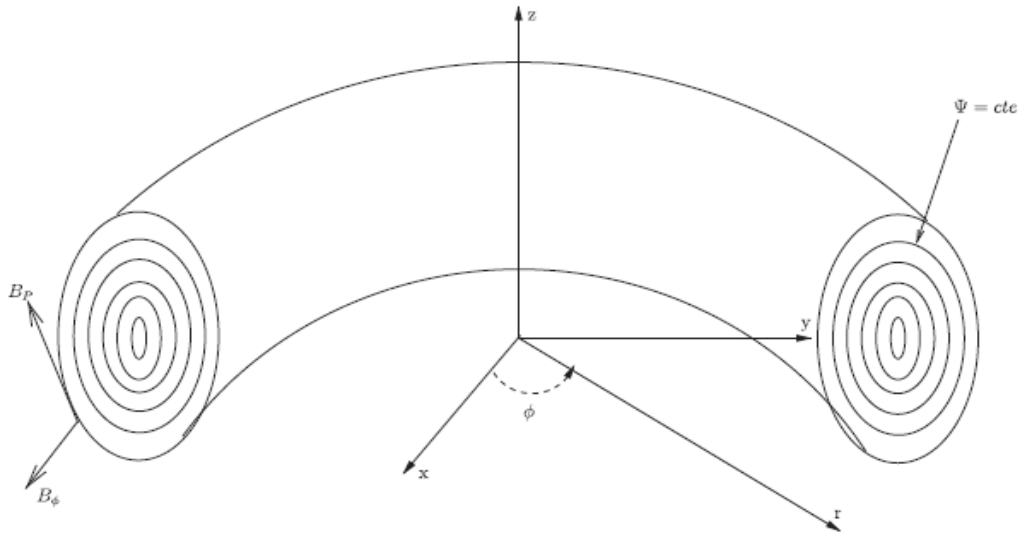


Figure 2.2 - Toroidal geometry of a plasma column. [12]

Using the cylindrical coordinate system represented in the figure 2.2 and considering that the magnetic field \vec{B} is independent of the toroidal angle ϕ , it is possible to define the function $\Psi(R, Z)$ that is the flux of the magnetic field \vec{B} through the horizontal disk $S(R, Z)$ (reported in figure 1.8), divided by 2π :

$$\Psi(R, Z) = \frac{1}{2\pi} \int_{S(R, Z)} \vec{B} \cdot \vec{ds} = \int_0^R B_z(R, Z) R dR$$

Where S is defined as the disc having as circumference the circle centered on the O_z axis and passing through a point (R, Z) in a poloidal section (see figure 2.3).

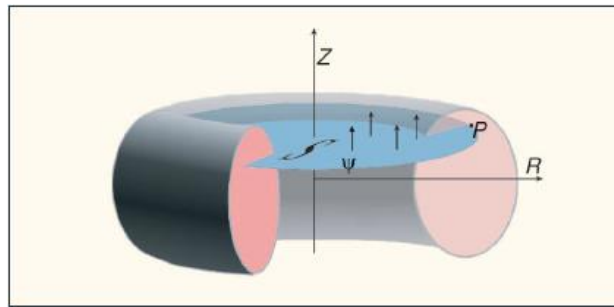


Figure 2.3 - Definition of poloidal flux function. The poloidal flux at point P in the (R, Z) cross section of the plasma is the total flux trough the surface S bounded by the toroidal ring passing through P . [9]

Deriving the equation respect to R :

$$\frac{\partial \Psi}{\partial R}(R, Z) = \frac{\partial}{\partial R} \left(\int_0^R B_z(R, Z) R dR \right) = R B_z(R, Z)$$

Deriving respect to z and considering that $\vec{\nabla} \cdot \vec{B} = \frac{1}{R} \frac{\partial(RB_R)}{\partial R} + \frac{\partial B_Z}{\partial z} = 0$:

$$\frac{\partial \Psi}{\partial Z}(R, Z) = \left(\int_0^R \frac{\partial B_Z}{\partial Z}(R, Z) R dR \right) = \int_0^R -\frac{\partial(RB_Z)}{\partial R}(R, Z) dR = -RB_R(R, Z)$$

Defining the diamagnetic function as $F = RB_\phi$, it is possible to decompose the magnetic field as:

$$\begin{cases} B_R = -\frac{1}{R} \frac{\partial \Psi}{\partial Z} \\ B_Z = \frac{1}{R} \frac{\partial \Psi}{\partial R} \\ B_\phi = \frac{F}{R} \end{cases}$$

Considering $B_p = B_R \vec{e}_R + B_Z \vec{e}_Z$, it is possible to write:

$$\begin{cases} \vec{B} = \vec{B}_p + \vec{B}_\phi \\ \vec{B}_p = \frac{1}{R} \vec{\nabla} \Psi \times \vec{e}_\phi \\ \vec{B}_\phi = \frac{F}{R} \vec{e}_\phi \end{cases}$$

Therefore, from Maxwell's equations, $B \cdot \nabla \Psi = 0$. This means that Ψ is a constant on each magnetic surface and $P=P(\Psi)$. It is possible to apply the same decomposition to j :

$$j_p = \frac{1}{R} \left[\nabla \left(\frac{F}{\mu_0} \right) \times \vec{e}_\phi \right]$$

Since $j \cdot \nabla P = 0$ also $\nabla F \cdot \nabla P = 0$ and therefore, F is constant on the magnetic surface, $F=F(\Psi)$.

From Maxwell's equations is possible to deduce that $B_\phi = \frac{F}{R} \vec{e}_\phi$ and $j_\phi = (-\Delta^* \Psi) \vec{e}_\phi$. Since $\nabla P = P'(\Psi) \nabla \Psi$ and $\nabla F = F'(\Psi) \nabla \Psi$ is possible to write the Grad-Shafranov equation valid in the plasma [\[12\]](#):

$$-\Delta_{\mu_0}^* \Psi = RP'(\Psi) + \frac{1}{R\mu_0} FF'(\psi)$$

Where Δ_μ^* is the elliptic operator defined as:

$$\Delta_\mu^* \Psi = \frac{\partial}{\partial R} \left(\frac{1}{\mu R} \frac{\partial \Psi}{\partial R} \right) + \frac{\partial}{\partial Z} \left(\frac{1}{\mu R} \frac{\partial \Psi}{\partial Z} \right) = -R \vec{\nabla} \cdot \left(\frac{1}{\mu R^2} \vec{\nabla} \Psi \right)$$

2.2 CRONOS code

CRONOS consists of a numerical suite of codes that integrates a 1D transport solver with general 2D magnetic equilibria (for this reason these type of codes are also called 1.5D codes), several heat, particles and impurities transport models, heat, particles and momentum sources such as neutral beams, radio-frequency waves and pellet injection. It solves the transport equations in one dimension using the minor radius space coordinate for various fluid quantities such as particles and impurities densities, ion and electron temperatures, current density and others.

From the beginning of CRONOS development, the most comprehensive physics solvers available have been included in the codes. These are reported in the figure 2.4.

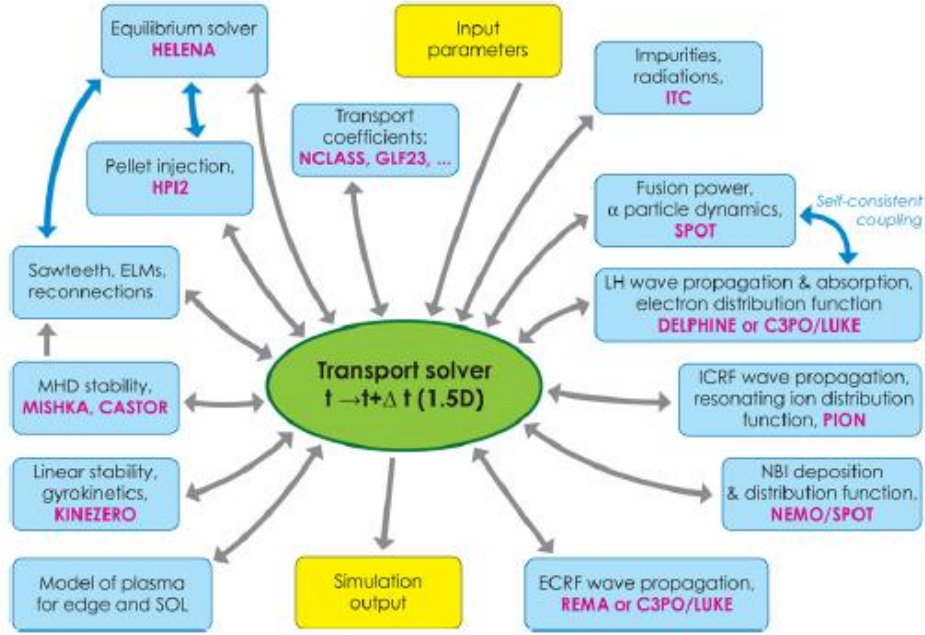


Figure 2.4 - Main sophisticated physics modules around the core transport equations solvers. [18]

In order to simulate a tokamak discharge the code is used in the predictive mode. This mode consists of solving the 1D radial transport equation for the poloidal flux, electron and ion temperature, particles densities and momentum, as well as 2D magnetic equilibria. For this reason, most variables are 1D time dependent radial profiles. They correspond to the average of the physical quantity over an infinitesimal volume around a flux surface of given radial position. The radial grid is equally spaced in normalized toroidal flux coordinate $x = \rho / \rho_m$, with $\rho = \sqrt{\Phi / \pi B_0}$, where Φ is the toroidal magnetic flux, B_0 the vacuum magnetic field at a given major radius R_0 and ρ_m is the value of ρ at the last closed flux surface. The transport equations solved assumes that B_0 does not change with time. These are second-order differential equations in space and two boundary conditions are needed. The first one is to impose $\left. \frac{\partial A}{\partial \rho} \right|_{x=0} = 0$, where A is the transported quantity; the second is the value of A at $x=1$. The transport equations and equilibrium are coupled in the quasi-static approximation: the time scale for perpendicular force balance is assumed much smaller than the radial transport time scale. This allows calculating static equilibria using the Grad-Shafranov equation at several time slices when solving the

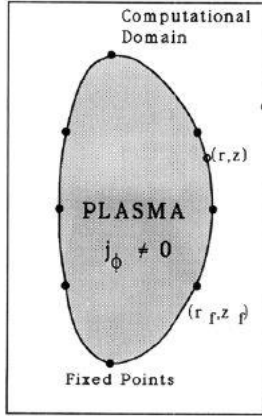


Figure 2.5 -
Computational domain
and fixed points
boundary. [19]

time-dependent transport equations. The equilibrium calculation mode in CRONOS is the fixed-boundary solver. This method consists of calculating the geometry of the magnetic surfaces using the current and the pressure profiles that are given by the transport equations as input. The plasma boundary is described as a series of (R,Z) points and the LCFS is prescribed and is taken as boundary condition (see figure 2.5). In alternative, it is possible to use also a free-boundary solver such as the FEEQS code.

CRONOS works also in the so-called interpretative mode using the experimental profiles of various fluid quantities to deduce the transport coefficients. This function is used to validate the overall functioning of the code in order to give confidence in the output of the code itself, which has been used to predict relevant scenarios of ITER and DEMO. Moreover, it is possible to analyze data from many tokamaks as Tore Supra, JET, TCV, JT-60U and others.

The use of state-of-the-art modules increases the accuracy of the simulation, but also the computational cost in computing time. To report an example, on ITER, the plasma turbulence evolves on time scale of 10^{-6} s, transported quantities evolves on a time scale of 1s and the diffusion of poloidal flux occurs in a time scale of 1000s. Due to the multi-scale nature of the physical problem, a simulation of a full discharge on ITER with a 1.5D transport code using sophisticated modules takes a few days. For this reason, a faster tool that allows testing and optimizing a large number of time-dependent scenarios has been developed. [18]

2.3 METIS code

METIS is a fast transport simulator code that allows building a realistic simulation of plasma scenarios in about one minute computation time, even for discharges of 1000s duration. It is in MATLAB language and contains some mexfile in C and in FORTRAN to solve PDE and for interpolation to speed up the computation. Originally, it is built as a module of CRONOS, later it has been developed as an autonomous code.

In order to be faster than a 1.5D code (2D equilibria and 1D transport equation) and to keep the reliability of the simulation results, a delicate development was necessary in order to establish what are the aspects of the transport that can be modelled in a simpler way. This is the code used in order to optimize the JT60-SA scenarios. Details of the equations that the code is able to solve are reported below and can be found in Ref [20].

The current diffusions and plasma equilibrium equations are used as in the 1.5D code. The first one is solved in terms of poloidal flux using a toroidal flux coordinate p grid, as in the CRONOS code. The equation solved is:

$$\begin{aligned} \frac{\partial \Psi}{\partial t} \Big|_{\rho_{norm}} &= \frac{\langle \frac{|\nabla \rho|^2}{R^2} \rangle}{\mu_0 \sigma_{||} \rho_m^2 \langle \frac{1}{R^2} \rangle} \frac{\partial^2 \Psi}{\partial \rho_{norm}^2} \\ &+ \left\{ \frac{\langle \frac{|\nabla \rho|^2}{R^2} \rangle}{\mu_0 \sigma_{||} \rho_m^2 \langle \frac{1}{R^2} \rangle} \frac{\partial}{\partial \rho_{norm}} \left[\ln \frac{\frac{\partial V}{\partial \rho_{norm}} \langle \frac{|\nabla \rho|^2}{R^2} \rangle}{F} \right] + \frac{\rho_{norm}}{\rho_m} \frac{d\rho_m}{dt} + \frac{\rho_{norm}}{2B_0} \frac{dB_0}{dt} \right\} \frac{\partial \Psi}{\partial \rho_{norm}} \\ &+ \frac{B_0}{\sigma_{||} F \langle \frac{1}{R^2} \rangle} j_{ni} \end{aligned}$$

Where $\frac{\partial \Psi}{\partial t} \Big|_{\rho_{norm}}$ is the time derivative of poloidal flux at a given radial position ρ_{norm} , $\sigma_{||}$ is the parallel electrical conductivity, F is the diamagnetic function, j_{ni} is the current density driven by non-inductive source, R the major radius coordinate, μ_0 is the magnetic permeability of free space, ρ_m the value of ρ at the last closed surface and $\rho_{norm} = \rho/\rho_m$ is the normalized toroidal flux coordinate. The notation $\langle \rangle$ indicates a magnetic flux surface average, defined as the volume average of a quantity around a flux surface of radial coordinate ρ .

In order to speed up the calculation, the current diffusion is computed on a 21 points radial grid only.

The modelling of heat transport is the most uncertain part of the code and consuming the largest CPU time, therefore it is treated as a mixed 0D-1D approach in order to accelerate the computation. The first step consists of solving the following equation for the plasma thermal energy content:

$$\frac{dW_{th}}{dt} = -\frac{W_{th}}{\tau_E} + P_{loss}$$

Where τ_E is the energy confinement time and P_{loss} is the total power transported away from the plasma separatrix by diffusion and convection phenomena.

The second step consists of computing the electron and ion temperatures profiles using the following two stationary equations on a set of pre-defined time slices:

$$\frac{\partial T_e}{\partial x} = \frac{-\int_0^x V' Q_e}{n_e \chi_e V' \langle |\nabla \rho|^2 \rangle} \text{ and } \frac{\partial T_i}{\partial x} = \frac{-\int_0^x V' Q_i}{n_i \chi_i V' \langle |\nabla \rho|^2 \rangle}$$

Where Q_e and Q_i are the electron and ion heat source terms, χ_e and χ_i are the electron and ion heat diffusion coefficients computed in a way consistent with the energy content that has been computed in the first step, V' is the derivative of the plasma volume enclosed in a magnetic surface with respect to the normalized radius ρ_{norm} and $\langle |\nabla \rho|^2 \rangle$ is the surface average of the squared gradient of the toroidal flux coordinate.

For the electron density profile a simpler approach is used. It is computed starting from the prescription of three parameters that are: the line-averaged density \bar{n}_e , the peaking factor $\frac{n_0}{\langle n \rangle}$ and the density value at the separatrix $n_{e,a}$.

All of the other species density profiles are assumed to be proportional to the electron density one (tungsten and helium ashes are treated separately). The ions species considered are H, D, D-T mixture, He and impurity ions.

In addition, an estimate of plasma rotation is computed taking into account the effect of neutral beam injection and intrinsic rotation, while the toroidal rotation due to the fast ion losses and the fast ion momentum transport is neglected.

Finally, METIS includes fast solvers for the computation of the source terms for the heat transport equation and the current diffusion one. They are chosen in order to be fast and simple avoiding increase of computational speed. The sources taken into account are NBI, ICRH, LH, ECRH, pellets injection, fusion reaction of thermal ions, ripple effects, wall recycling and radiative processes.

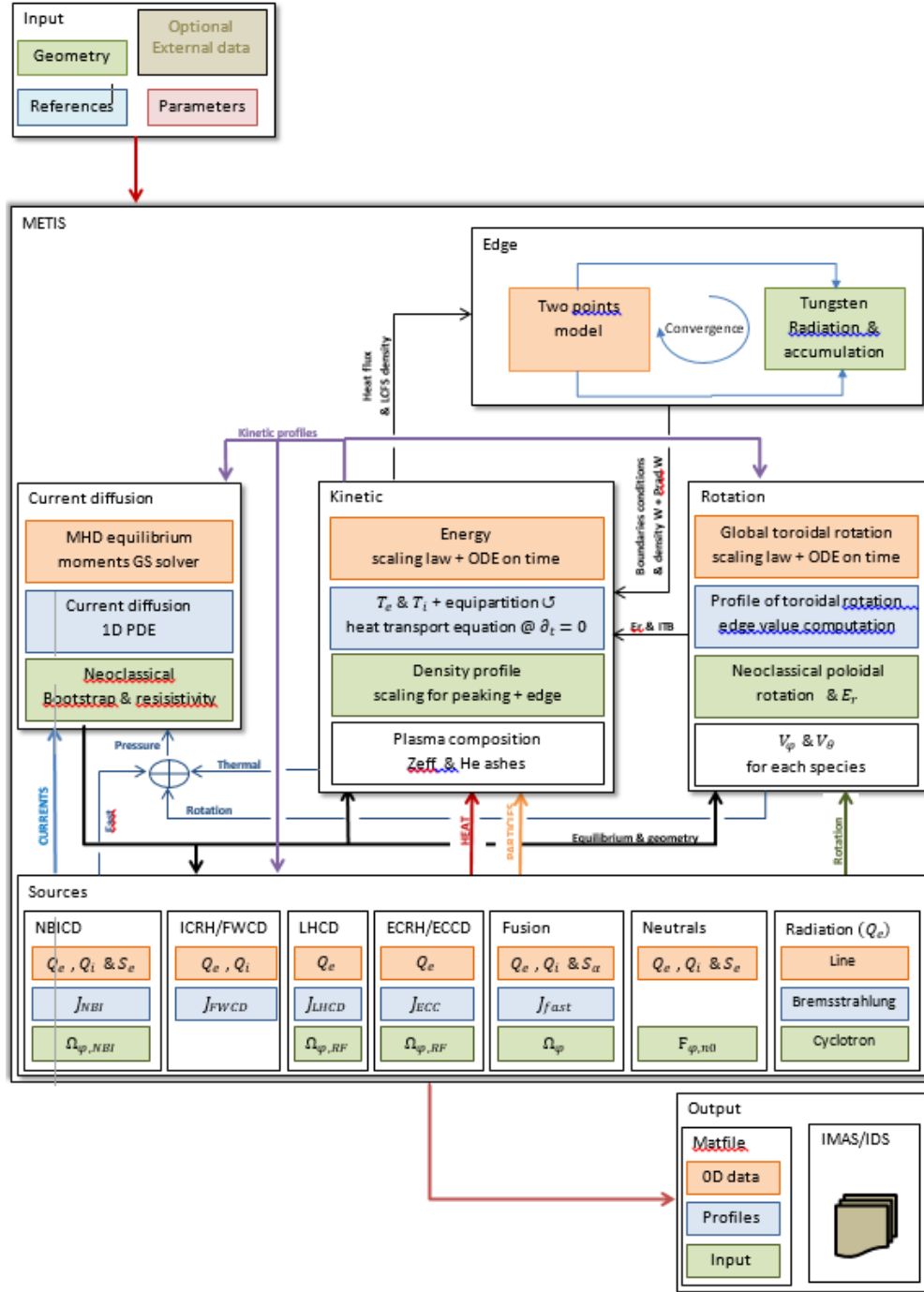


Figure 2.6 - METIS internal organization. [20]

The figure 2.6 shows METIS internal structure and how it works. In order to use large time steps and to reduce the CPU time of simulation the numerical algorithm inside METIS consists of a global convergence loop on the whole time evolution of all plasma quantities that are in storage as g_N at iteration N . A new time evolution of all plasma quantities $F(g_N)$ is computed starting from the g_N time evolution at each iteration of the main loop. This new time evolution is combined to the previous one in order to compute the time evolution at the next iteration following the formula:

$$g_{N+1} = \alpha_N F(g_N) + (1 - \alpha_N) g_N$$

Where α_N is an oscillation damping coefficient that depends of the number of iterations (for the first 21 iteration $\alpha_{N+1} = 0.95\alpha_N$). The loop ends when the relative difference between $F(g_N)$ and g_N is lower than a required value.

It is possible to make simulations taking data from existing experiments already done on various tokamaks. However, according to the purpose of this study, the most interesting way to use METIS is by means of on a dedicated scenario generator. The following figure 2.7 represents the graphical user interface (GUI) used to give the inputs data to the code. [20]

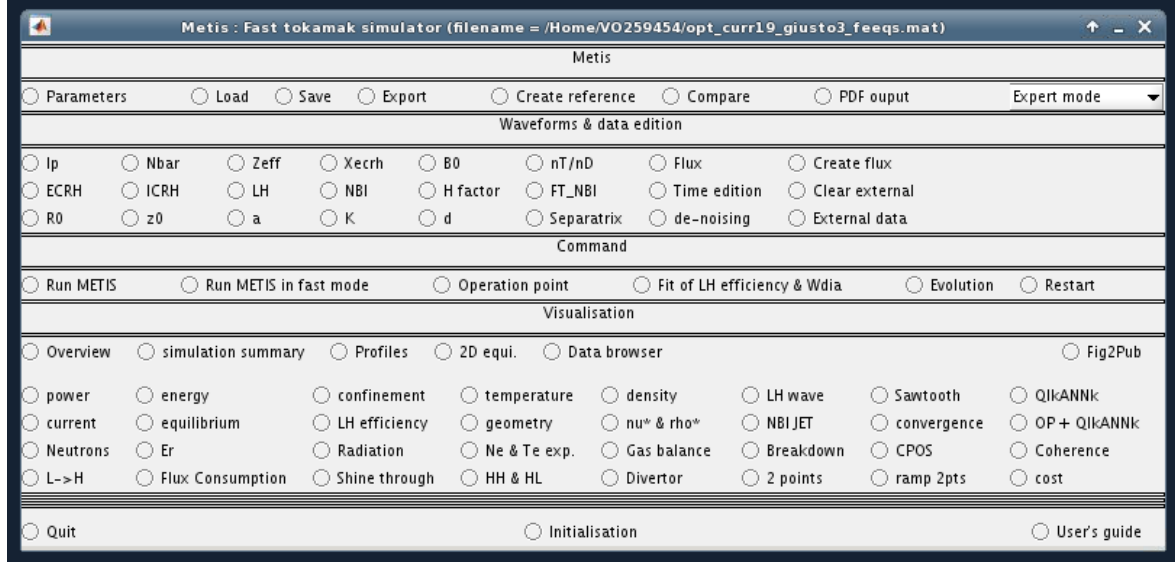


Figure 2.7 - GUI to input data on METIS.

The inputs are given as waveforms in time and they consist of:

- Plasma current I_p ;
- Line-averaged electron density N_{bar} ;
- Line-averaged effective charge Z_{eff} ;
- Position of the maximum power deposition for ECRH;
- Toroidal field at the toroidal coils center B_0 ;
- Ratio between tritium and deuterium density;
- Power injected in the plasma by the electron cyclotron resonance heating system ECRH;
- Power injected in the plasma by the ion cyclotron resonance heating system ICRH;
- Power injected in the plasma by the lower hybrid heating system LH;
- Power injected in the plasma by the neutral beam injection system NBI;
- Confinement multiplication H factor for L and H mode;
- Major plasma radius R_0 ;
- Minor plasma radius a ;
- Vertical plasma position z_0 ;
- Plasma elongation k ;
- Upper and lower plasma triangularity d .

In this case, METIS uses a description of plasma geometry given by moments of the 2D magnetic geometry. It is possible to describe the plasma shape using a LCFS given by points. In this way, the LCFS is given by a list of points $(R, Z)_k$ that are used to recompute the moments and the global geometric quantities as defined above. The equilibrium mesh is corrected using a morphing function in such a way that the current diffusion equation is solved using corrected geometrical coefficients.

The lower part of figure 2.8 shows the standard outputs produced by the code. In addition, a data browser can be used to plot all of the output data computed. An example is reported in the following figure 2.6. [\[20\]](#)

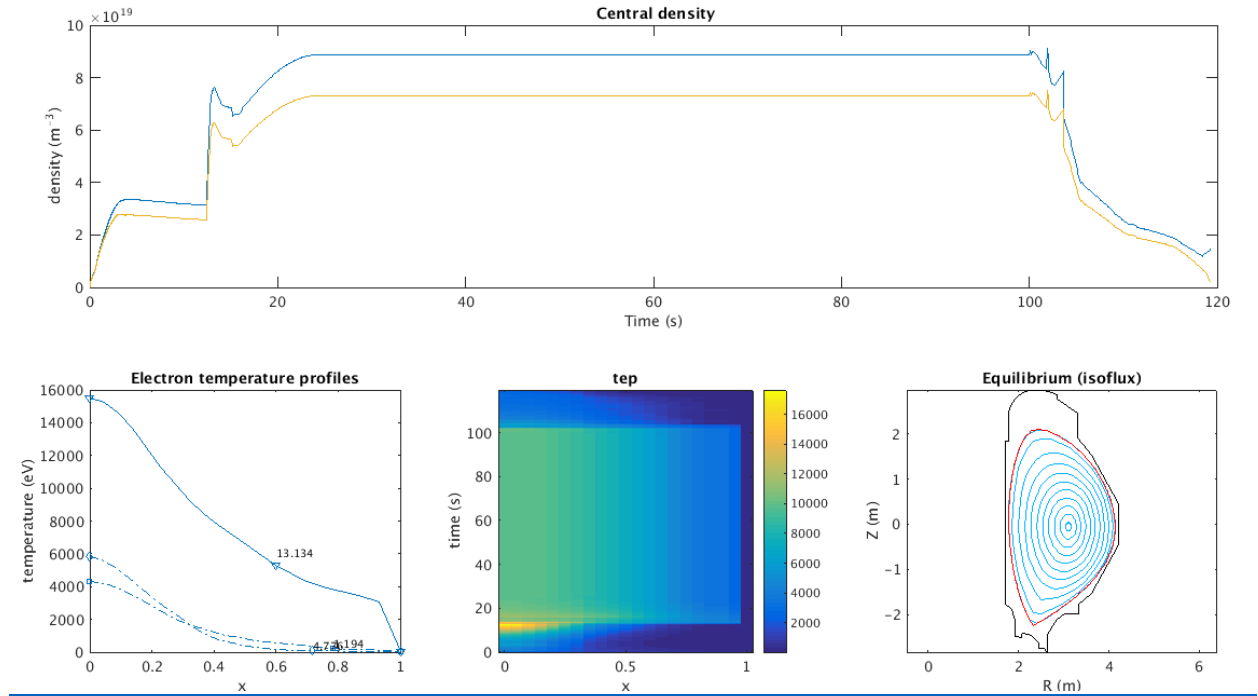


Figure 2.8 - Example of data browser windows. The upper part shows the ions (yellow) and electron (blue) central density; the bottom left part shows the radial profiles of electron temperature at time 1.194s, 4.776s and 13.748s; central bottom figure shows the electron temperature plotted into radial-time coordinates; the right bottom picture shows the plasma equilibrium at 13.748s.

In the upper part, the central electron and ion densities are plotted vs time (electron in blue and ion in yellow). In the left bottom part the radial profiles of electron temperature at time $t=1.194$ s (ramp-up phase), $t=4.776$ s (reaching of x-point) and $t=13.748$ s (H-mode transition) are shown. In the center bottom part the value electron temperature is plotted in 2D coordinates (radial and time). While the right bottom part graph shows the plasma equilibrium (i.e., the cross-section of the magnetic flux surfaces) at $t=13.748$ s.

2.4 FEEQS code

In order to simulate a whole tokamak discharge, it is necessary to compute the time series of currents applied into the poloidal field coils. To deal with this problem a so-called free-boundary equilibrium evolution method is used (FBEE). The code combines the classic Grad-Shafranov equation for MHD equilibrium in an axisymmetric system with circuit and induction equations for poloidal field coils and passive structures inside the tokamak. This type of codes are able to find a specific set of voltages that can ensure a certain scenario, to check if the voltages are sufficient to permit the transition from limiter to divertor configuration, to compute the current accumulated in the passive components and to compare the results to technological constraints. If these functions are computed, the code is working in inverse mode. Of course, there is a huge variety of possible voltages configurations and the problem is still non-linear, therefore it is difficult to predict the exact voltages values.

The code can also work in direct mode if it is used to provide plasma boundary position and shape for given PF coils currents. Both modes are used to optimize the JT-60SA scenarios.

In the code, the tokamak equilibrium is described using the MHD model, therefore it is computed starting from the following equation:

$$\vec{\nabla} p = \vec{j} \times \vec{B}$$

Where p is the scalar plasma pressure, \vec{j} is the current density and \vec{B} is the magnetic field.

In the cylindrical coordinates system (R, φ, Z) and under the axisymmetric assumption, the poloidal flux function is defined as:

$$\Psi(R, Z) = \frac{1}{2\pi} \int_{D(R, Z)} \vec{B} \cdot \vec{ds}$$

Where $D(R, Z)$ is a horizontal disk centered on the symmetry axis of the tokamak

Assuming that the magnetic field does not depend on the toroidal angle φ and starting from Maxwell's equation, it is possible to deduce the general equation for the poloidal flux $\Psi(R, Z)$ valid in the poloidal plane and using a cylindrical coordinate system:

$$-\Delta_{\mu}^* \Psi e_{\varphi} = \vec{J}_{\varphi}$$

Where μ is the magnetic permeability.

The value of the poloidal flux depends on the different parts of the tokamak, therefore 5 subdomains have been defined (see figure 2.9):

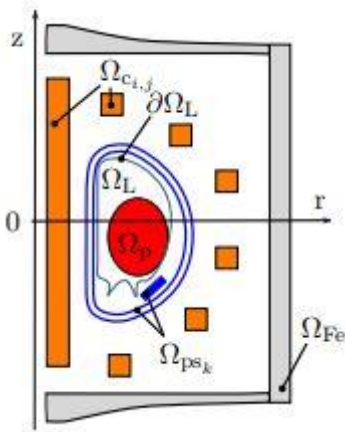


Figure 2.9 - Areas of the poloidal domain considered. [21]

- Ω_p plasma region;
- Ω_{Bi} coils region;
- Ω_{ps} passive structure region;
- Ω_f ferromagnetic structure;

- Ω_a vacuum region.

Let Γ_L be the first wall of the device, and Ω_L the area inside Γ_L . Considering the poloidal section of the plasma inside the torus, the inner isoflux degenerates into a line and it is known as magnetic axis. The value of the function Ψ into the magnetic axis is quoted as Ψ_a :

$$\Psi_a = \sup_{\Omega_p} \Psi$$

Let Ψ_b be the value of Ψ on the plasma boundary:

$$\Psi_b = \sup_D \Psi$$

It is possible to determine the normalized flux as:

$$\Psi_N = \frac{\Psi - \Psi_a}{\Psi_b - \Psi_a}$$

And compute the toroidal current density in each subdomain.

The plasma boundary Γ_p is defined as the outermost closed flux surface inside the first wall. it is possible to define the plasma boundary as:

$$\Gamma_p = \{M \in \Omega_L | \Psi(M) = \sup_D \Psi\}$$

$$\text{where } D = \{M \in \Gamma_L | \overrightarrow{P_a M} \cdot \overrightarrow{\nabla \Psi} < 0\} \cup \{X \in \Omega_L, X \neq P_a | \overrightarrow{\nabla \Psi} = 0\}$$

where P_a is the magnetic axis.

This leads to define the plasma area as:

$$\left\{ \begin{array}{l} \Psi_b = \sup_D \Psi \\ \Omega_p = \{M \in \Omega_L | \Psi(M) \geq \Psi_b\} \end{array} \right.$$

Therefore, it is possible to rewrite the Grad-Shafranov equation for each subdomain.

$$\text{In the plasma area } \Omega_p: -\Delta_{\mu_0}^* \Psi = R \frac{dP}{d\Psi} + \frac{1}{2\mu_0 R} \frac{dF^2}{d\Psi} = j_\varphi(R, \Psi)$$

$$\text{In the passive structure } \Omega_{ps}: -\Delta_{\mu_0}^* \Psi = -\frac{\sigma}{R} \frac{\partial \Psi}{\partial t}$$

Where σ is the electrical conductivity of the structure.

$$\text{In the coils } \Omega_{Bi}, \text{ considering } N_c \text{ coils: } -\Delta_{\mu_0}^* \Psi = \frac{n_i V_i}{R_i S_i} - \frac{2\pi n_i^2}{R_i S_i^2} \int_{\Omega_{Bi}} \frac{\partial \Psi}{\partial t}$$

Where V_i is the voltage applied to coil i , n_i is the number of wire turns, R_i is the resistance of the wire and S_i its cross section.

In the vacuum and in the ferromagnetic structures the current density is assumed to be 0:

$$\text{In } \Omega_a -\Delta_{\mu_0}^* \Psi = 0$$

$$\text{In } \Omega_f -\Delta_{\mu}^* \Psi = 0$$

The boundary conditions on Ψ have to be set in order to solve the system of equations. Ψ is equal to zero on the O_z axis. Due to the absence of the current outside the plasma region, it is possible to impose $\Psi = 0$ at infinity. Therefore, the boundary conditions are:

$$\begin{cases} \lim_{||R,Z|| \rightarrow +\infty} \Psi(R,Z) = 0 \\ \Psi(r = 0, Z) = 0 \end{cases}$$

Being the domain Ω large enough, it is possible to change the first limit condition with $\Psi(R,Z) = 0$ on the boundary Γ . If the boundary of the domain is a semicircle containing all of the tokamak structures, it is possible to solve the equilibrium problem on the boundary Γ . The value of Ψ on Γ is calculated using Green functions, because here the problem becomes linear. Therefore, the boundary condition become:

$$\begin{cases} \Psi(R,Z) = g(R,Z) \text{ on } \Gamma \\ \Psi(r = 0, Z) = 0 \end{cases}$$

The time dependent equilibrium system that the code is able to solve using a finite element formulation with P1 elements is:

$$\left\{ \begin{array}{l} -\Delta_{\mu_0}^* \Psi = R \frac{dP}{d\Psi} + \frac{1}{2\mu_0 R} \frac{dF^2}{d\Psi} \text{ in } \Omega_p \\ -\Delta_{\mu_0}^* \Psi = \frac{n_i V_i}{R_i S_i} - \frac{2\pi n_i^2}{R_i S_i^2} \int_{\Omega_{Bi}} \frac{\partial \Psi}{\partial t} \text{ in } \Omega_{Bi} \\ -\Delta_{\mu_0}^* \Psi = -\frac{\sigma}{R} \frac{\partial \Psi}{\partial t} \text{ in } \Omega_{ps} \\ -\Delta_{\mu_0}^* \Psi = 0 \text{ in } \Omega_a \\ -\Delta_{\mu}^* \Psi = 0 \text{ in } \Omega_f \\ \Psi_a = \sup_{\Omega_p} \Psi \\ \Psi_b = \sup_D \Psi \\ \Omega_p = \{M \in \Omega_L | \Psi(M) \geq \Psi_b\} \\ \Psi_N = \frac{\Psi - \Psi_a}{\Psi_b - \Psi_a} \\ \Psi(r = 0, Z) = 0 \\ \Psi(R, Z) = g(R, Z) \text{ in } \Gamma \end{array} \right.$$

The finite element method is a classical method used to solve partial differential equation. Once the weak formulation of the problem has been written, the resolution of the domain is divided into elements, triangles in the case of P1 formulation. The problem is solved into an approximate space, generated by the basic functions of the finite elements. In case of P1 formulation, these functions are

continuous and linear on each elements. Writing the approximate problem for each basic functions of the approximate space, a matrix system like $Ax=b$ is obtained and this system can be solved. [22]

P1 is a one-dimensional problem such that $P1: \begin{cases} -u''(x) = f(x) \text{ for } 0 < x < 1 \\ u(0) = u(1) = 0 \end{cases}$ where f is a given continuous function and u as unknown function of x . Integrating the equation $-u''=f$ twice, this problem has a unique solution u . [23]

The problem still has three nonlinearities: the magnetic permeability, the current density in the plasma and the plasma boundary. They are solved using the Newton's method because it is always stable and it gives a quadratic convergence if the initial step is close enough to the solution. FEEQS computes the initial step using a Picard method giving an initial elliptic plasma boundary, where the current density is constant. Newton's method stops when the relative error is smaller than a given precision that is 10^{-10} . This value of magnitude is higher than the order of magnitude of the machine epsilon because the equilibrium computation need a lot of operation. The machine epsilon is defined as the difference between 1 and the least value greater than 1 that is representable in the given floating point type and its value is typically 10^{-16} . [24]

In order to optimize the scenarios, it is possible to use FEEQS in three different modes. The inverse magneto-static mode is necessary to compute static solution of current in the coils during the breakdown phase, minimizing the poloidal field in the user defined zone, maximizing the poloidal flux at the planned magnetic axis position and respecting currents limits of coils. The inverse Poynting mode gives as results the real LCFS shapes, coils currents for full simulation, forces and maximum magnetic field on coils and the estimation of voltage on coils. In this case the constraints are P' and FF' profiles and plasma shape from METIS, plasma current, LCFS poloidal flux and coils limits. However, a self consistently computed current in passive structures is still missing. Nevertheless, it is used for the optimization process. The inverse evolving mode is suitable for transient studies as current on passive structures, but it is quite time consuming and it needs some tuning of parameters to converge. For this reason, it is not very well adapted to whole scenario studies. [21] [25]

3. Case of Study

The aim of the work is to simulate the whole discharge of JT-60SA in order to optimize its scenarios. The discharge of a plasma includes the breakdown, the ramp-up, the flattop and the ramp-down phases. Therefore, all of these parts have to be simulated and controlled. To concern with the first one, FEEQS in inverse magnetostatic mode is used. The sub-chapter 3.1 is dedicated to the validation of the code. It shows the comparison of the results obtained through the simulations with data computed with another code. Sub-chapter 3.2 contains the results obtained running for the first time the coupled codes. In order to validate them, the results are compared with data already available and computed using other codes. In order to be sure that the two codes are able to simulate a plasma discharge, the benchmark of FEEQS in inverse Poynting mode has been done and the results are shown in this sub-chapter. Once the codes have been validated, the optimization of scenario is carried out. The sub-chapter 3.3 reports the results obtained using the coupled codes to optimize two of three JT-60SA defined scenarios.

3.1 FEEQS in inverse magnetostatic mode: plasma breakdown

Stable plasma initiation will be obtained by a combination of good wall conditioning followed by precise magnetic field control and gas puffing; therefore, optimization of voltage waveforms of poloidal field coil is necessary. The same plasma initiation condition of ITER can be applied to JT-60SA because it is a large superconducting tokamak. In the paper *Optimization of plasma initiation scenario in JT-60SA* published by M. MATSUKAWA (see Ref. [\[26\]](#)) the static analysis of residual magnetic field is carried out defining the reference points, plasma breakdown area and the maximum value of magnetic field and the coil current distribution in the pre-magnetization phase is obtained. The scope of this phase is to produce a region in which the transverse residual magnetic field is as low as possible (null field) and the plasma particles can freely flow along the toroidal magnetic field lines. Of course, 10 PF coil system can produce a variety of null field, each one with proper amount of total supplied flux. The PF coil currents are summarized in the table 3.1, while figure 3.1 shows the various results of breakdown area.

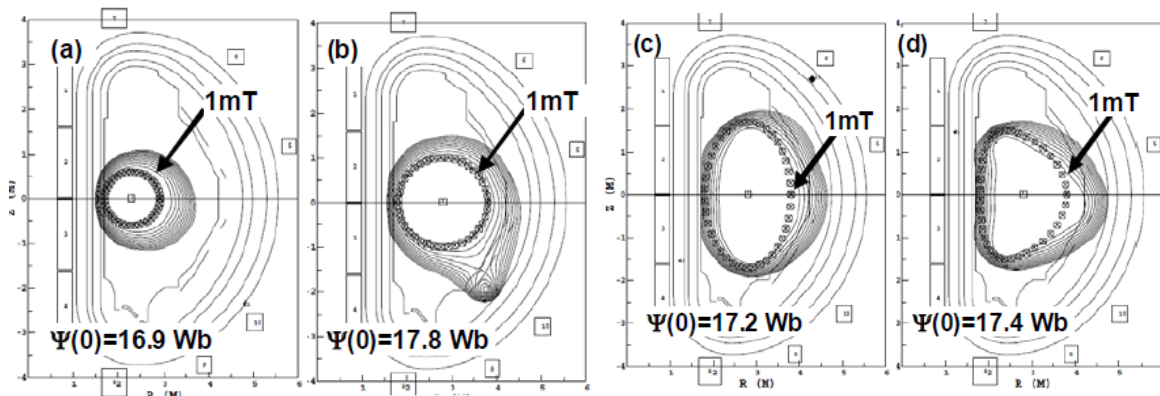


Figure 3.1 - Null field regimes for various currents coils sets. Black lines represent the magnetic field lines configuration. The points individuate the null field region. [\[26\]](#)

Table 3.1 - PF coil currents of static analysis results (kA).

Coil	Case a)	Case b)	Case c)	Case d)
CS1	17.56	19.58	20.00	20.00
CS2	18.20	19.07	18.31	18.52
CS3	18.15	19.02	18.39	18.59
CS4	18.09	20.00	19.64	19.63
EF1	2.777	13.67	1.004	1.074
EF2	-3.035	-0.1112	0.7695	0.4848
EF3	20.00	16.17	13.40	14.22
EF4	13.45	11.38	11.48	12.58
EF5	-1.777	-0.8427	-2.256	-3.498
EF6	0.549	1.298	1.892	2.261

The aim of the study is to reproduce the exact PF coil currents of the static analysis proposed by M. MATSUKAWA in Ref. [26]

Once defined the geometry and the position of passive coils, stabilizing plate, and vacuum vessel, the FEEQS.M code is used in inverse magneto-static mode in order to compute the initial currents in the magnetic coils, the initial available flux and the poloidal magnetic field.

In order to obtain the value of coil currents in the table 3.1, the same CS2 current of the table 3.1 has been fixed for each case, while the value of the central position of the null zone R (m) and the radius of the null zone a (m) have been changed until the value of the other coil currents have been reached.

The results obtained for each case are summarized in the following:

- For case a, imposing $R=2.21\text{m}$ and $a=0.5\text{m}$ the coils currents reported in the second column of table 3.2 are computed. The third column contains the values of coils currents taken from Matsukawa's paper. Figure 3.2 shows the value of poloidal magnetic field and its configuration. The position of the null field has to be as much as possible similar to figure 3.1 a).

Table 3.2 - Coils currents computed using FEEQS for case a).

Coil	FEEQS computation (kA)	Case a (kA)
CS1	17.5978	17.56
CS2	18.2	18.20
CS3	18.1706	18.15
CS4	17.9055	18.09
EF1	2.89339	2.777
EF2	-3.19398	-3.035
EF3	20	20.00
EF4	14.1764	13.45
EF5	-2.41831	-1.777
EF6	0.585986	0.549

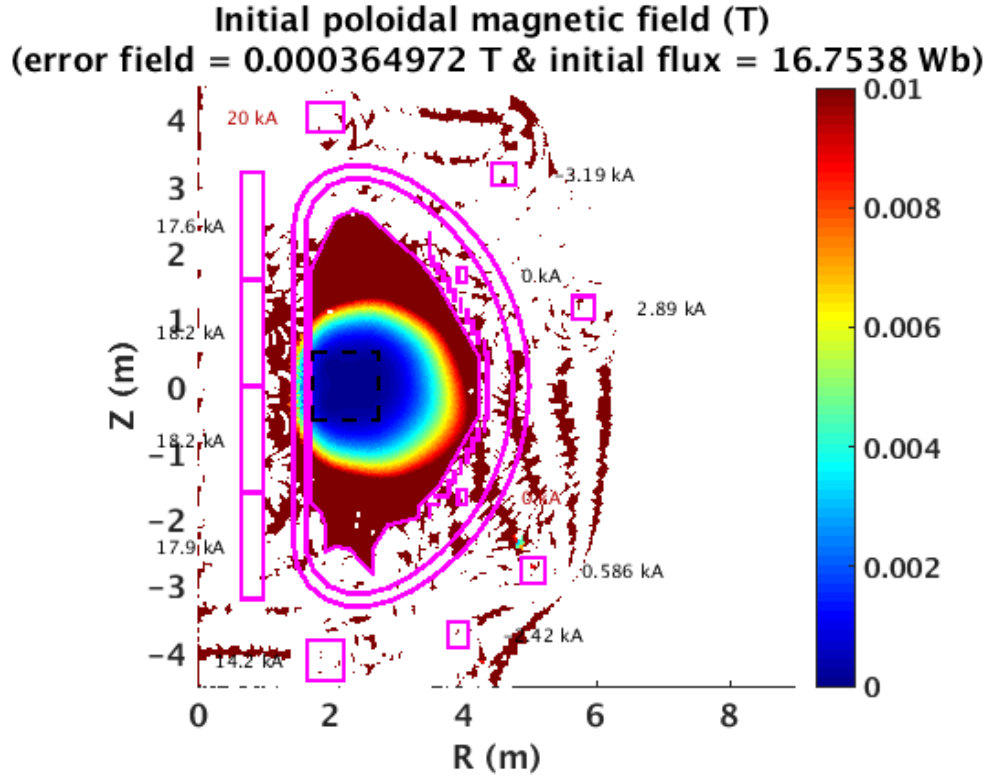


Figure 3.2 - Initial poloidal magnetic field case a).

- For case b, imposing $R=2.6\text{m}$ and $a=0.483\text{m}$ the coils currents reported in the second column of table 3.3 are computed. The third column contains the values of coils current taken from Matsukawa's paper. Figure 3.3 shows the value of poloidal magnetic field and its configuration. The position of the null field has to be as much as possible similar to figure 3.1 b).

Table 3.3 - Coils currents computed using FEEQS for case b).

Coil	FEEQS computation (kA)	Case b (kA)
CS1	19.6312	19.58
CS2	19.07	19.07
CS3	19.0025	19.02
CS4	20	20.00
EF1	13.7595	13.67
EF2	-0.109409	-0.1112
EF3	15.9559	16.17
EF4	11.4769	11.38
EF5	-1.02585	-0.8427
EF6	1.31303	1.298

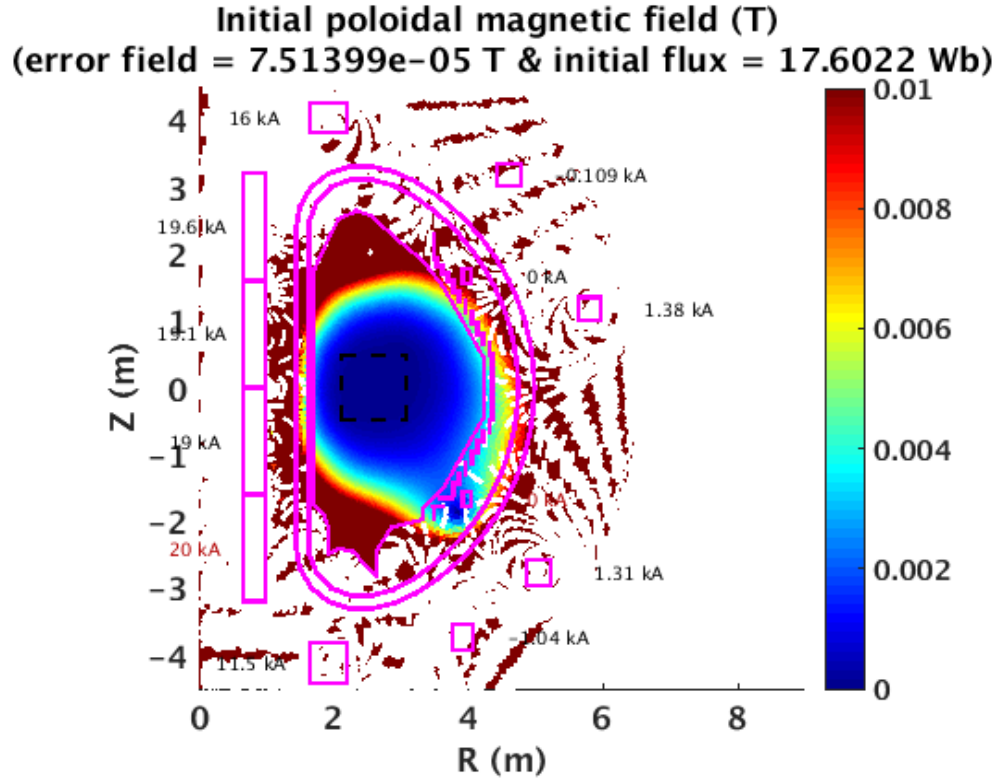


Figure 3.3 - Initial poloidal magnetic field case b).

- For case c, imposing $R=2.9\text{m}$ and $a=0.65\text{m}$ the coils currents reported in the second column of table 3.4 are computed. The third column contains the values of coils current taken from Matsukawa's paper. Figure 3.4 shows the value of poloidal magnetic field and its configuration. The position of the null field has to be as much as possible similar to figure 3.1 c).

Table 3.4 - Coils currents computed using FEEQS for case c).

Coil	FEEQS computation (kA)	Case c (kA)
CS1	19.1009	20.00
CS2	18.31	18.31
CS3	18.209	18.39
CS4	19.2901	19.64
EF1	1.041	1.004
EF2	0.400387	0.7695
EF3	14.4465	13.40
EF4	11.8685	11.48
EF5	-2.78599	-2.256
EF6	1.99428	1.892

Initial poloidal magnetic field (T)
(error field = 7.59749×10^{-5} T & initial flux = 16.9057 Wb)

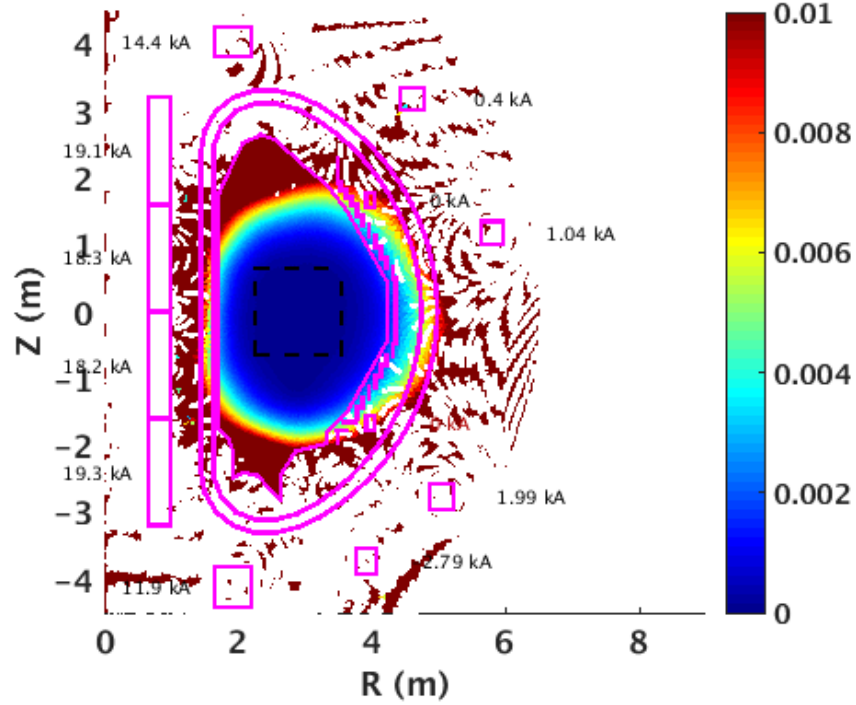


Figure 3.4 - Initial poloidal magnetic field case c)

- For case d, imposing $R=2.9\text{m}$ and $a=0.65\text{m}$ the coils currents reported in the second column of table 3.5 are computed. The third column contains the values of coils current taken from Matsukawa's paper. Figure 3.5 shows the value of poloidal magnetic field and its configuration. The position of the null field has to be as much as possible similar to figure 3.1 d).

Table 3.5 - Coils currents computed using FEEQS for case d).

Coil	FEEQS computation (kA)	Case d (kA)
CS1	19.32	20.00
CS2	18.52	18.52
CS3	18.4178	18.59
CS4	19.5114	19.63
EF1	1.05294	1.074
EF2	0.404979	0.4848
EF3	14.6122	14.22
EF4	12.0046	12.58
EF5	-2.81794	-3.498
EF6	2.01716	2.261

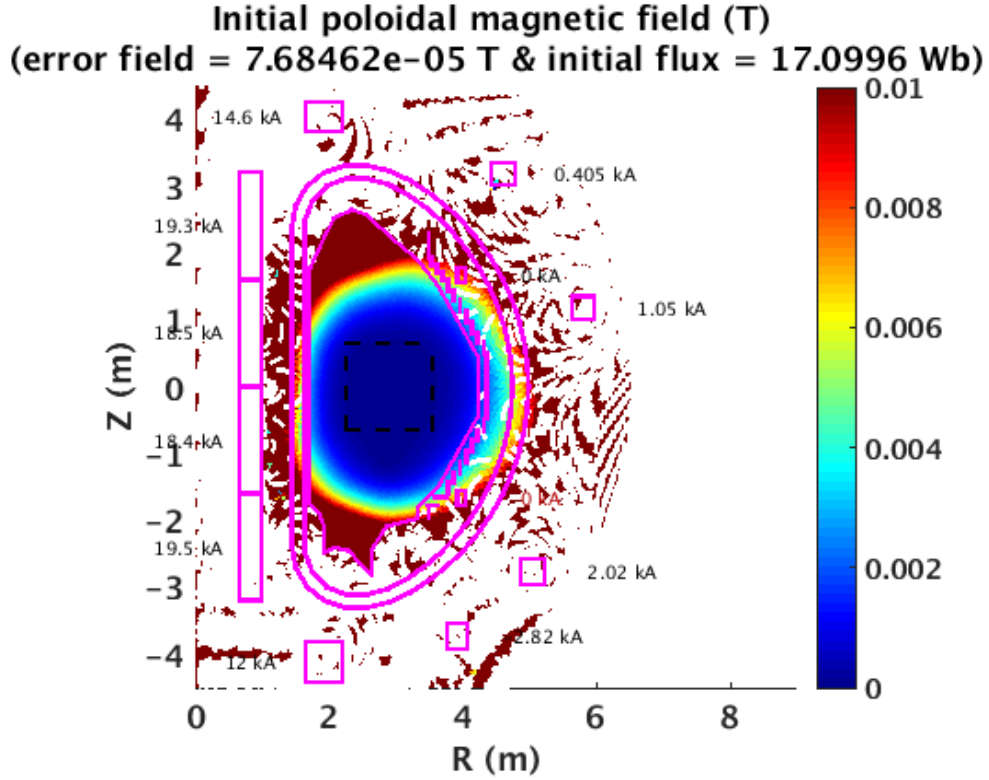


Figure 3.5 - Initial poloidal magnetic field case d).

As it is possible to observe from figures from 3.2 to 3.5 and tables from 3.2 to 3.5, FEEQS used in the inverse magneto-static mode gives results that are in very good agreement with those reported in Ref. [\[26\]](#)

3.2 METIS and FEEQS for JT-60SA operational scenarios

The JT-60SA tokamak has been designed to realize a wide range of plasma equilibria using superconducting toroidal and poloidal field coils. As it is possible to check in the article *Development of operation scenario for plasma breakdown and current ramp-up phases in JT-60SA tokamak*, published by H. Urano (see Ref. [\[27\]](#)), the operation scenarios have been developed and verified in simulation using the TOSCA code.

The aim of the study is to obtain the same plasma parameters reported in this paper using the METIS and the FEEQS codes. Once the input parameters have been set, METIS computes the flux consumption. Then, all of the output data are used in FEEQS. It uses a free boundary equilibrium in inverse mode method in order to reach the same coil currents reported in the previous paper.

For this comparison, the scenario #2 of JT-60SA tokamak is chosen. In particular, this scenario requires full pre-magnetization of CS coils which enables to operate in a long inductive discharge at high plasma current (I_p) of 5.5 MA. Moreover, an external heating power up to 41MW is provided using an ECRH (7MW) and the two types of NBI (respectively 24MW and 10MW).

The magnetic flux consumption represents the main parameter to estimate the coil currents. The difference between TOSCA and FEEQS consist of the calculation of this parameter. The first one uses the following formula:

$$\Delta\Psi = L_p\Delta I_p + C_{Ejima}\mu_0 R_p\Delta I_p$$

Where the plasma self-inductance (L_p), the increment of the plasma current (ΔI_p), the Ejima factor ($C_{Ejima} = 0.45$), and the plasma major radius (R_p) are set as input in the code. μ_0 is the permeability of the vacuum.

Moreover the value of $I_i(3)$ and β_p for the plasma have been chosen consistently by the spatial profiles of current density and plasma pressure with the auxiliary heating system calculated using the ACCOME code that evaluates the current density profile of the bootstrap, NB-driven and ohmic components from NB heating geometry and the spatial profiles of plasma density and temperature. At this point, the TOSCA code computes a set of the coil currents and voltages for each equilibrium.

As it is possible to see from Ref [27], the divertor configuration is formed at $t=3.74s$ when I_p reaches 1.51 MA and Ψ_p decreases from 17.7 to 8.1 Wb. Ψ_p decreases gradually through the inductive and resistive flux consumption from 17.7 Wb at the initial plasma to -17.8 Wb at the SOF (Start of Flat-top) of $t=15.14s$. The plasma parameter at the end of the ramp-up ($t=24s$) are $I_p=5.5$ MA, $\Psi_p=-17.0$ Wb, $k=1.92$, $I_i(3)=0.75$, $\beta_p=0.67$ and $H=1.3$.

The FEEQS code is a 2D Free Boundary MHD Equilibrium code that works in an inverse Poynting mode, in other words provides the set of PF coils currents that allow to best match a desired plasma boundary. In order to do that, the code has to solve the Grad-Shafranov equation starting from the current density distribution in the plasma. The constraints used by FEEQS are P' and FF' profiles and plasma shape taken from METIS, plasma currents, LCFS poloidal flux and coils limits. As a result FEEQS gives the real FBE solution, waveforms of coils currents for full simulation, forces and maximum magnetic fields on coils and estimation of voltages on coils and currents in passive structures.

The first step of the study is to change the input METIS parameters starting from scenario 2 of JT-60SA in order to obtain similar behavior of Ψ_p , q_{95} , $I_i(3)$ and β_p and similar value of C_{Ejima} factor as in Urano's paper. The input data are made of waveforms and consist of real controllable parameters during a real experiment as plasma current, injected power for heat sources, line-averaged density, plasma geometry, and non-controllable parameters as effective charge, isotopic plasma composition, confinement enhancement factor.

The waveform of plasma current is taken from Urano's paper and only the waveform of the line-averaged density and injected power for heat source have been changed.

Two different solutions are taken into account. The first one has as goal of obtaining the same waveforms of $I_i(3)$ and β_p . In this case, the C_{Ejima} factor is equal to 0.33. The parameters analyzed are plotted in the figure 3.6.

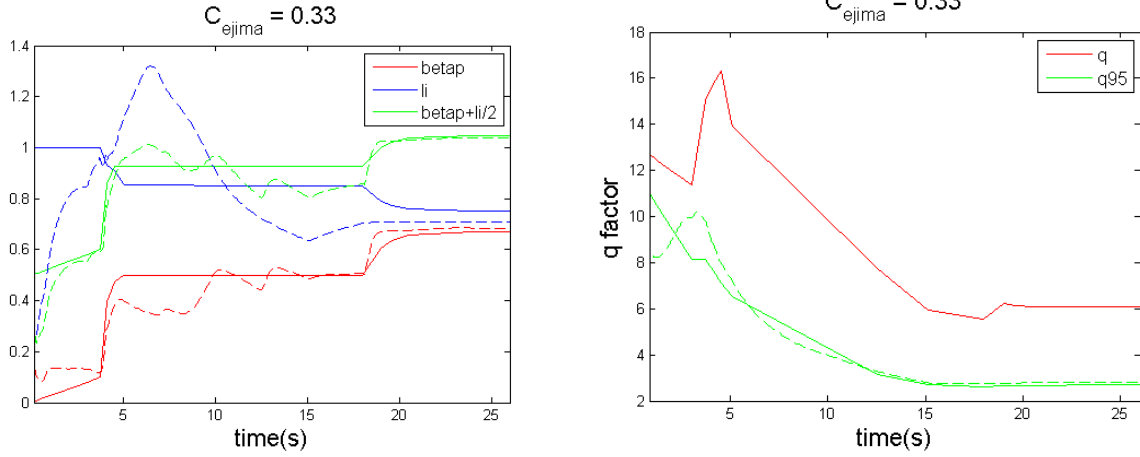


Figure 3.6 - Solid lines correspond to the data taken from Ref [27], the dashed lines are computed by METIS code. Left figure shows $li(3)$, β_p and $li/2 + \beta_p$ profiles of case 1. Right figure shows the central value of quality factor (q) and the safety factor at 95% of poloidal flux (q_{95}) profiles of case 1.

In the second case the aim is to reach the same value of C_{ejima} factor (0.45). The behaviors of $li(3)$, β_p and q_{95} have been computed as consequence (figure 3.7).

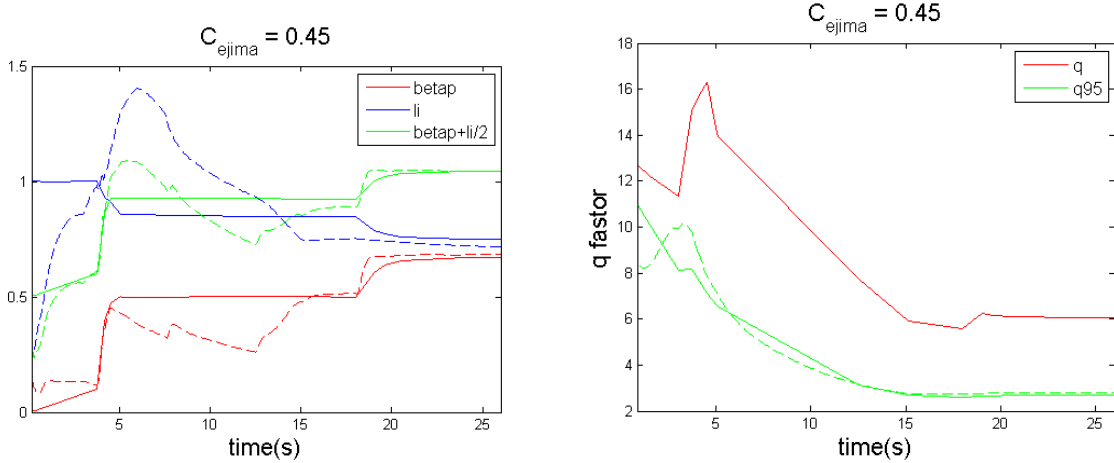


Figure 3.7 - Solid lines correspond to the data taken from Ref [27], the dashed lines are computed by METIS code. Left figure shows $li(3)$, β_p and $li/2 + \beta_p$ profiles of case 2. Right figure shows the central value of quality factor (q) and the safety factor at 95% of poloidal flux (q_{95}) profiles of case 1.

Starting from these two cases, the flux consumptions are computed and compared with Urano's data. This leads to have a first idea about the coil currents behaviors because the CS1 current has the same behavior of the flux consumption. In order to compare the two fluxes computed by METIS with Urano's data, they are multiplied by a factor of 2π due to the different definitions used in METIS and in Urano's paper. They are plotted in figure 3.8.

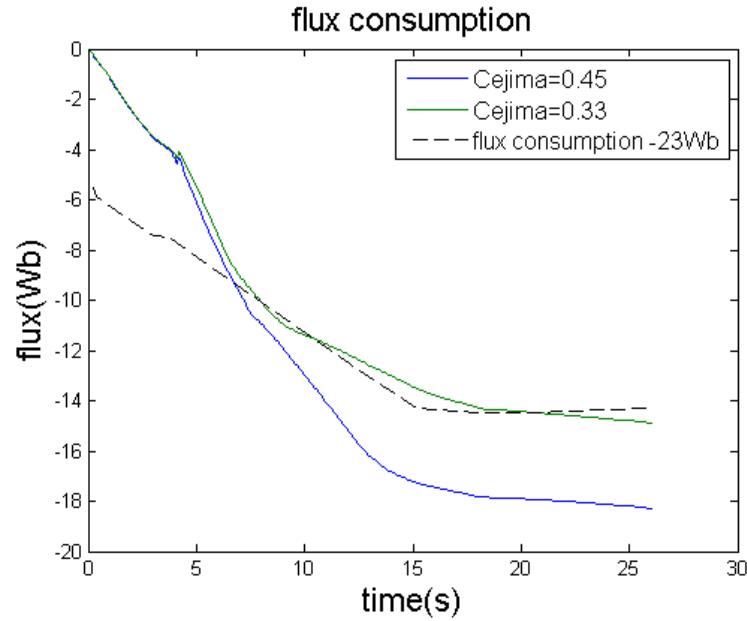


Figure 3.8 - Fluxes consumptions of two cases compared to the reference one. 23 Wb are subtracted to the reference flux consumption in order to overlap the curves.

According to the results obtained, the first case has been chosen because it shows a more similar behavior with respect to Urano's one.

The study is continued trying different attempts in order to reduce the slope of the first part of the curve. In order to do that, the waveforms of line-averaged density, ECRH and NBIs heating have been changed again. Different attempts made are plotted in figure 3.9.

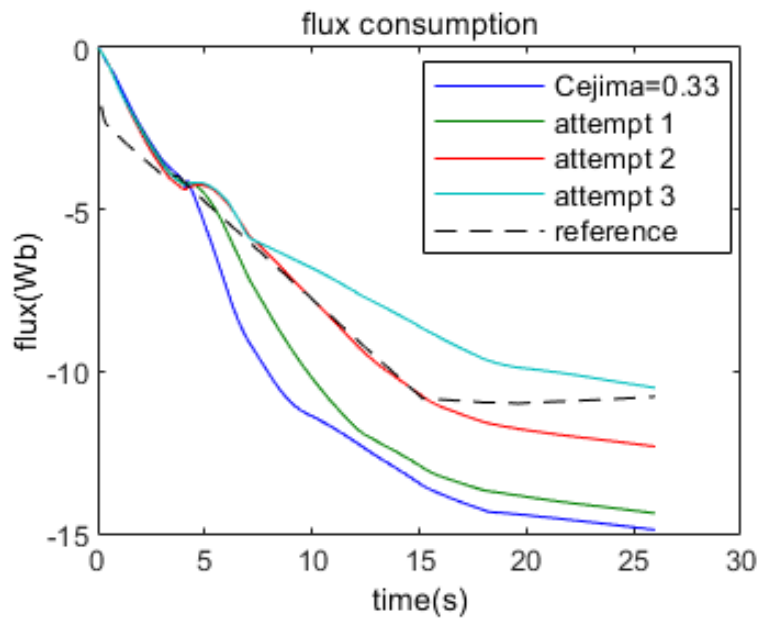


Figure 3.9 - Different attempts compared with reference one. 19 Wb are subtracted to the reference flux consumption in order to overlap the curves.

The attempt 2 has been chosen and other changes have been done until reaching the final attempt. This one is plotted on the figure 3.10. Also the behavior of the input parameters that have been changed in order to reach this final configuration are plotted in figures from 3.10 to 3.12.

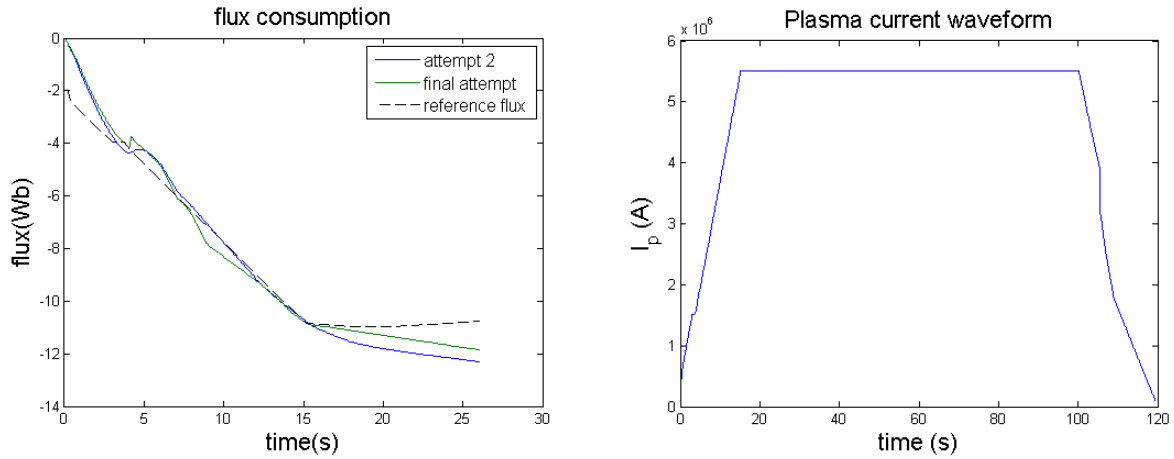


Figure 3.10 – Left: final attempt chosen compared with reference one. Right: plasma current behavior to generate final configuration.

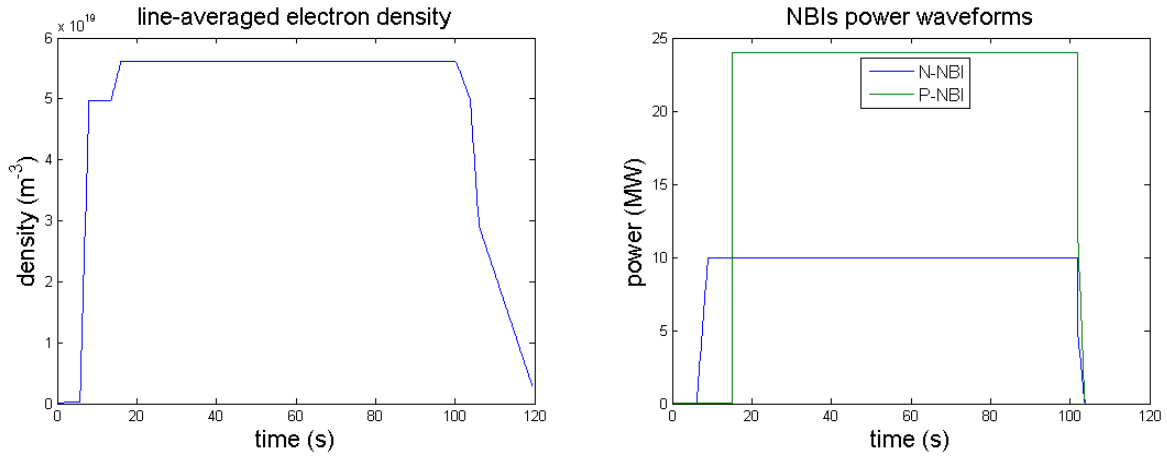


Figure 3.11 – Left: line-averaged density behavior to generate final configuration. Right: NBIs heating behavior to generate final configuration.

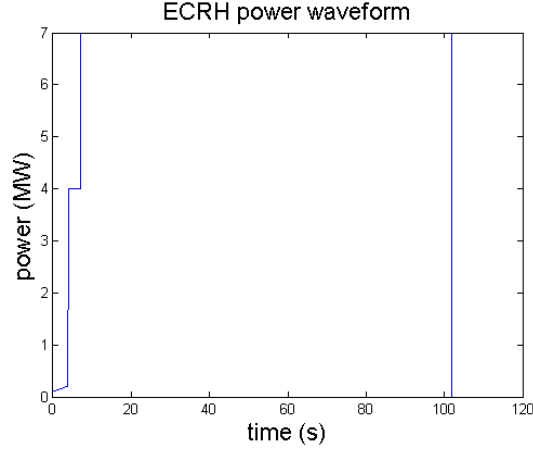


Figure 3.12 - ECRH heating behavior to generate final configuration.

The next step consists of using this final configuration as input for FEEQS in order to compute coils currents and to compare them to Urano's results. The first run of the code is made with the flux offset in automatic mode. The flux offset is used to match METIS current diffusion LCFS poloidal flux with FEEQS LCFS poloidal flux. The automatic mode means that the offset is automatically computed taking into account the flux consumption estimated for the breakdown and the flux leakage computed with the help of current diffusion equation between the end of the breakdown and the first time of ramp-up. Otherwise, it is possible to use the manual mode and to set the value of the offset that better matches the two LCFS poloidal fluxes. The value of the offset is expressed in Weber, in fact, it consists in a precise number that it is added to the LCFS poloidal flux computed by METIS.

The regularization weight is set to 10^{-20} . Statistically speaking, the regulation weight are known as Tikhonov regularization and it is a method of regularization of ill-posed problems. It is particularly useful to mitigate the problem of multicollinearity in linear regression, which commonly occurs in models with large numbers of parameters. In general, the method provides improved efficiency in parameter estimation problems. Suppose that the aim is to find a vector x such that:

$$Ax = b$$

Where the matrix A and the vector b are known. The standard approach is ordinary least squares linear regression. However, if no x satisfies the equation or more than one x does, the problem is said to be ill posed. Therefore, in solving the inverse-problem, in order to give preference to a particular solution with desirable properties, a regularization term can be included in the minimization:

$$\|Ax - b\|_2^2 + \|\Gamma x\|_2^2$$

For some suitably chosen Tikhonov matrix. In many cases, this matrix is chosen as a multiple of the identity matrix ($\Gamma = \alpha I$) giving preference to solutions with smaller norms. This regularization improves the conditioning of the problem, thus enabling a direct numerical solution. The effect of regularization may be varied by the scale of matrix Γ . The optimal regularization parameter α is usually unknown and often in practical problems is determined by an *ad hoc* method. [\[28\]](#)

For the FEEQS specific case, the same plasma equilibria can be obtained with a different set of coils current. The regulation term is used to force the code to find the value of the current in the following time slice as close as possible to the computed value. At the beginning of the run, FEEQS searches for a suitable time slice as starting point in which the initial convergence loop is computed. After finding the starting time slice, FEEQS estimates the best regularization weight computing the initial loop with each integer number between the minimum and the maximum value of regularization weight that have been set. The constraint forces on coils and the constraint forces between coils are taken into account in all simulations. Then, the flux offset is shifted in manual mode with value 9 Wb in order to move the curves and to overlap them on the reference ones. The results are plotted in the figures from 3.13 to 3.17.

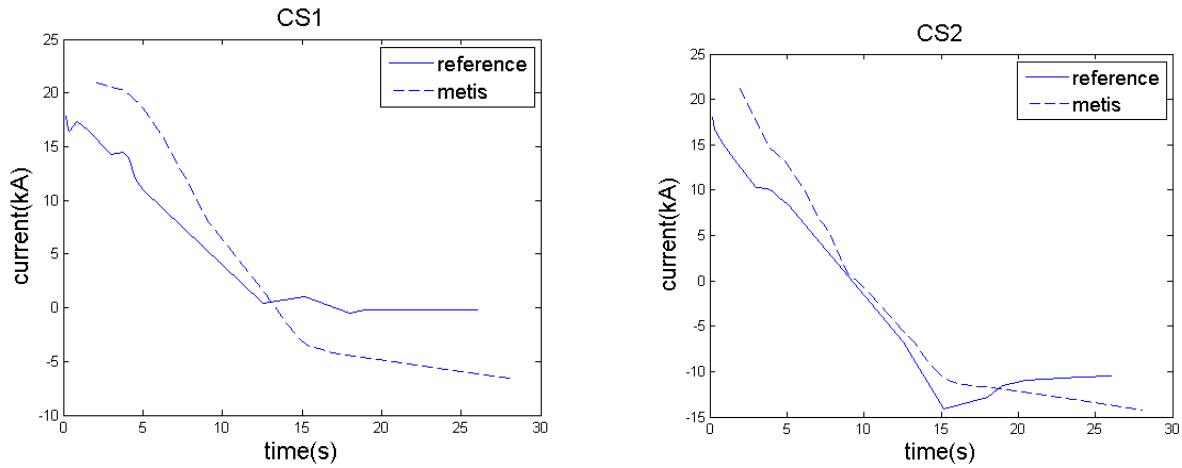


Figure 3.13 – Left: current in CS1 compared with reference. Right: current in CS2 compared with reference.

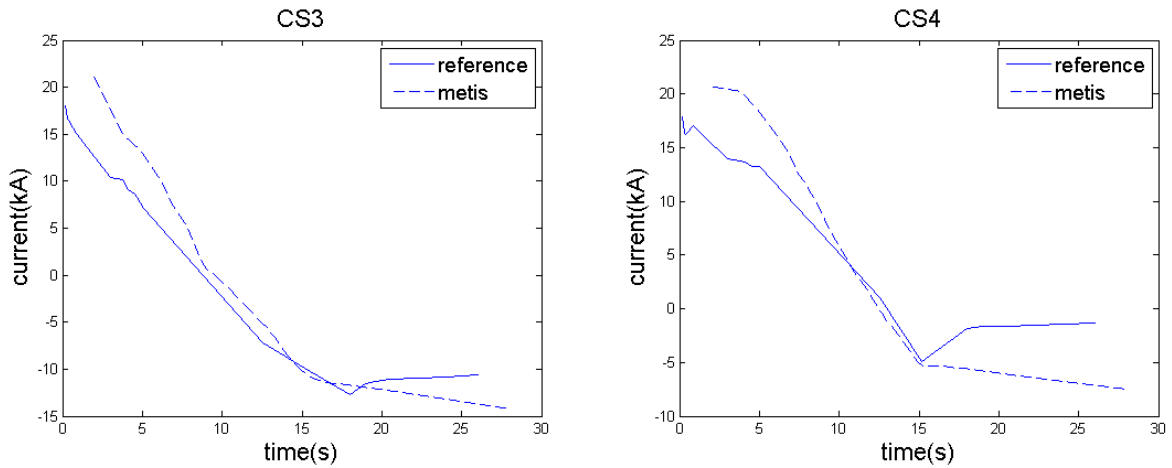


Figure 3.14 – Left: current in CS3 compared with reference. Right: current in CS4 compared with reference.

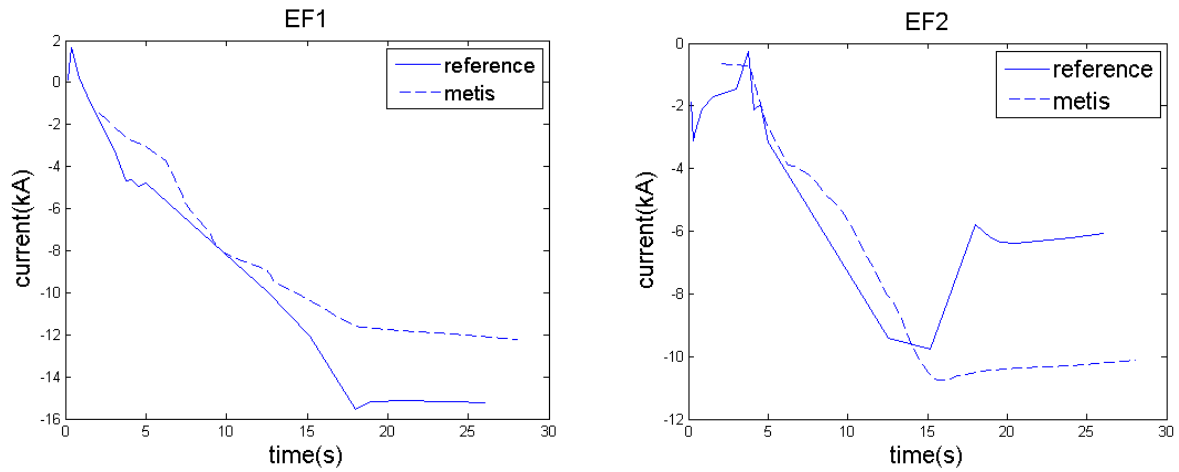


Figure 3.15 – Left: current in EF1 compared with reference. Right: current in EF2 compared with reference.

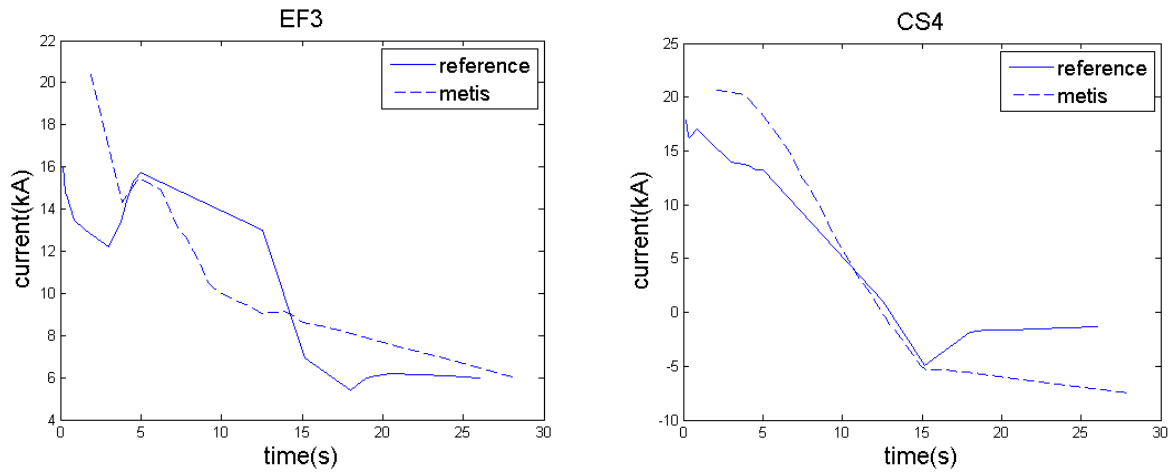


Figure 3.16 – Left: current in EF3 compared with reference. Right: current in EF4 compared with reference.

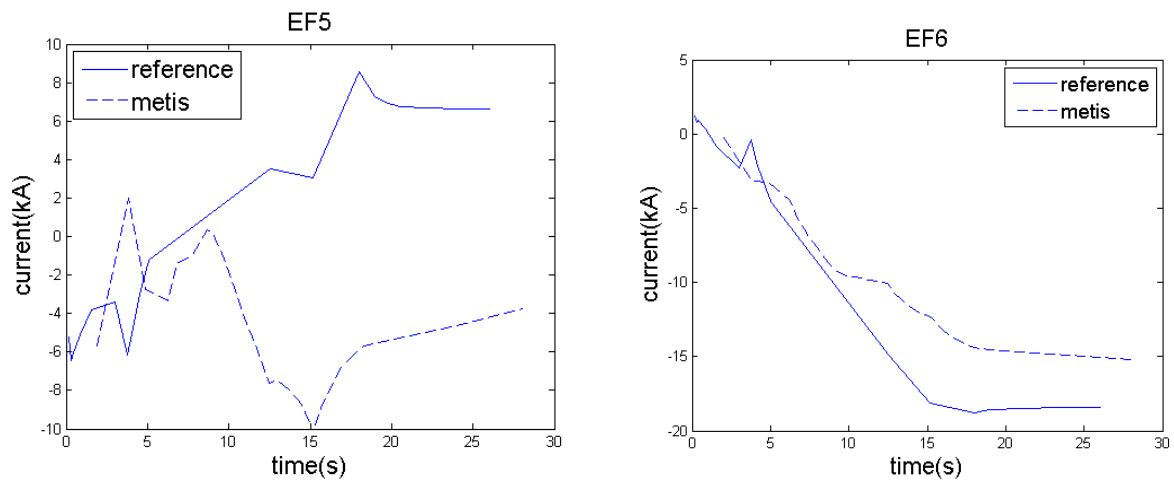


Figure 3.17 – Left: current in EF5 compared with reference. Right: current in EF6 compared with reference.

Once the value of flux offset is defined, also the regulation weights have been adjusted. The only case that leads to different waveforms consists of setting the regulation weight to 10^{-14} . The results are plotted below in figures 3.18 to 3.22.

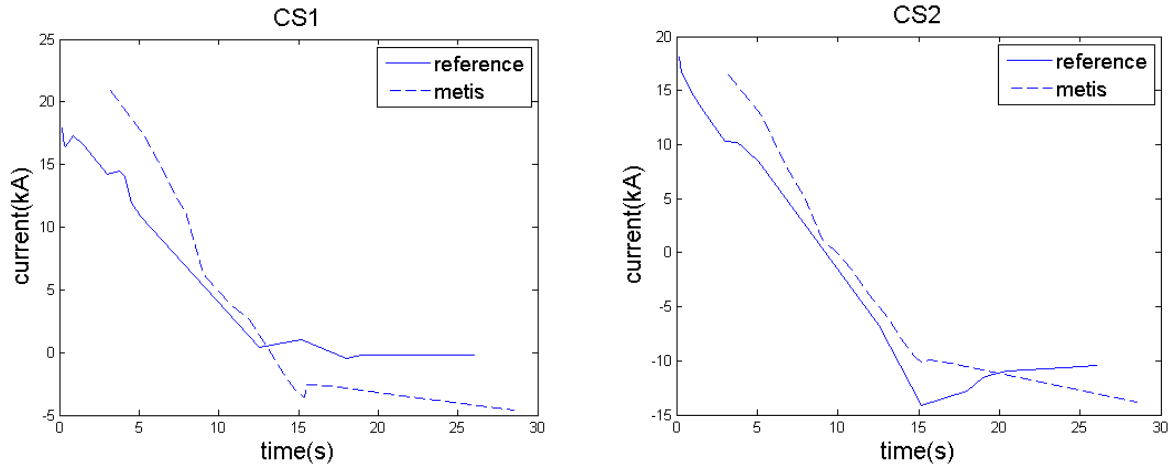


Figure 3.18 – Left: current in CS1 compared with reference. Right: current in CS2 compared with reference.

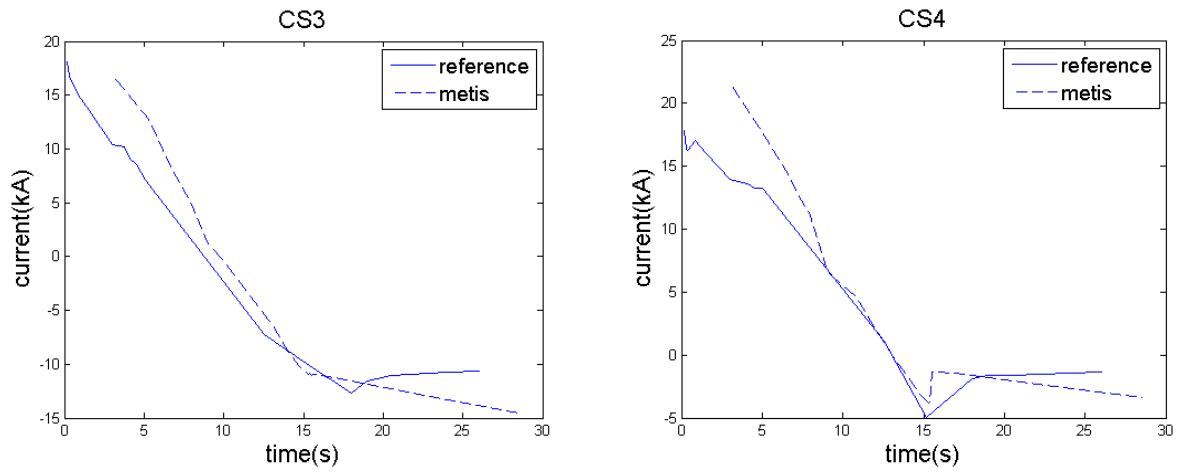


Figure 3.19 – Left: current in CS3 compared with reference. Right: current in CS4 compared with reference.

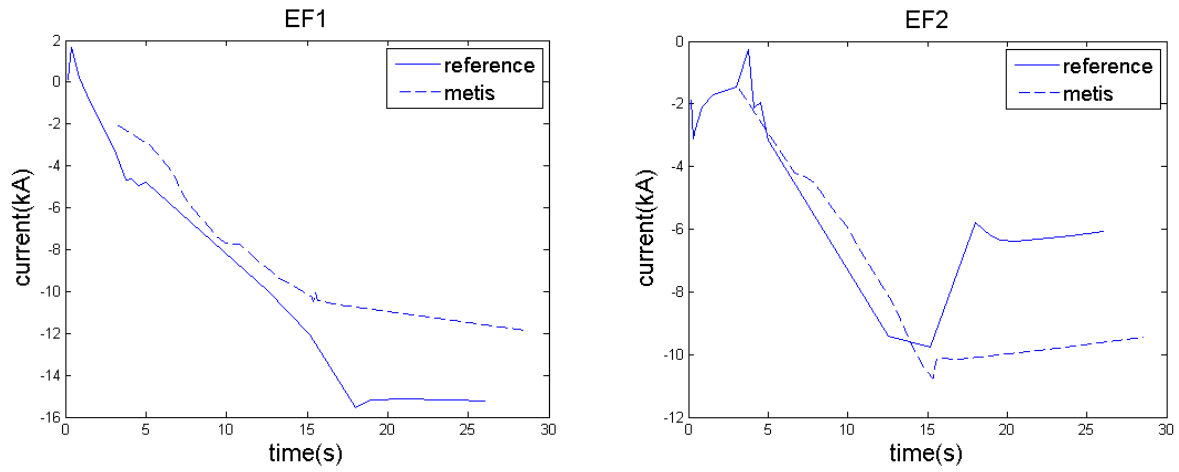


Figure 3.20 – Left: current in EF1 compared with reference. Right: current in EF2 compared with reference.

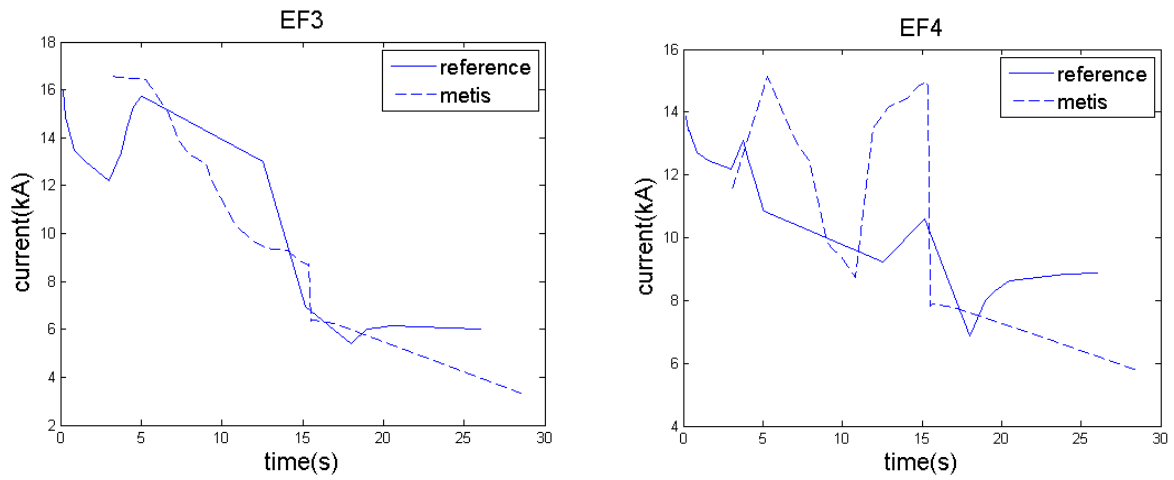


Figure 3.21 – Left: current in EF3 compared with reference. Right: current in EF4 compared with reference.

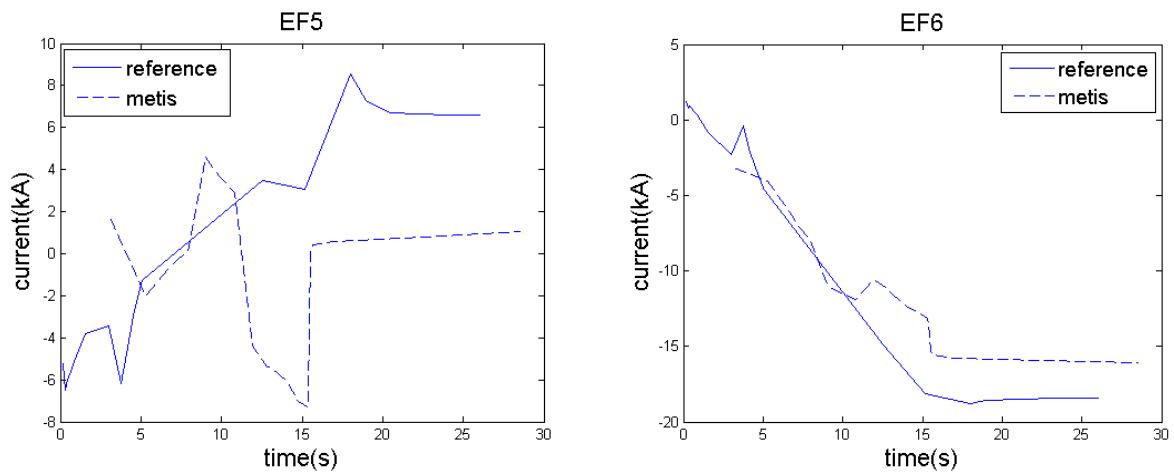


Figure 3.22 – Left: current in EF5 compared with reference. Right: current in EF6 compared with reference.

The results obtained are not precisely matching, especially for EF4 and EF5. Nevertheless, the currents behaviors inside the solenoids coils are similar to the references.

In order to understand if imperfect match between Urano's data and METIS/FEEQS results is due to a problem inside the free-boundary code, a direct benchmark between TOSCA and FEEQS has been made without METIS in the loop. Two different cases have been considered. In both cases, the data have been extracted from the official data repository DMS, in the zip archive named "JT-60SA_TOSCA_Scenario2_Case1_Hayashi_N_20150430.ZIP", and FEEQS has been run in inverse mode without current in passives structures and with a regularization weight of 10^{-18} . Also parameters for P' and FF' profiles have been set to match β_p and I_i as well as possible.

The first case consists of setting CS1 to CS4 currents to the value taken from TOSCA and computing EF currents using FEEQS. The results are plotted below in figure 3.23 and figure 3.24.

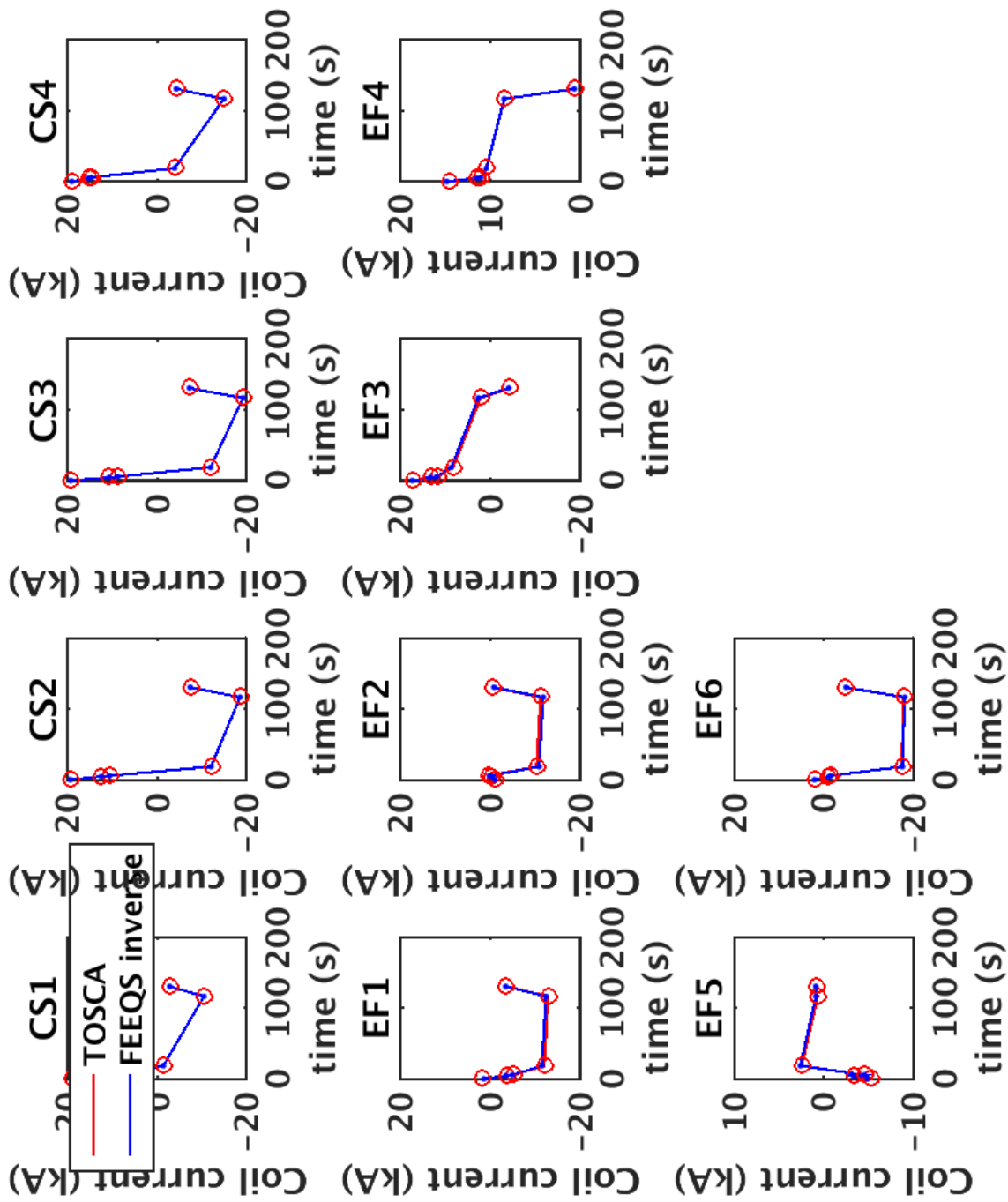


Figure 3.23 - Comparison between coil currents from FEEQS and TOSCA case 1. CS1 to CS4 currents are set to the value taken from TOSCA and EF currents are computed using FEEQS.

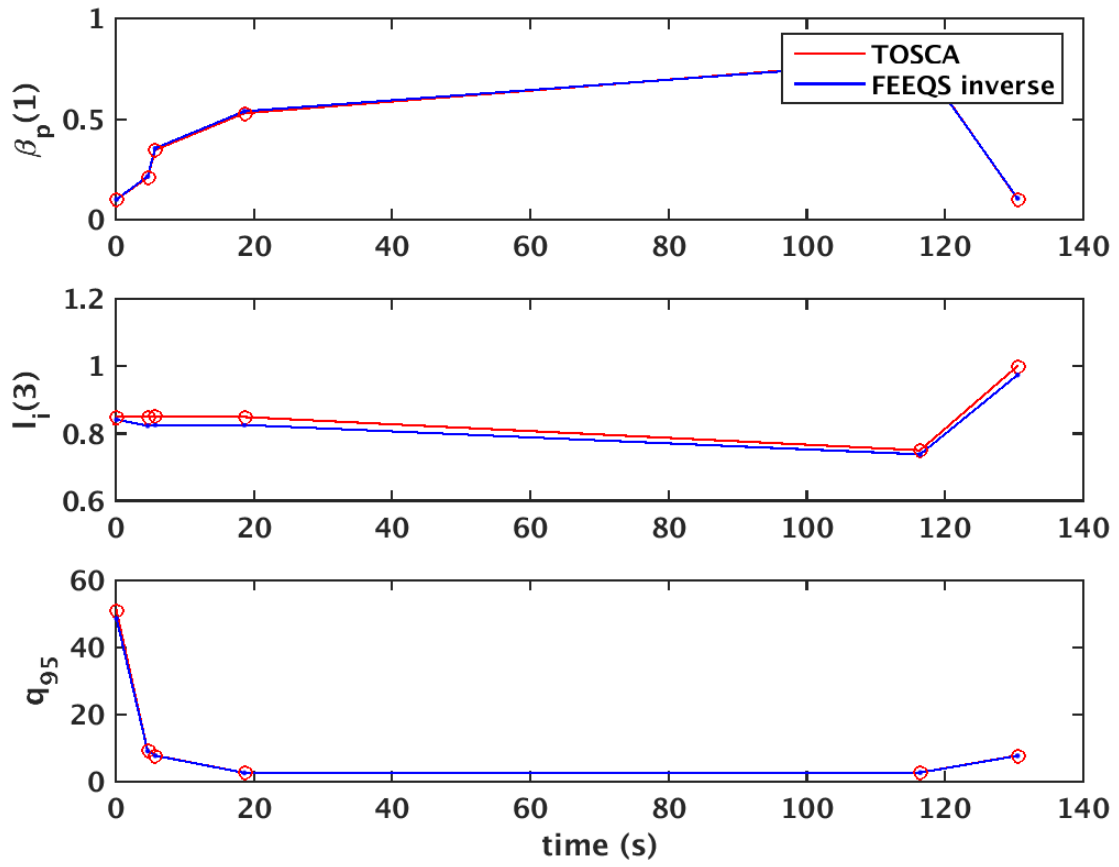


Figure 3.24 - comparison between I_i , β_p and q_{95} from FEEQS and TOSCA case 1. CS1 to CS4 currents are set to the value taken from TOSCA and EF currents are computed using FEEQS.

The second case consists of setting CS2 current to the values taken from TOSCA and computing all of the other currents using FEEQS. The figures 3.25 and 3.26 show the results obtained.

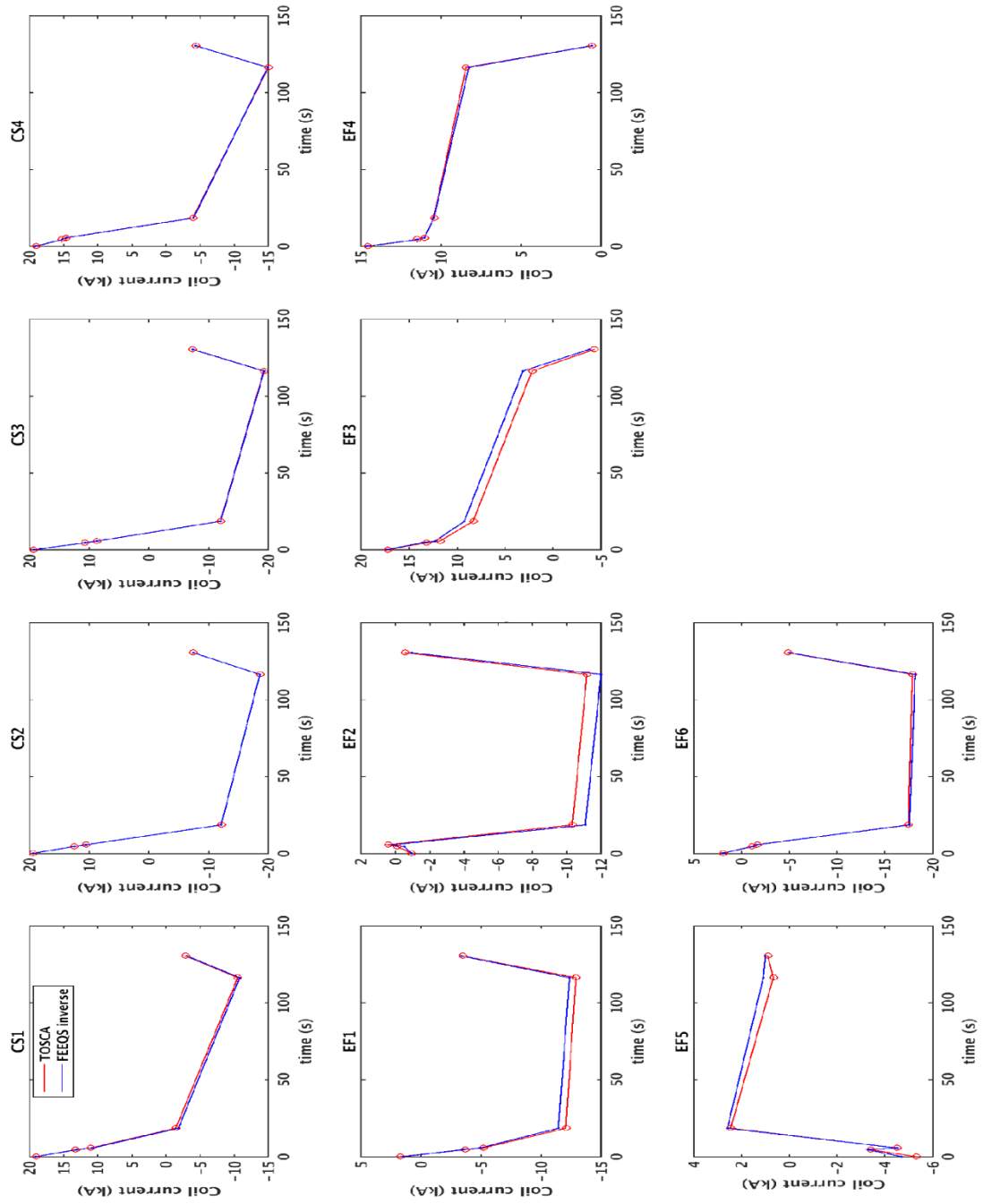


Figure 3.25 - Comparison between coil currents from FEEQS and TOSCA case 2. CS2 current is set to the values taken from TOSCA and all of the other currents are computed using FEEQS.

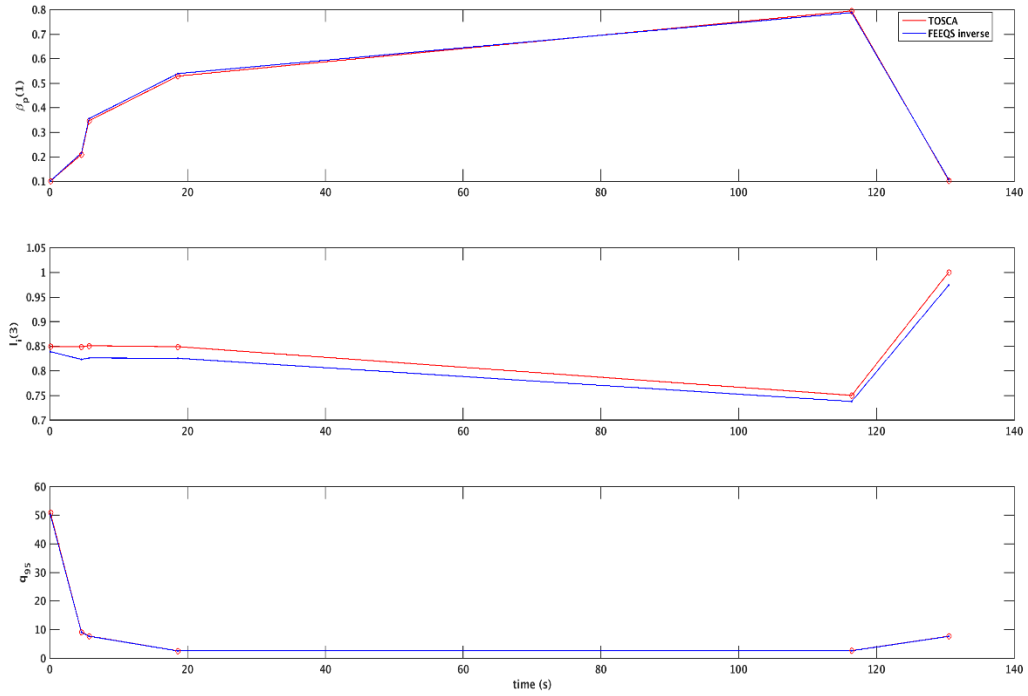


Figure 3.26 - Comparison between I_i , β_p and q_{95} from FEEQS and TOSCA case 2. CS2 current is set to the values taken from TOSCA and all of the other currents are computed using FEEQS.

As it can be seen, FEEQS results match TOSCA data well, which means that the two codes have the same contents and similar accuracy. The small differences between the two probably come from the currents in passive structures, set to be 0. Considering that there is no problem in the data exchanging from FEEQS to METIS, the difference in the coil currents is due to the difference in plasma shape and in P' and in FF' plasma profiles.

The last step consists of comparing the coil currents obtained above with those computed uploading in METIS the LCFS generated by FEEQS. This step is useful to obtain a better convergence in the loop. To run METIS for the first time, a LCFS given by points is used. This means that METIS computes a plasma equilibrium that ensures a certain LCFS given as an input. Once FEEQS is run, it is able to compute the LCFS as real solution of the free-boundary equation problem. Therefore, it is possible to update the new LCFS in METIS and run again the code. $I_i(3)$, β_p and elongation are computed and compared. The new outputs are used to run FEEQS and to re-compute the coil currents. The figure from 3.27 to 3.31 show the coil currents behavior, figures from 3.32 to 3.34 show the comparison between plasma parameters. All the plots are made using a regularization weight 10^{-18} and an offset flux of 9Wb.

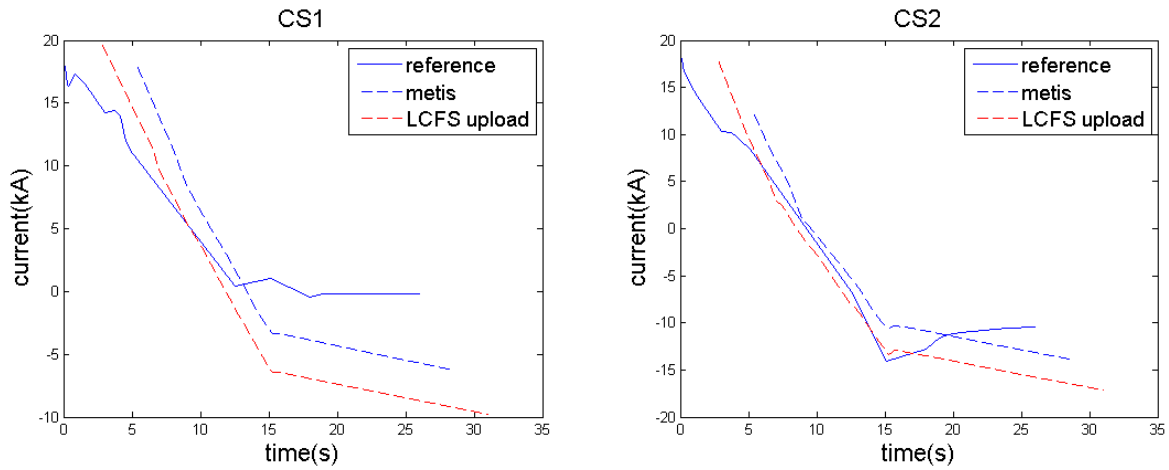


Figure 3.27 – Left: CS1 current comparison between first calculation and uploaded LCFS calculation. Right: CS2 current comparison between first calculation and uploaded LCFS calculation.

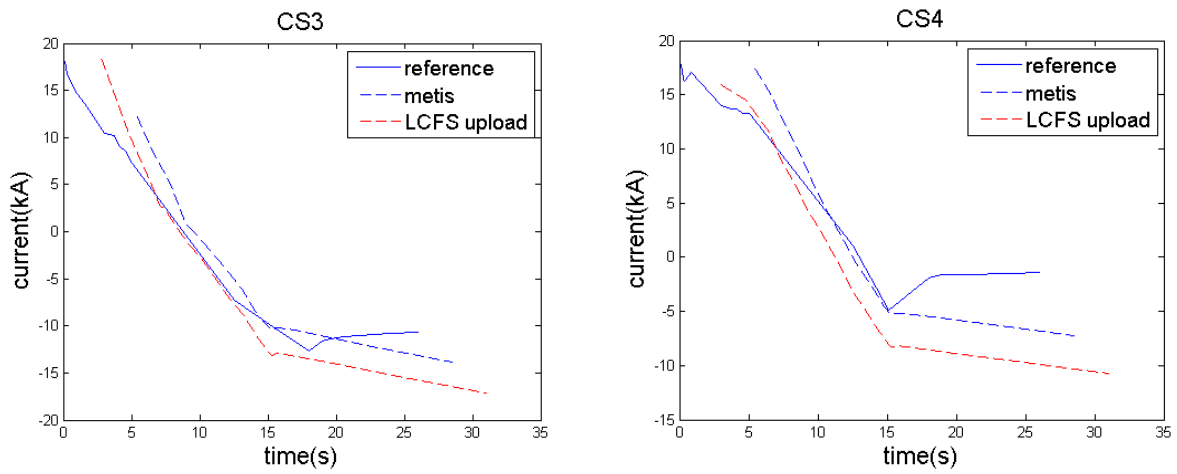


Figure 3.28 – Left: CS3 current comparison between first calculation and uploaded LCFS calculation. Right: CS4 current comparison between first calculation and uploaded LCFS calculation.

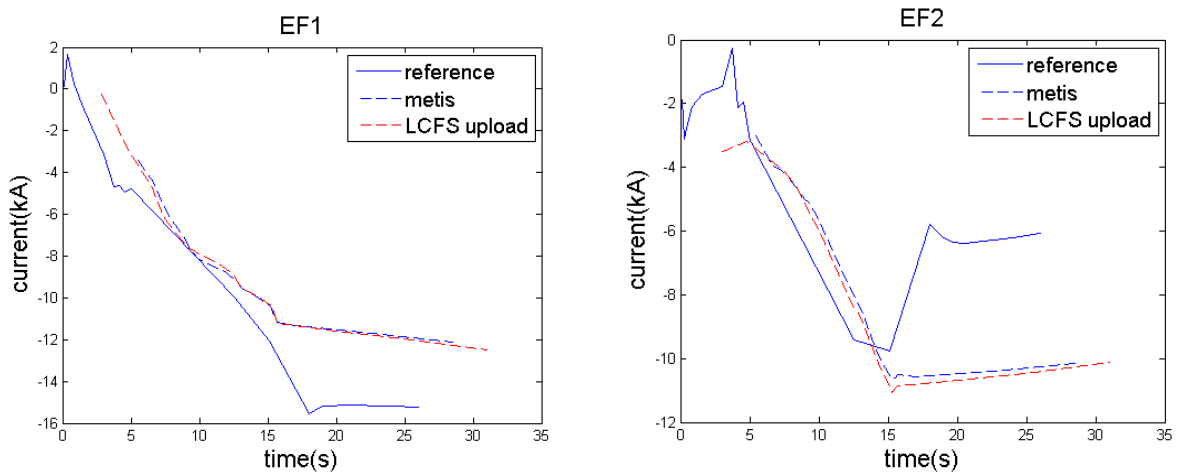


Figure 3.29 – Left: EF1 current comparison between first calculation and uploaded LCFS calculation. Right: EF2 current comparison between first calculation and uploaded LCFS calculation.

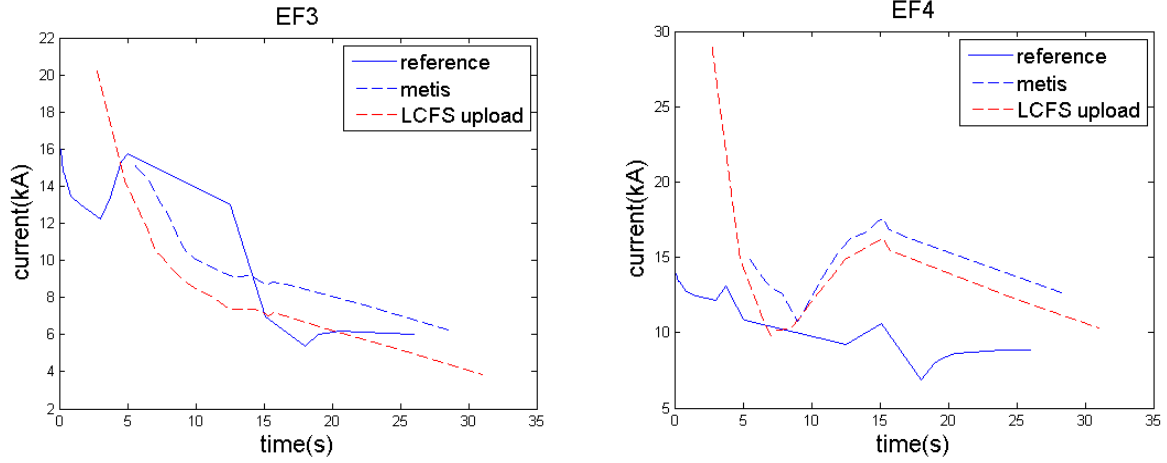


Figure 3.30 – Left: EF3 current comparison between first calculation and uploaded LCFS calculation. Right: EF4 current comparison between first calculation and uploaded LCFS calculation.

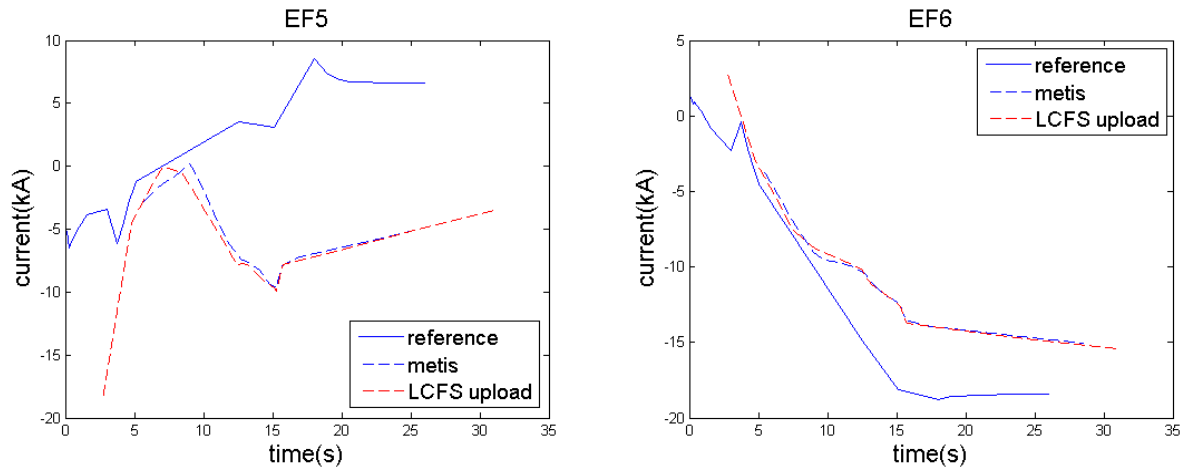


Figure 3.31 – Left: EF5 current comparison between first calculation and uploaded LCFS calculation. Right: EF6 current comparison between first calculation and uploaded LCFS calculation.

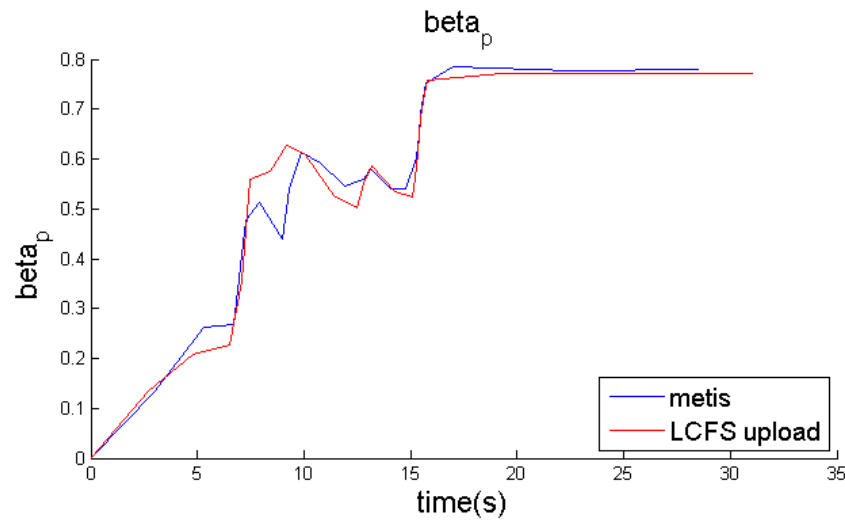


Figure 3.32 – β_p comparison between first calculation and uploaded LCFS calculation.

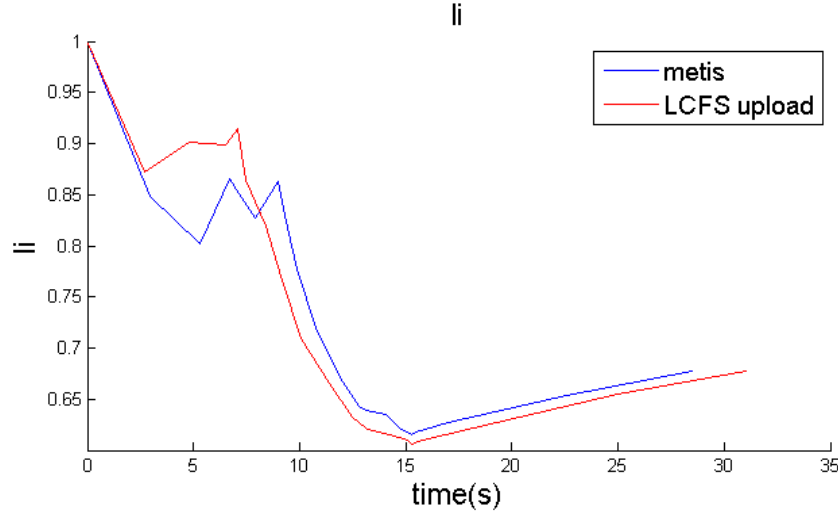


Figure 3.33 - i_l comparison between first calculation and uploaded LCFS calculation.

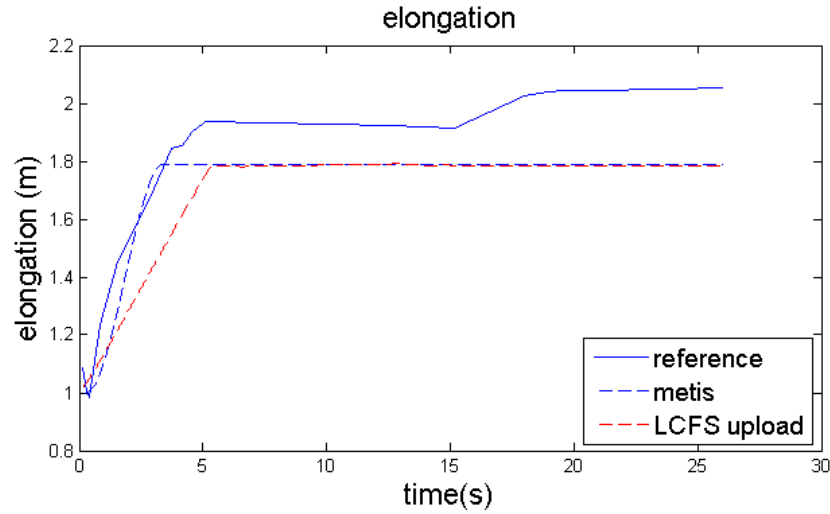


Figure 3.34 - elongation comparison between first calculation and uploaded LCFS calculation.

As it can be seen from the figures, the behaviors of the coil currents are quite similar and the difference in the values are due to different plasma shape parameters. In fact, the last plot shows a different value of the elongation of the plasma and this leads to different values of coil currents. In METIS it is possible to directly check the changing in LCFS plotting the LCFS given by points and the LCFS computed by FEEQS. Figure 3.35 shows this difference. All of the isoflux surfaces have been computed and plotted. The dashed lines correspond to the LCFS computed by FEEQS, while the solid lines are referred to the LCFS given by points.

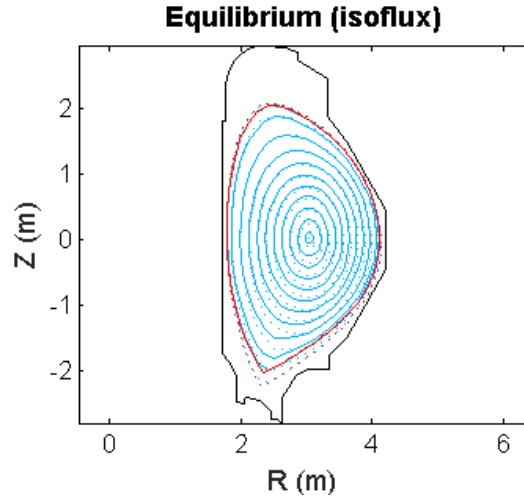


Figure 3.35 – Isoflux surfaces computed by METIS for the case in which the LCFS is given by points (solid lines) and for the case in which the LCFS is computed by FEEQS and uploaded in METIS (dashed lines).

3.3 Operation of scenarios

JT-60SA is designed to investigate how to optimize scenarios to support both ITER and DEMO. Thanks to its intrinsic flexibility it is possible to analyze a variety of scenarios that are: pulsed, inductive standard H-mode scenarios (#2 Full Ip inductive 41MW); advanced inductive, high- β , low magnetic shear scenarios (#4-2 Advanced inductive 37MW); and fully non-inductive, steady-state, advanced scenarios (#5-1 High β_N Full CD 37MW). The main parameters of the reference scenarios are reported in the figure 3.36. [\[17\]](#)

Table 1-1 Typical Parameters of JT-60SA

Parameters	#2 Full Ip Inductive 41MW	#4-1 ITER-like- Shape Inductive 34MW	#4-2 Advanced inductive (hybrid) 37MW	#5-1 High β_N Full CD 37MW	#5-2 High β_N Full CD 31MW
Plasma current, I_p (MA)	5.5	4.6	3.5	2.3	2.1
Toroidal magnetic field, B_T (T)	2.25	2.28	2.28	1.72	1.62
Major radius, R_0 (m)	2.96	2.93	2.93	2.97	2.96
Minor radius, a (m)	1.18	1.14	1.14	1.11	1.12
Aspect ratio, A	2.5	2.6	2.6	2.7	2.6
Elongation, κ_x, κ_y	1.87, 1.72	1.81, 1.70	1.80, 1.72	1.90, 1.83	1.91, 1.84
Triangularity, δ_x, δ_y	0.50, 0.40	0.41, 0.33	0.41, 0.34	0.47, 0.42	0.45, 0.41
Safety factor, q_{95}	3.0	3.2	4.4	5.8	6.0
Shape Parameter ($=q_{95}I_p/(aB_T)$)	6.3	5.7	5.9	7.0	7.0
Plasma Volume (m ³)	131	122	122	124	124
Heating Power, P_{heat} (MW)	41	34	37	37	31
Temperature (Vol-ave.), $\langle T_i \rangle, \langle T_e \rangle$ (keV)	6.3, 6.3	3.7, 3.7	3.7, 3.7	3.4, 3.3	3.1, 2.9
Electron Density, Vol-ave, (E_{20}/m^3)	0.56	0.81	0.62	0.42	0.43
Stored Energy (Thermal, Fast ion) (MJ)	22.2, 4.0	18.0, 1.5	13.4, 2.1	8.4, 2.7	8.1, 1.7
Thermal Energy Confinement Time τ_E (s)	0.54	0.52	0.36	0.23	0.25
Current Diffusion Time (s)	32.7	15.2	14.6	12.6	10.8
Assumed Confinement improvement, HHy2	1.3	1.1	1.2	1.3	1.38
Normalized beta, β_N	3.1	2.8	3.0	4.3	4.3
Bootstrap current fraction, f_{BS}	0.28	0.3	0.4	0.68	0.79
Non inductive CD fraction, f_{CD}	0.5	0.43	0.58	1	1
Normalized density, n_e/n_{GW}	0.5	0.8	0.8	0.85	1.0

Figure 3.36 - JT-60SA operational scenarios parameters. [\[8\]](#)

The aim of the work is to optimize the scenarios and to check if the parameters are achievable. Only the first two scenarios are analyzed. The ramp-up, the flat-top and the ramp-down phase are included in the study. In order to make the simulation as realistic as possible two different codes are used. The first one, METIS, is able to predict the plasma equilibrium evolution from the post-breakdown phase to the ramp-down one, starting from a given LCFS. Scenario optimization is achievable launching a large number of simulations and varying a large number of parameters. After that, a second code, FEEQS, is used in order to compute coil currents, power supply voltages, forces on coils and to update the LCFS. Once the computation is finished, the new LCFS is uploaded (as result of FBE solution) in the same scenarios and METIS and FEEQS are run again in order to obtain a better convergence.

The starting point is changing the reference scenarios using the function “scenario generator” in METIS. The figure 3.37 shows the parameters that is possible to change.

The screenshot shows a software window titled "module interface jt60sametissimulation". It contains a grid of parameters, each with a label, a value field, and a data type. The parameters are organized into two main columns. The left column includes parameters like reference_parameters, gas, voltage_first, edge_density_factor, PNBI_N, PECCD, Recycling, runaway, and f_dipdt_rampup. The right column includes parameters like ip, flux, H_H, PNBI_P, PBREAK, radiation, breakdown, f_dipdt_rampdown, b0, density, ITB, PICRH, PRAMPUP, SOL_model, and duration. Each parameter has a corresponding value field (e.g., dropdown, text box, or spinner) and a data type label (e.g., (string), (integer), (float), (string)). At the bottom of the window, there are buttons for "Cancel", "reset", and "Ok".

Parameter	Value	Data Type
reference_parameters	/ZONE_TRAVAIL/	(string)
gas	2	(integer)
voltage_first	high	(string)
edge_density_factor	1	(float) [0.1 10]
PNBI_N	10	(float) [0 10]
PECCD	7	(float) [0 21]
Recycling	0	(float) [0 0.9999]
runaway	off	(string)
f_dipdt_rampup	1	(float) [0.3 3]
sepa_option	2	(integer)
ip	5.5	(float) [0.3 5.5]
flux	full	(string)
H_H	1.3	(float) [0.5 2]
PNBI_P	24	(float) [0 24]
PBREAK	0.1	(float) [0 2]
radiation	Matthews	(Matthews)
breakdown	off	(string)
f_dipdt_rampdown	1	(float) [0.3 3]
sepa_create	No	(string)
b0	2.25	(float) [0.3 2.3]
density	6.04	(float) [1 15]
ITB	off	(string)
PICRH	0	(float) [0 24]
PRAMPUP	5.7	(float) [0 7]
SOL_model	scaling	(string)
duration	100	(float) [30 100]

Figure 3.37 - Module interface JT60-SA scenario generator.

The meaning of the parameters are:

- Sepa_option allows selecting the reference scenario for LCFS parametrization;
- sepa_create allows using an LCFS provided by CREATE or generated by the program;
- Gas option selects the main gas species;
- Ip imposes the value of plasma current in the flat-top;
- b0 sets the vacuum magnetic field;
- voltage_first allows using high or low loop voltage;
- flux is able to shift from half CS current to full CS current of available flux from pre-magnetization;
- density imposes the value of the line average electron density during flat-top;
- edge_density_factor consists of a multiplication factor applied to the edge density scaling law;
- H_H imposes the confinement time multiplication factor during the H-mode phase;
- ITB allows or not the ITB formation;
- PNBI_N defines the maximum value of negative NBI power during flat-top;
- PNBI_P defines the maximum value of positive NBI power during flat-top;
- PICRH defines the maximum value of ICRH power during flat-top;

- PECCD defines the maximum value of ECCD power during flat-top;
- PBREAK defines the injected ECCD/ECRH power for assisted breakdown;
- PRAMPUP defines the injected ECCD/ECRH power for assisted Ramp-up;
- Recycling imposes the wall recycling coefficient;
- Radiation defines the line radiation model;
- SOL_model defines the scrape-off-layer model;
- Runaway allows or not runaway electrons in the discharge;
- Breakdown turns on or off the breakdown model for plasma initiation;

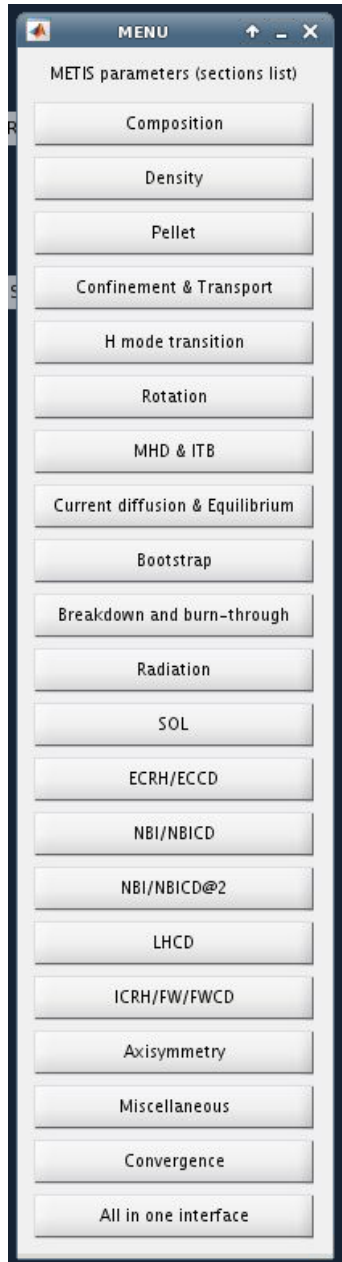


Figure 3.38 - METIS parameters sections list.

- Duration imposes the time of the end of flat-top;
- F_{dipdt_rampup} is the multiplication factor applied to dI_p/dt for plasma current ramp-up with respect to the reference case;
- $F_{dipdt_rampdown}$ is the multiplication factor applied to dI_p/dt for plasma current ramp-down with respect to the reference case.

Once the parameters have been changed, the reference scenario is updated. It is possible to modify the waveforms of the parameters using the main windows of METIS GUI and other parameters using the METIS parameters section list showing in the following figure 3.38:

- Composition allows tuning the plasma composition, the behavior of helium, impurities accumulation and presence or absence of tungsten.
- Density allows controlling the plasma electron density behavior and plasma electron density shape.
- Pellet allows switching on or off pellet injection, to prescribe the amount of fueling due to pellet and to tune the pellet deposition profile.
- Confinement & Transport allows tuning the model for core and pedestal confinement and to choose the shape of transport coefficients.
- H mode transition allows managing the transition from L-mode to H-mode and the back transition from H-mode to L-mode.
- Rotation allows turning the model for toroidal rotation and to select the mode for poloidal rotation.
- MHD & ITB section allows tuning the model for sawteeth, for ITB threshold and for MHD beta limit.
- Current diffusion & Equilibrium allows changing boundary condition for the current diffusion equation, choosing parameters for equilibrium and turning on or off the model for runaway electrons.
- Bootstrap allows selecting the model used to compute bootstrap current for core plasma, pedestal and fast ions.
- Breakdown and burn-through allows turning on or off the model describing breakdown and burn-through and turning physical quantities as prefill pressure, passive structure parameters, etc.
- Radiation allows selecting model for line radiation and tuning parameters for radiation sources.

- SOL allow selecting model for SOL and divertor and tuning physical associated parameters.
- ECRH/ECCD allows tuning EC/ECCD source.
- NBI/NBICD allows tuning first NBI/NBICD source.
- NBI/NBICD@2 allows tuning second NBI/NBICD source.
- LHCD allows tuning LHCD or second ECCD source.
- ICRH/FW/FWCD allows tuning IC source.
- Axisymmetry allows turning on or off the magnetic ripple effect computation.
- Miscellaneous allow changing machine name, shot number, choosing a file for first wall description, override all parameters with parameters given in a file and set reactor power balance parameters.
- Convergence allows changing METIS internal convergence parameters.

Once all the parameters have been selected, METIS is run and the output is generated. The aim of the study is to reach all the values of parameters reported in figure 3.36. Another fundamental aspect is to achieve a shot as long as possible within the available flux limit. An example is reported in the following figure 3.39.

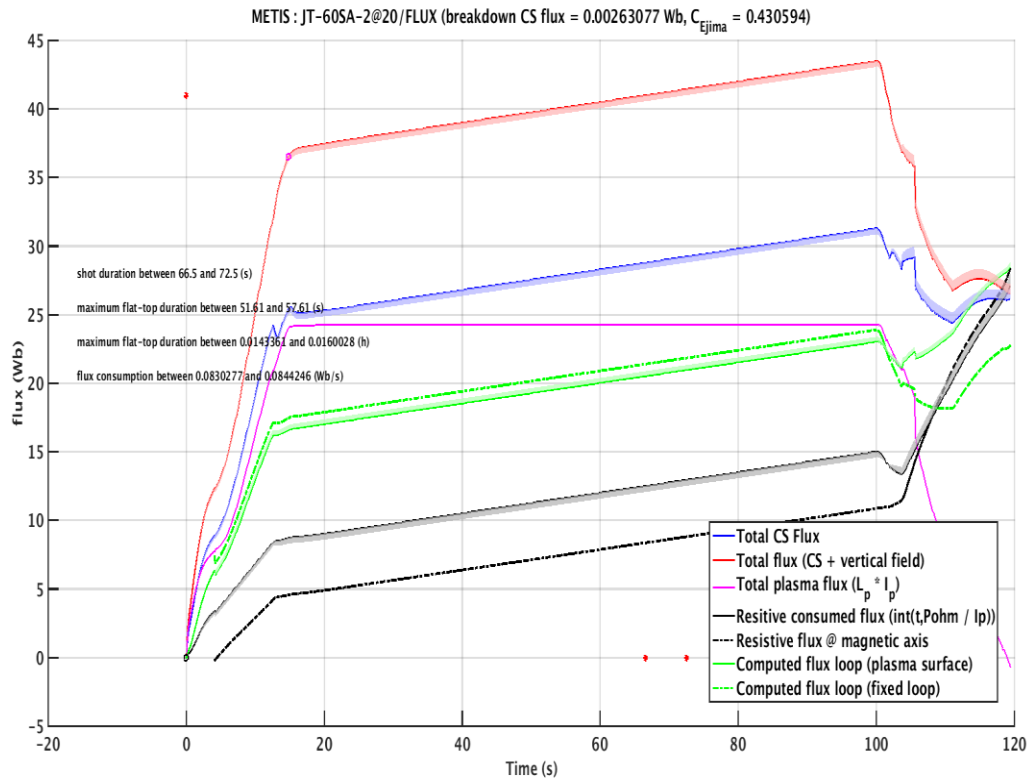


Figure 3.39 - Computed flux consumption for scenario 2 (not optimized). Red point near the vertical axis defines the available flux after breakdown, the two red points near the horizontal axis display the duration of the shot.

As it is possible to notice from figure 3.39, the red point near the vertical axis defines the available flux after breakdown, the two red points near the horizontal axis display the duration of the shot, which in this case is included between 66.5s and 72.5s

The figure 3.40 shows how the flux consumption behaves changing the plasma current, density and ECRH waveforms with respect to the previous not-optimized case.

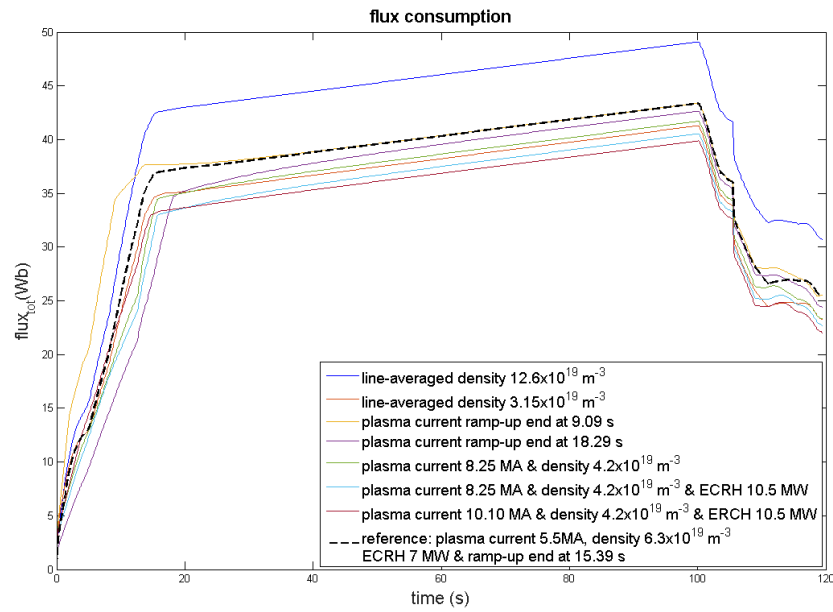


Figure 3.40 - The maximum value of the line-averaged electron density, the plasma current and the ECRH and the derivative of the current ramp-up are changed respect to scenario 2 of JT-60SA in order to understand how the flux consumption behave.

For example, the faster the plasma current ramp-up, the lower is the flux consumption. Of course, the higher is the power of ECRH and the lower is the flux consumption.

Another parameter that has been checked is the loop voltage. It has to be included between the upper and lower limit as long as possible, however it can overcome the limits but for a very short time. The loop voltage for the reference case is reported in the figure 3.41.

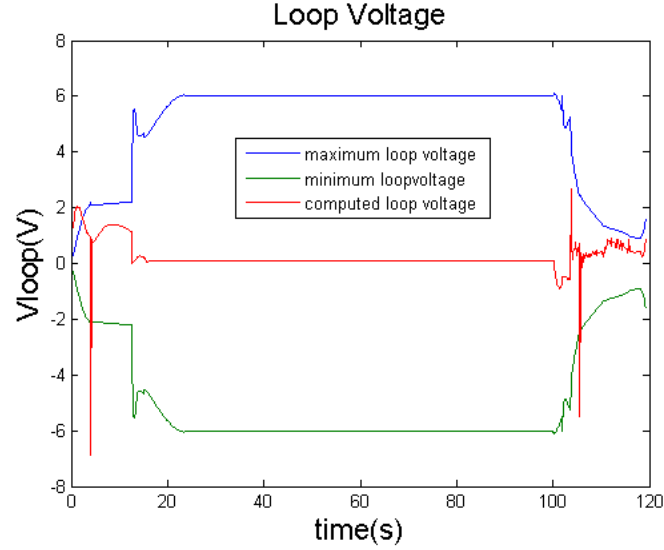


Figure 3.41 - Loop Voltage for reference case. First peak is related to the reach of H-mode, second peak is due to the loss of the x-point.

The first negative peak corresponds to the transition from L-mode to H-mode, the second one is related to the losses of the x-point. Both are difficult to eliminate, however it is possible to reduce them significantly.

Also the line-averaged electron density has to be checked because it has to be higher respect to a low limit due to the instability and lower than the Greenwald limit. The first limit is imposed in order to minimize the runaway electron formation. The second one is computed as $\frac{I_p}{\pi a^2}$ and in tokamaks exceeding it leads to a disruption. The figure 3.42 shows the behavior of the three densities for the reference case.

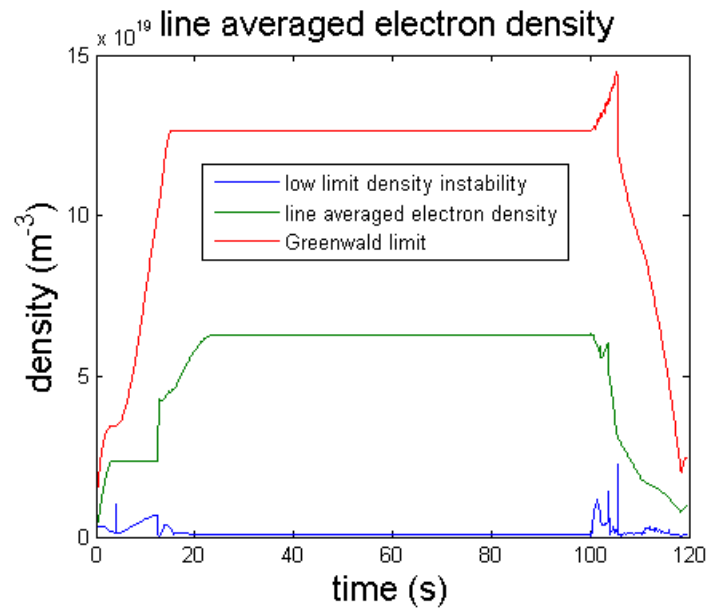


Figure 3.42 – Line-averaged electron density, Greenwald density and low limit for reference case.

Finally, it is important to check if the plasma is subject to disruptions during the shot because if they are present they have to be eliminated in order to have safe plasma operation and prevent structures damage. Control of disruptions should be taken into account for safety in ITER, in which only a limited number of disruptions will be tolerable and because any disruptions are unacceptable for DEMO. Therefore their prediction and avoidance in high beta operation are an important subject. Disruptions are caused by vertical displacement events (VDE), MHD mode locking during current plasma ramp-up, high density above the Greenwald density limit, machine or sub-system dysfunctions and others adverse events. Against the disruptions, JT-60SA has a passive stabilizing plate and fast plasma position control coils (FPPC) inside the vacuum vessel. Also massive gas injection and ECRF are useful tools for their control and mitigation. Figure 3.43 reports possible disruption during the shot for the reference case. To describe the disruption, METIS uses the influence of runaway electrons on current diffusion during the current ramp-up. Figure 3.44 shows the electron volume averaged temperature and the electron central temperature. The dashed lines in figure 3.44 represent the values that the temperature has to reach in order to respect the operation scenarios parameters values reported in figure 3.36.

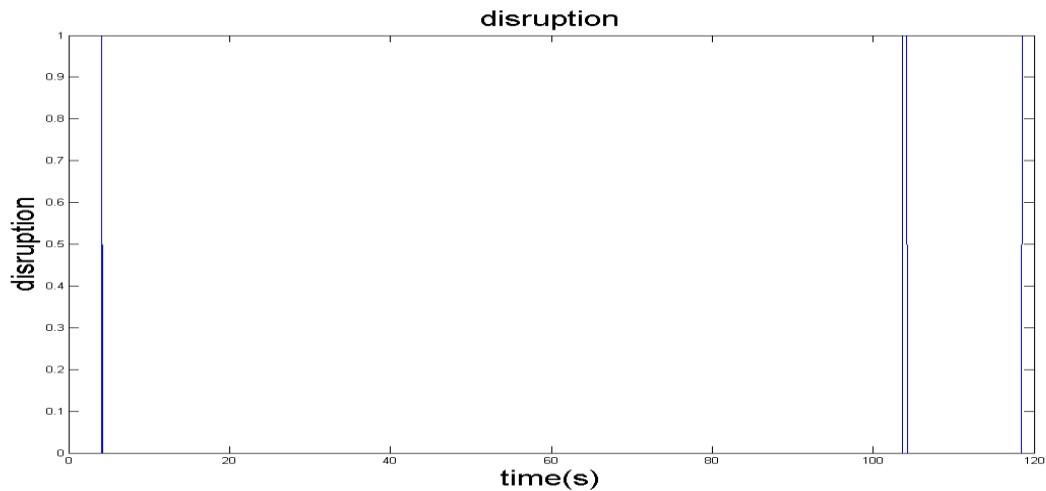


Figure 3.43 - Disruption during the shot for the reference case. Value 1 means that a disruption has occurred.

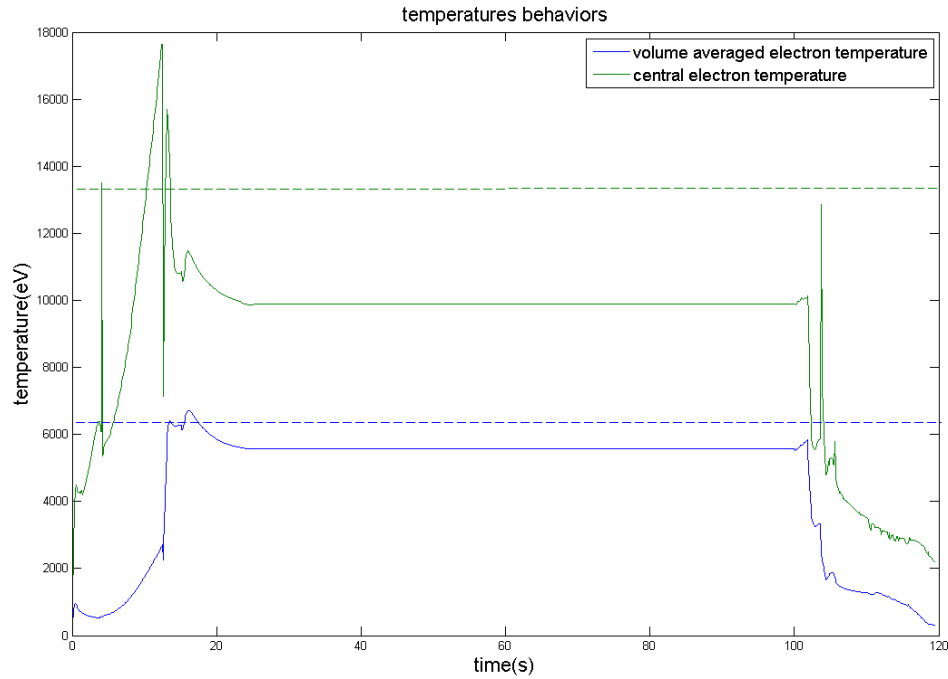


Figure 3.44 - Volume averaged electron temperature behavior and central electron temperature compared with the values reported in figure 3.39 (dashed lines).

At this point, FEEQS has been run in order to check if coils currents and forces on coils are inside the limits. The flux offset is set to 8 Wb in order to have the starting values of the coils currents lower the upper limits. The following figures show the currents and forces waveforms for each CS and PF coils. More precisely, figure 3.45 shows the coils currents behaviors, figure 3.46 represents the radial hoop forces on coils, figure 3.47 plots the vertical forces on coils and figure 3.48 displays the voltage on coils. As it is possible to notice, for this initial setting no waveforms respect the limits imposed.

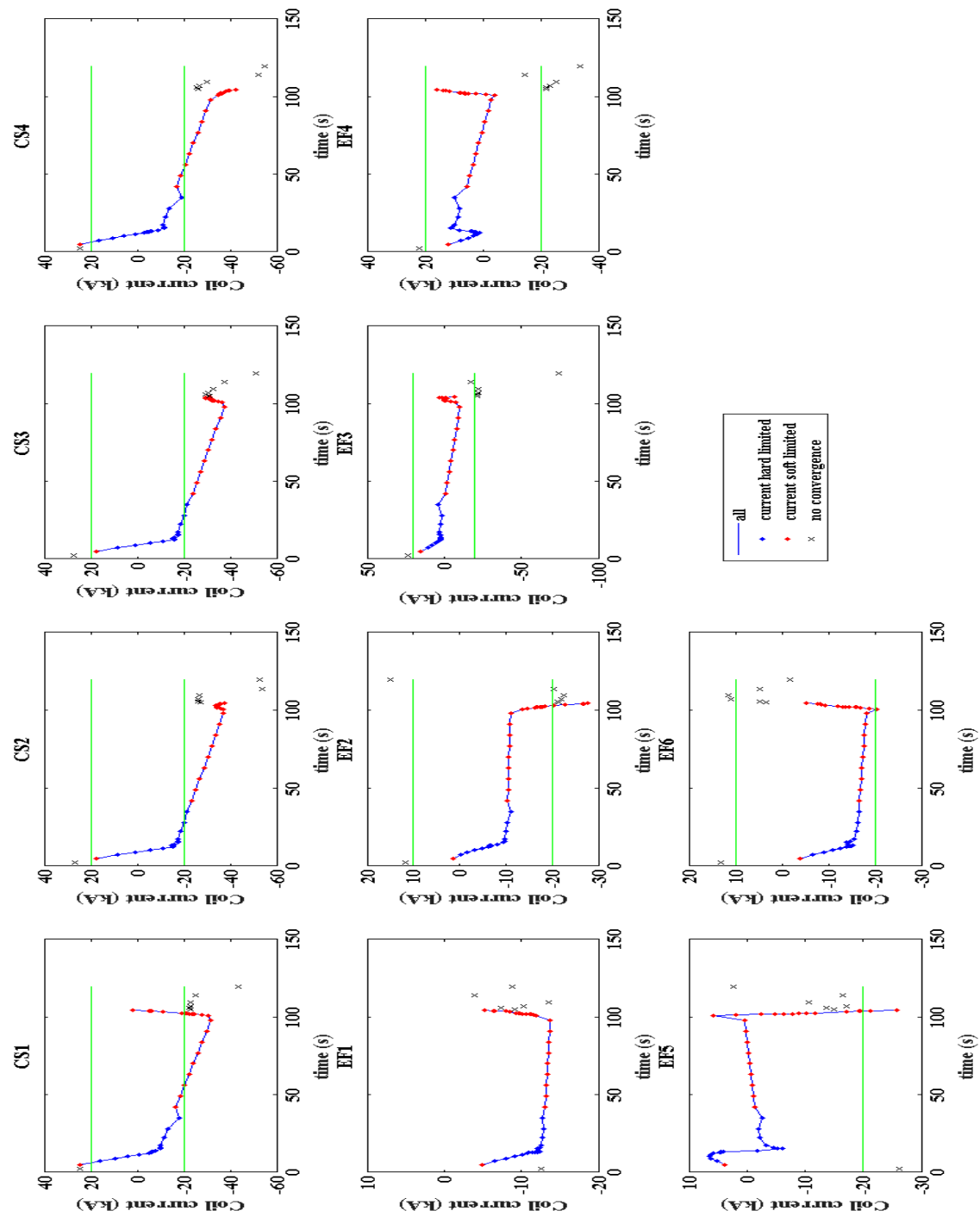


Figure 3.45 - Coils currents computed by FEEQS using the reference case as input data. Green lines represent the upper and the lower limits on each coils. All the computed coils current have to respect the imposed limit after the optimization process.

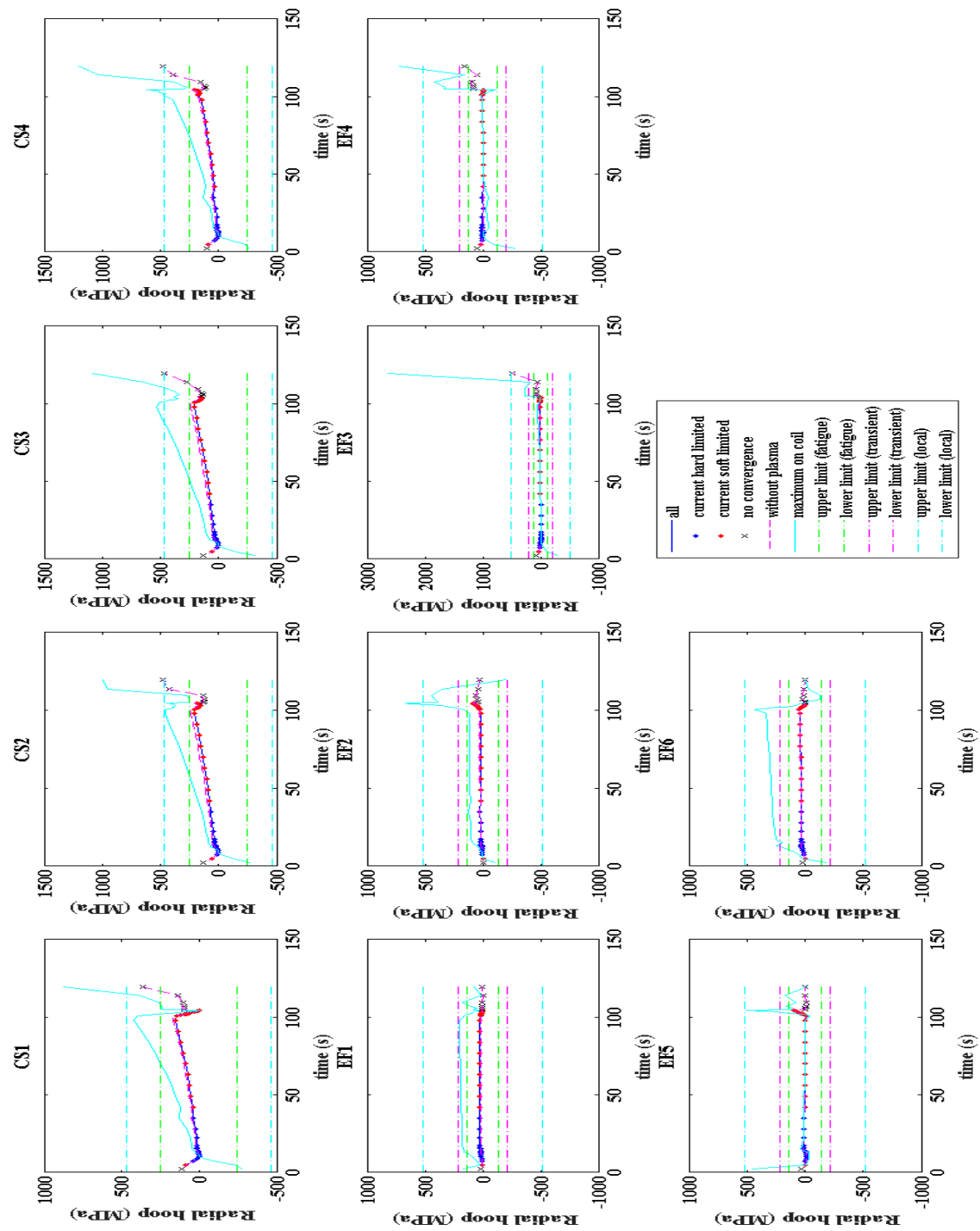


Figure 3.46 - Radial hoop forces computed by FEEQS using the reference case as input data. Green lines represent the upper and the lower limits on each coils. All the computed hoop forces have to respect the imposed limit after the optimization process.

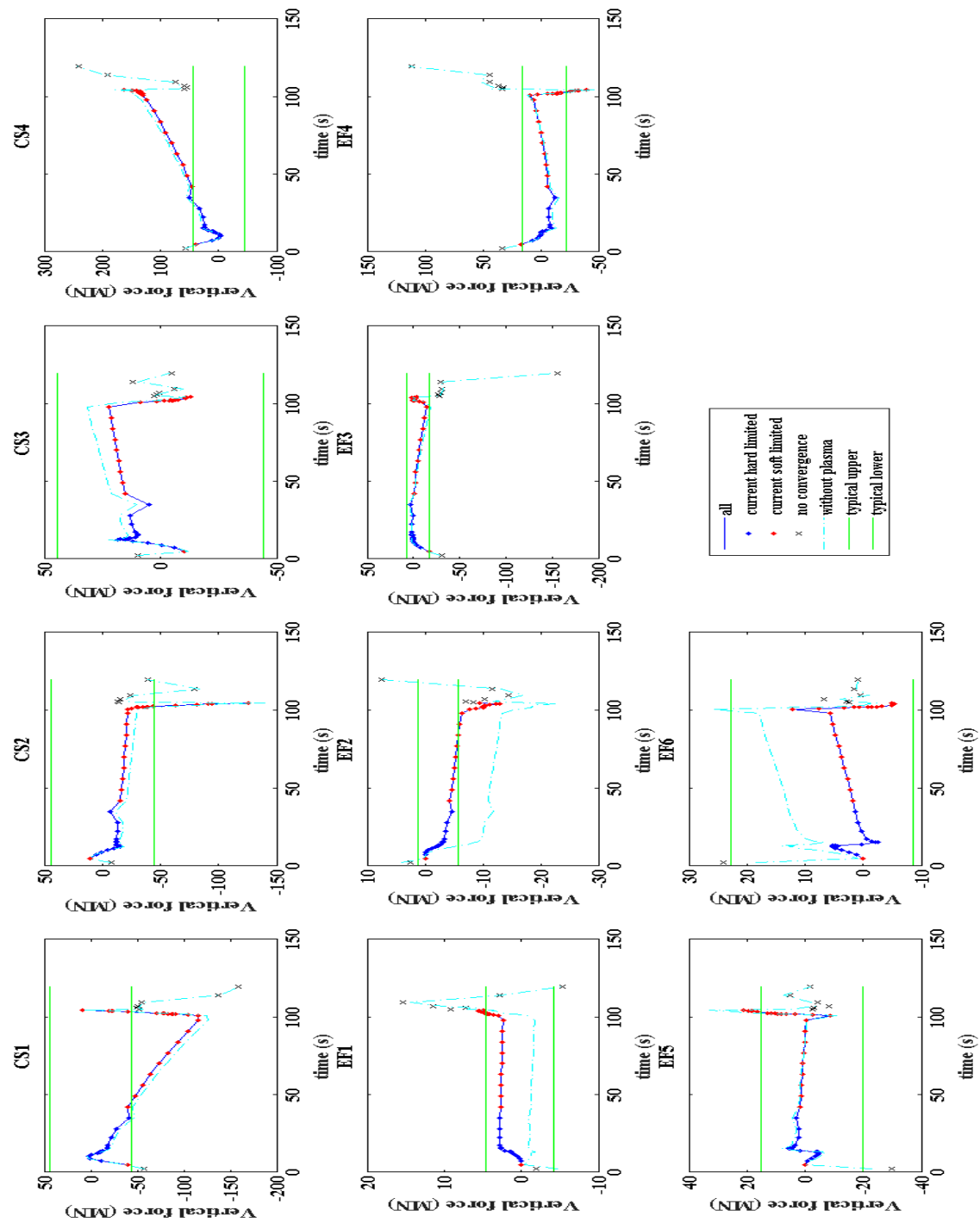


Figure 3.47 - Vertical forces computed by FEEQS using the reference case as input data. Green lines represent the upper and the lower typical values on each coils. All the computed vertical forces have to respect the imposed limit after the optimization process.

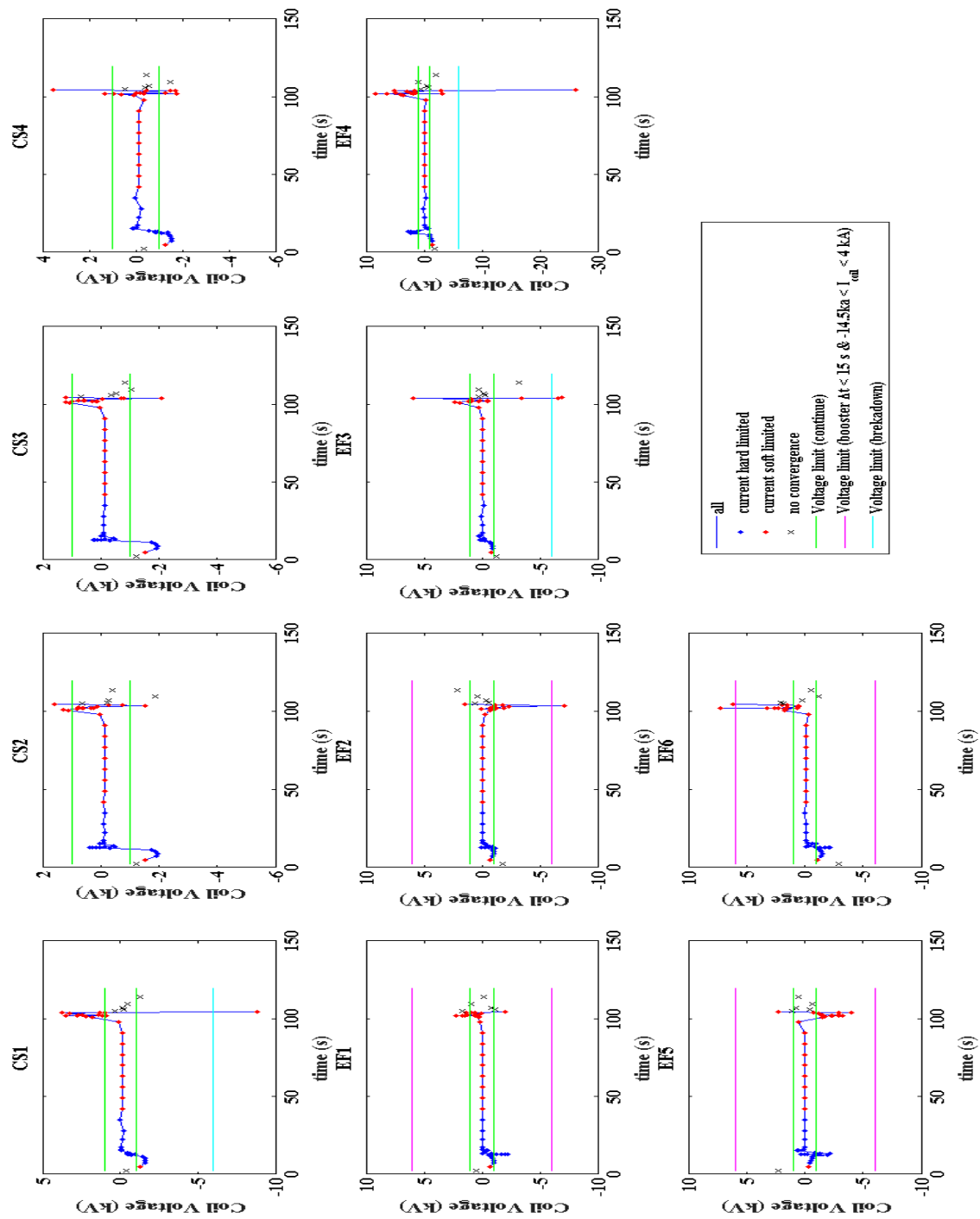


Figure 3.48 - Coils voltage computed by FEEQS using the reference case as input data. Green lines represent the upper and the lower limits on each coils. All the computed coils voltage have to respect the imposed limit after the optimization process.

3.3.1 Scenario #2

The first scenario analyzed is a standard H-mode similar to the ITER baseline scenario. It consists of an inductive operation at $I_p=5.5$ MA with a flat top duration of 100 s. The heating and current drive systems will provide neutral beam injection of 34MW (10MW, 500KeV N-NBI and 24MW, 85KeV P-NBI) and ECRH of 7MW with 138GHz frequency (the appropriate one for a 2.25 T magnetic field). The divertor target is designed to be water-cooled in order to handle the expected heat flux up to 15MW/m² for up to 100s [\[17\]](#). The other main parameters of scenario #2 are reported in the table 3.6.

Table 3.6 - Typical parameters of scenario #2.

Plasma current I_p (MA)	5.5
Toroidal magnetic field B_T (T)	2.25
Major radius R (m)	2.96
Minor radius a (m)	1.18
Flattop duration (s)	100
N-NBI power (MW)	10
P-NBI power (MW)	24
ECRH power (MW)	7
Volumetric averaged electron temperature (KeV)	6.3
Central averaged temperature (KeV)	13.5
Volumetric averaged electron density (10E20/m³)	0.56
Line-averaged electron density (10E20/m³)	0.63
Central averaged electron density (10E20/m³)	0.77
H factor	1.3

In order to simulate this scenario, deuterium is used, the plasma current has to be of 5.5MA, the vacuum magnetic field is imposed to 2.25T as reported in table 3.6, the duration is set to 100s and full CS current is considered. In addition, the value of H_H factor (1.3), PNBI_N (10MW), PNBI_P (24MW) and PECCD (7MW) are chosen following the table 3.6. The breakdown is taken into account, while ITB formation, recycling and runaway effects are neglected. Matthews scaling law is considered to model the line radiative power in the core plasma and the LFCS electron temperature and density are computed using scaling law models. All of the simulations have been made setting a low voltage in order to reduce the values of the two voltage peaks and setting the line-averaged density to $6.3 \times 10^{19} \text{ m}^{-3}$ that is the value reported in the table 3.6 [\[29\]](#)

Some simulation is done in order to decide the value of power for assisted breakdown (PBREAK) and the maximum power at the end of the ramp-up (PRAMPUP). The first parameters is set to 0.1 because

a higher value leads to a very large electron temperature at the beginning of the shot. The second one is set to 6.7 because this corresponds to the value that largely increase the flat-top duration.

In order to choose the value of the ramp-up rate (f_{dipdt_rampup}) three different simulations are generated: in the first one this value is set to 0.7 MA/s, in the second one is set to 1 MA/s and in the last one is set to 1.9 MA/s. The ramp-down rate ($f_{dipdt_rampdown}$) is set to 1.3 MA/s for the first and the last case because this corresponds to the value that minimizes the voltage peak due to the L-mode transition. In the second simulation, it is set to 1 MA/s in order to have the same value in the two peaks.

The value of multiplication factor applied to edge density scaling law ($edge_density_factor$) is different for the three cases: 1.58 for the first shot, 2.5 for the second one, and 2.7 for the last one.

The ECRH radial deposition position is equal to 0.25 for the first two cases, while it is equal to 0.5 up to 40s and it is shifted to 0.6 for the last case. This leads to obtain the values of volume averaged and central electron density of table 3.6.

The ECRH power waveform is modelled in order to avoid the first disruption of the plasma due to the x-point formation, while P-NBI is used to assist the transition to H-mode. This transition is reached at 17.793s in the first case, at 12.49s in the second case and at 6.5s in the third case.

All of the geometrical parameters of the plasma shape are kept constant in the different cases.

The central and the volume averaged electron temperature show a high value at the very beginning of the shot and this is due to the breakdown, in fact after 0.06s they start to decrease and reach acceptable values. This stresses the need for detailed modelling to have results that are more precise.

For all of the simulations a duration of 100s is ensured, so FEEQS is used in order to compute the coil currents and determine which is the best simulation. The following figures (from 3.49 to 3.53) show the coils currents behaviors for each coil.

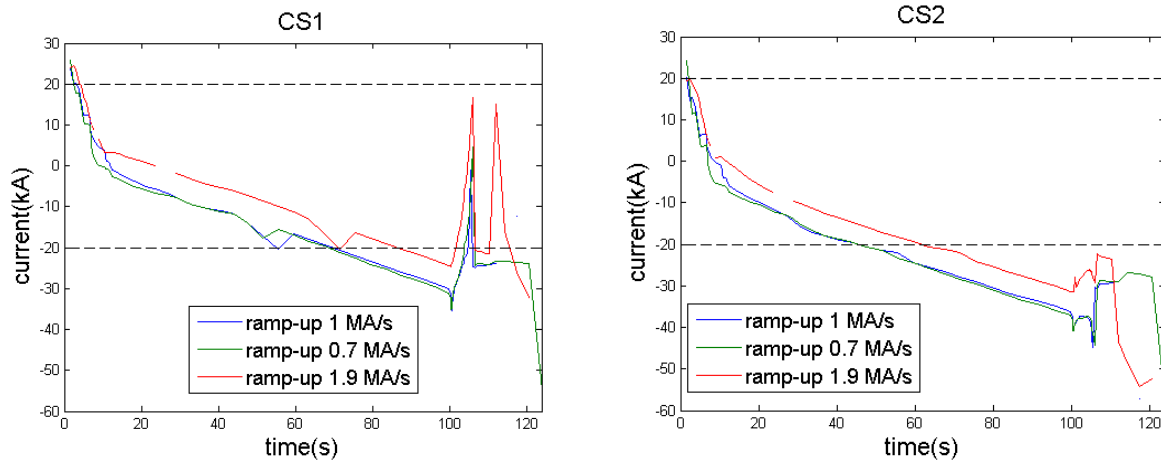


Figure 3.49 – Left: CS1 currents behaviors. Right: CS2 currents behaviors.

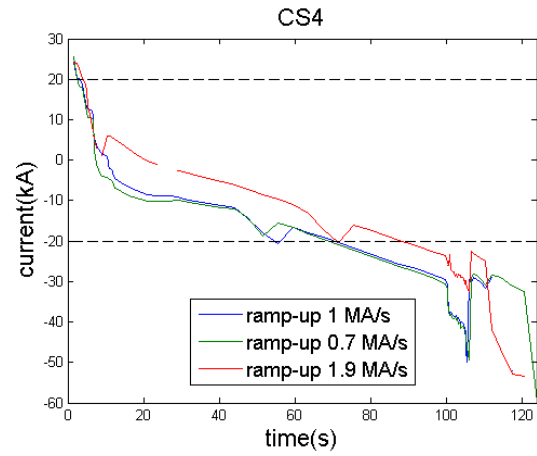
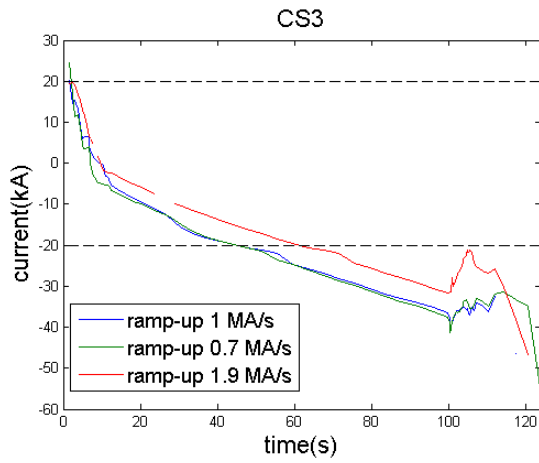


Figure 3.50 – Left: CS3 currents behaviors. Right: CS4 currents behaviors.

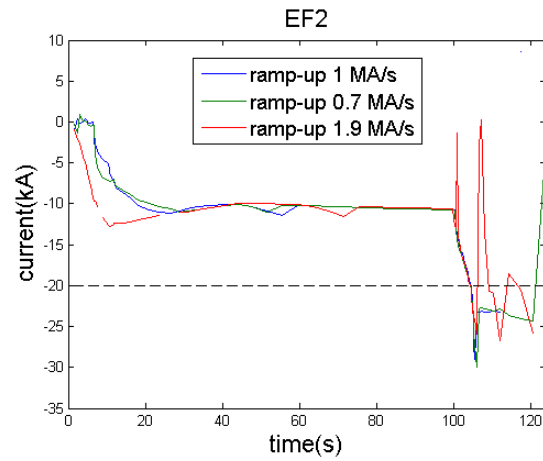
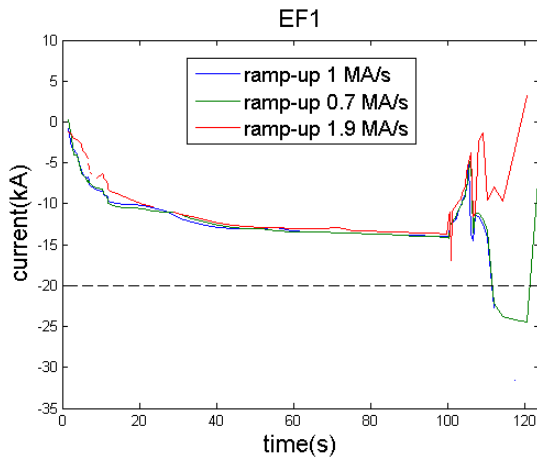


Figure 3.51 - Left: EF1 currents behaviors. Right: EF2 currents behaviors.

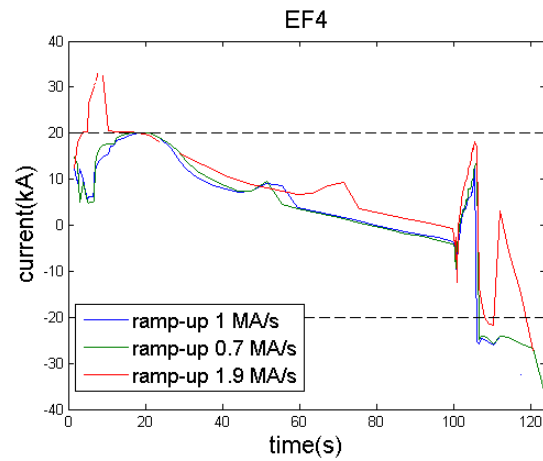
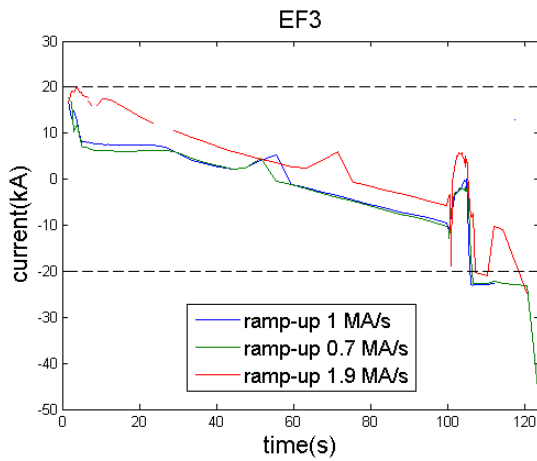


Figure 3.52 - Left: EF3 currents behaviors. Right: EF4 currents behaviors.

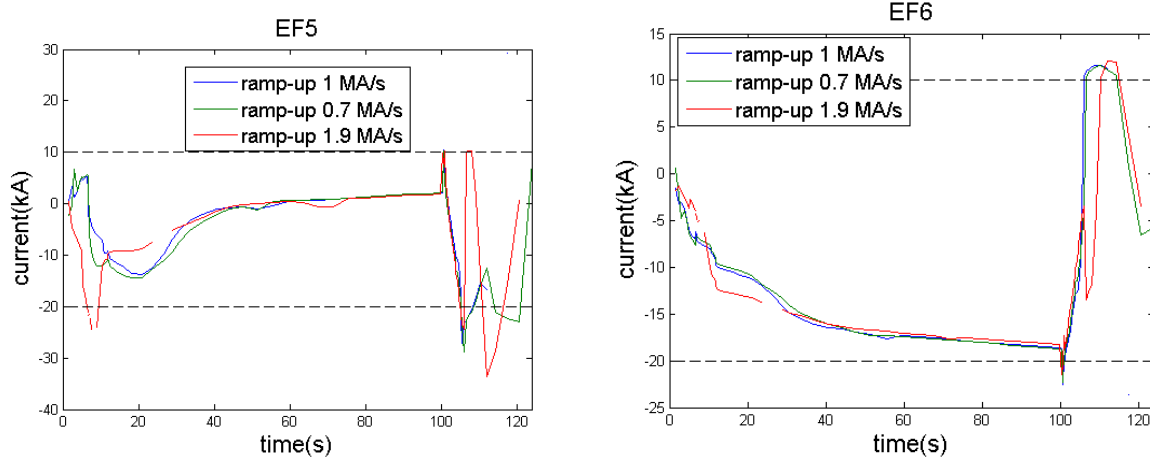


Figure 3.53 - Left: EF5 currents behaviors. Right: EF6 currents behaviors.

As it is possible to notice, especially from the CS coils currents behaviors, an increase of ramp-up rate leads to a reduction of flux consumption during the ramp-up. Probably, this phenomenon is due to the reaching of H-mode transition before the other two cases. The gaps in the curves are due to a non-convergence between FEEQS and METIS. The large fluctuations during the ramp-down are caused by different configurations of LCFS between the codes. In fact, in METIS the LCFS is given by points, which means that it is not a solution of free boundary equilibrium problem. In FEEQS the LCFS is obtained solving the FBE, therefore it is really a true solution. For this reason, the LCFS computed by FEEQS has to be uploaded in METIS and the code has to be run again. This last step is made only in the third case, which is chosen to continue the optimization process.

Starting from the configuration in which the ramp-up is set to 1.9 MAs, some METIS parameters are changed. In particular, the density peaking factor (central density/volume averaged density) has a fixed value of 1.3, the ECRH deposition poloidal location is set to 180 and the vertical shift at the center of the plasma of the neutral beam trajectory is set to 0.5.

At this point, the waveforms of other parameters have been changed in order to reduce the flux consumption and therefore the CS coil currents. More precisely, the ECRH deposition width is set to 0.7 and it is still Gaussian. Tangency radius of NBIs are imposed to 2.5, the current drive efficiency multiplication factor of N-NBI and of ECRH are set to 1.3 and the temporal evolution of NBICD has the same behavior of thermal P-NBI.

In order to better understand the following figures, table 3.7 reports the main times of the discharge.

Table 3.7 – Main times of simulation.

	Time (s)
X-point	2.32
End of ramp-up	6.92
ECRH switch-on	1.226
N-NBI and P-NBI switch-on	6.52/8.42
H-mode transition	6.52
End of flat-top/L-mode transition	100
End of ramp-down	124

Two final solutions have been chosen. In the first case the P-NBI and N-NBI are switched off respectively at 107.8 s and 110.6 s, in order to avoid plasma disruption. However, from 103 s the plasma starts to go down toward the divertor plates and NBIs power is no longer deposited into the plasma and therefore it heats the first wall. In the second case, NBIs are turned off at 100s and this leads to a plasma disruption. The figures (from 3.54 to 3.57) show the final waveforms of input parameters for both cases.

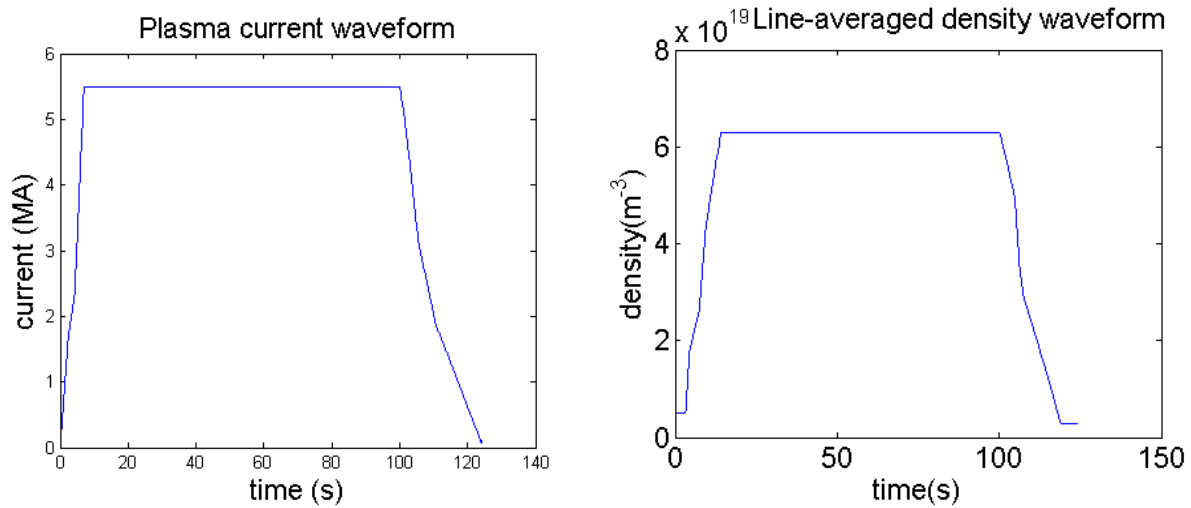


Figure 3.54 – Left: plasma current waveform input. Right: line-averaged electron density waveform input.

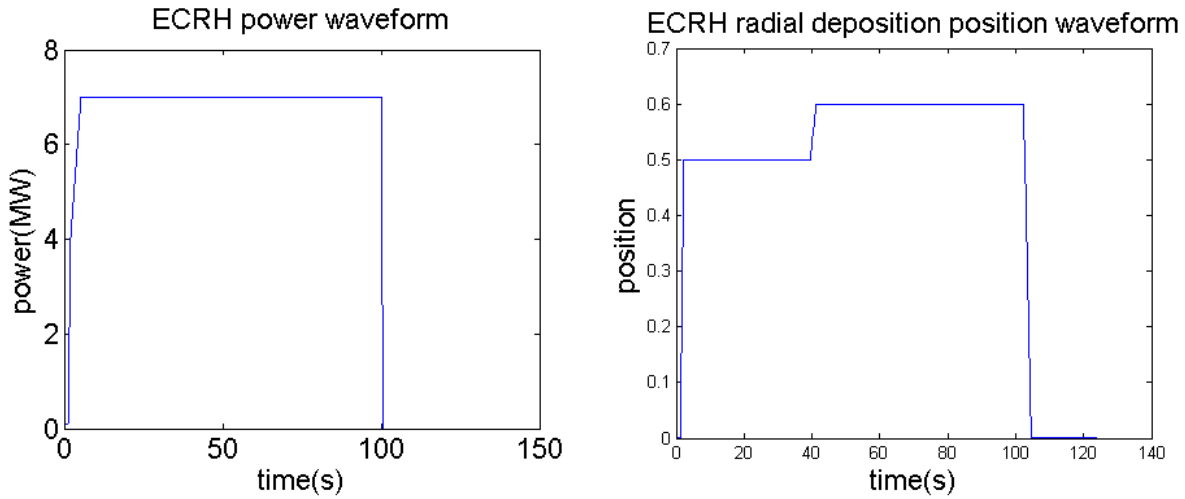


Figure 3.55 - Left: ECRH power deposition position waveform input. Right: ECRH power waveform input.

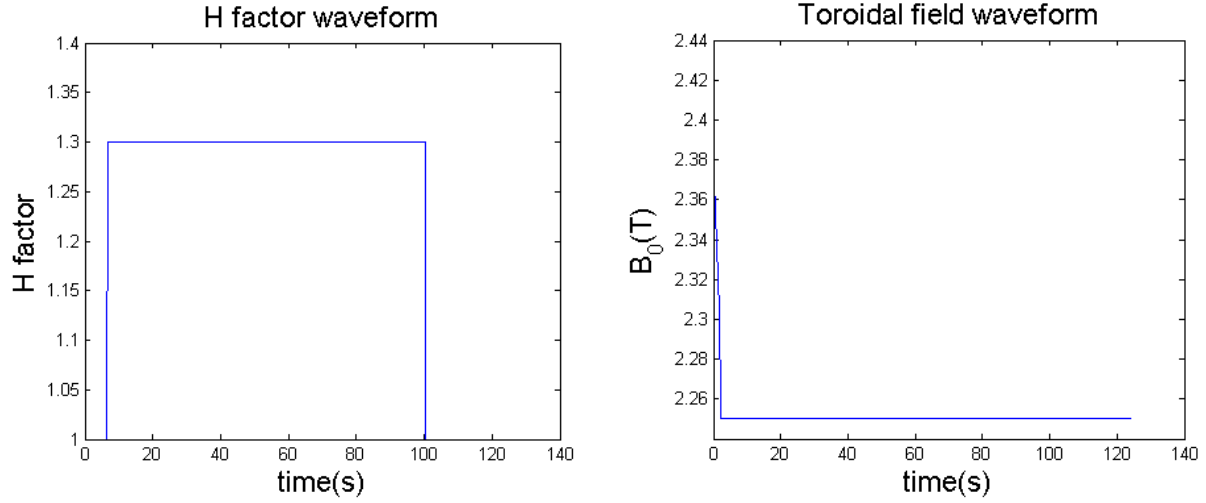


Figure 3.56 - Left: H factor waveform input. Right: toroidal field waveform input.

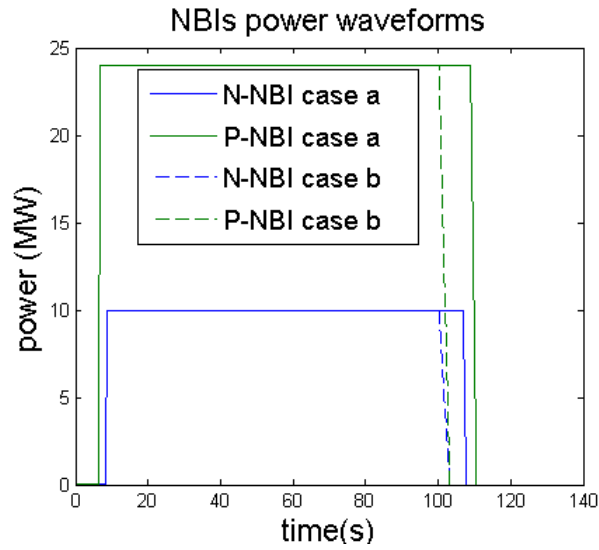


Figure 3.57 - NBIs waveforms inputs for both case. In first case, NBIs are switched off later in order to avoid the disruption; in the second case, NBIs are switched off at 103.2 s in order to avoid possible damage to the first wall.

In both cases the coil currents are computed using FEEQS, then the new LCFs are uploaded in METIS and both codes are run again. In all the run, the flux offset is fixed in manual mode with value 11 Wb and minimum and maximum regulation weights are 10^{-8} and 10^{-15} respectively. At the beginning of the run, FEEQS searches for a suitable time slice as starting point for computing the initial convergence loop and the best regularization weight. The last configuration of coil currents are plotted in the following figures (from 3.58 to 3.62) in order to stress the differences between the two cases.

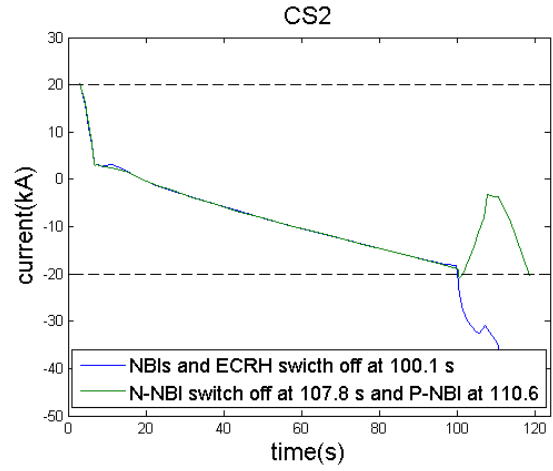
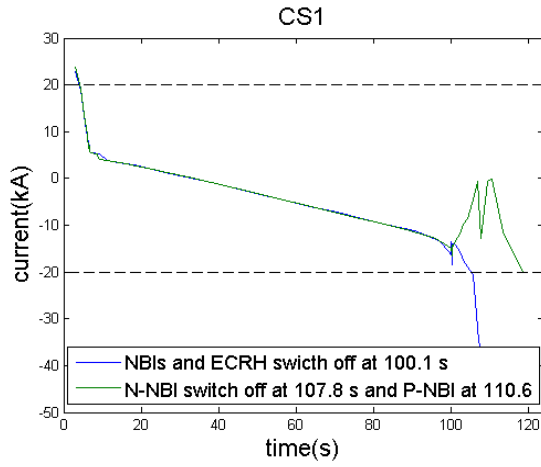


Figure 3.58 - Left: CS1 currents comparison. Right: CS2 currents comparison.

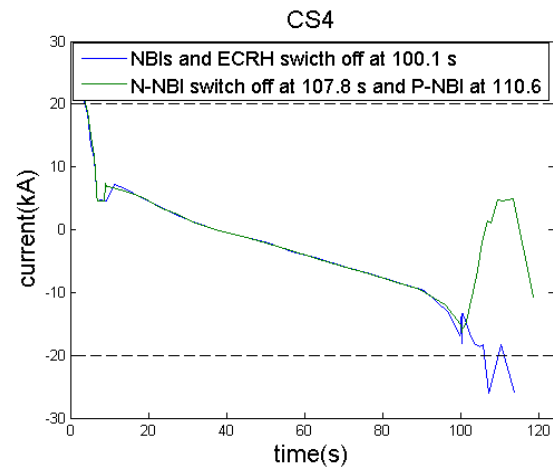
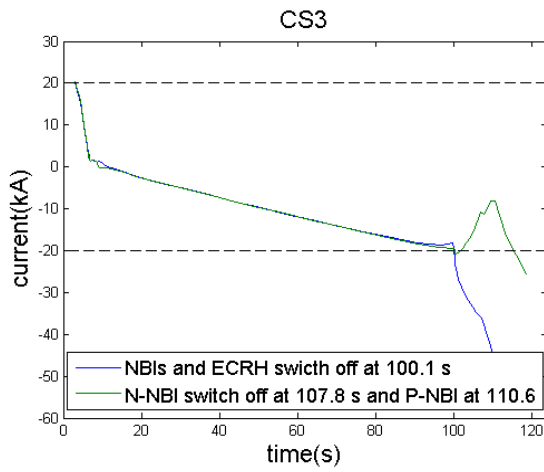


Figure 3.59 - Left: CS3 currents comparison. Right: CS4 currents comparison.

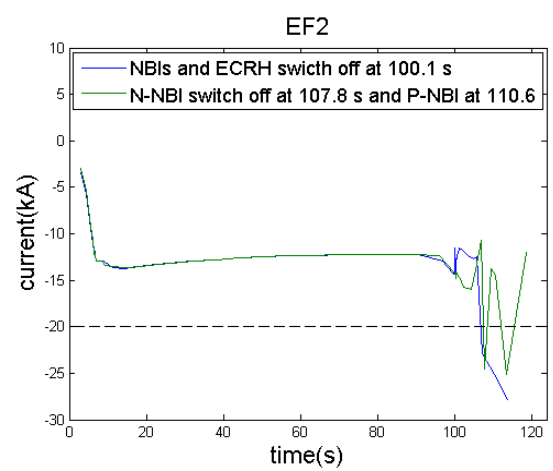
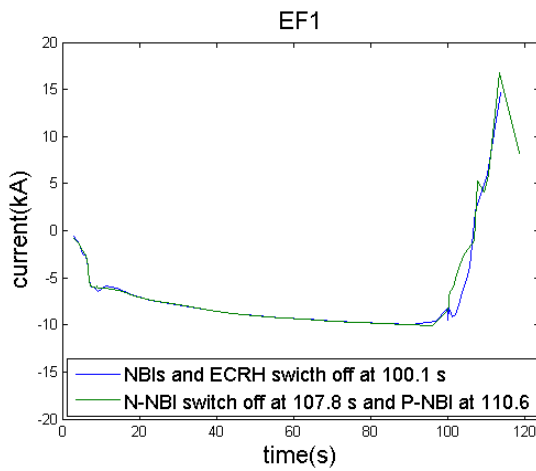


Figure 3.60 - Left: EF1 currents comparison. Right: EF2 currents comparison.

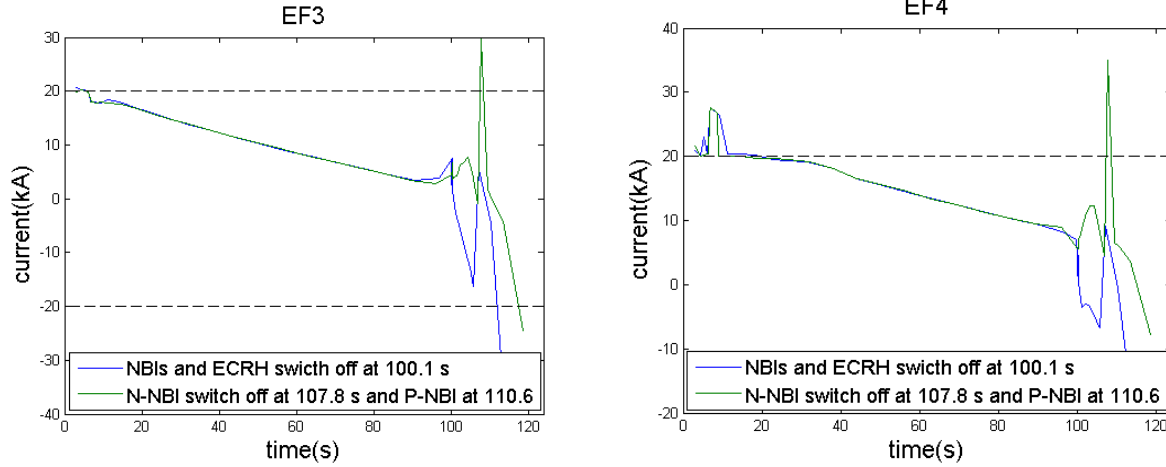


Figure 3.61 - Left: EF3 currents comparison. Right: EF4 currents comparison.

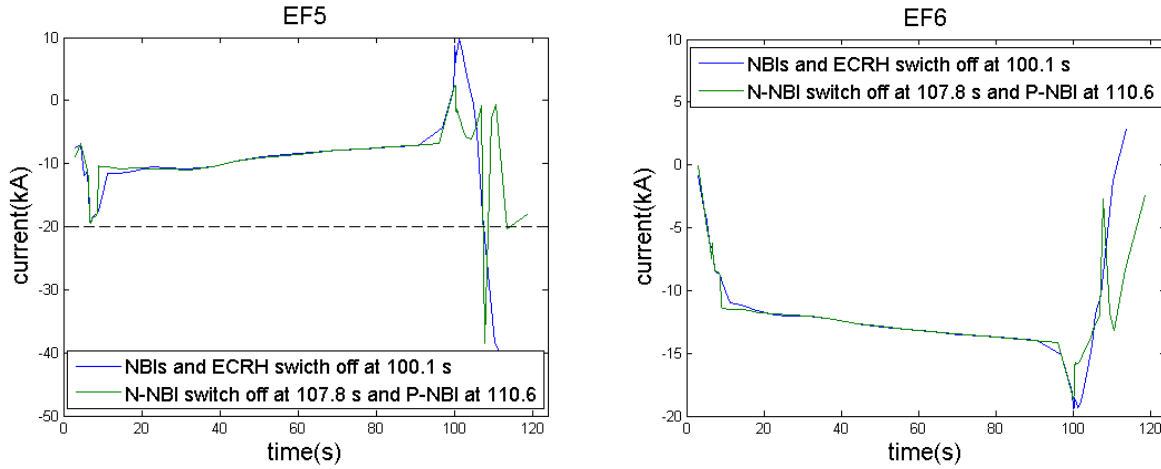


Figure 3.62 - Left: EF5 currents comparison. Right: EF6 currents comparison.

The case in which the P-NBI and the N-NBI are switched off at 107.8 s and 110.6 s shows a better behavior of coil currents during the ramp-down for the CS, but NBIs heats the first wall once the plasma starts to move downwards. Moreover, some peaks of currents appear in EF coils once the NBIs are switched off.

On the other hand, the case in which the external heating are switched off at 100.1 s shows a disruption during the ramp-down phase. Nevertheless the CS coil currents exceed the lower limits during the ramp-down.

In both cases, the EF4 and EF5 coils have a current jump, probably due to the transition from L-mode to H-mode as the geometric parameters do not show anomalies in this point. In order to solve the problem the current ramp-up is set to 1.3 MA/s, therefore the H-mode transition is shifted to 9.63 s. The ECRH deposition width is set to 0.2 and the current drive efficiency of N-NBI and of ECRH are set to 1. Again, two final solutions have been chosen. In the first case, the NBIs and ECRH are switched off at 102.8 s, in order to try to reduce the voltage peak occurring at the beginning of the ramp-down. In the second case, NBIs are turned off at 100s and this leads to a plasma disruption. The following figures (from 3.63 to 3.66) show the final waveforms of input parameters of both cases.

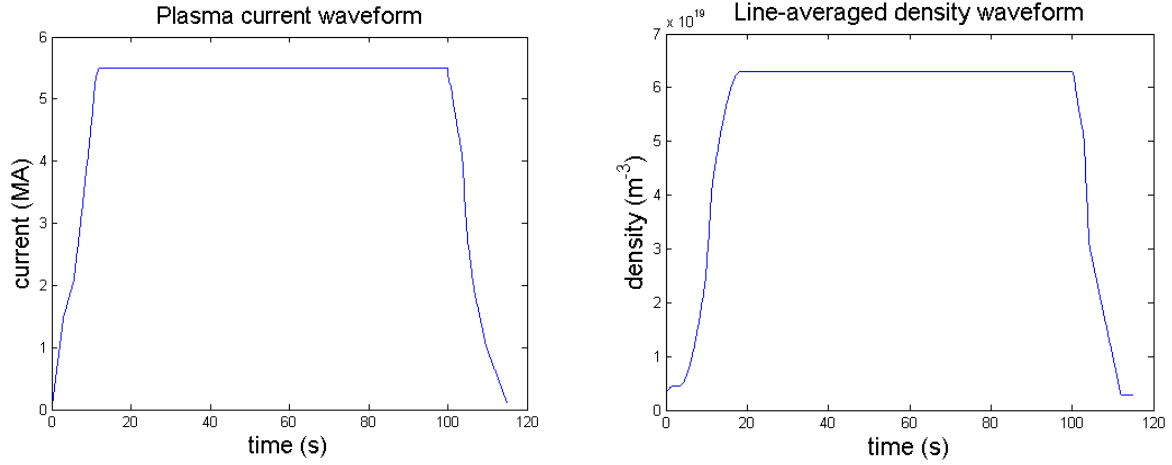


Figure 3.63 – Left: plasma current waveform input. Right: line-averaged electron density waveform input.

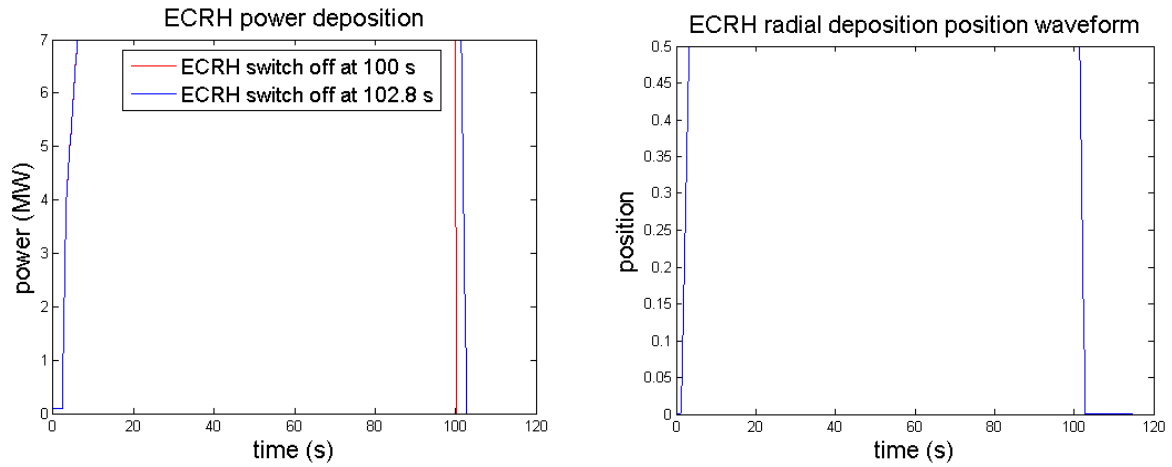


Figure 3.64 - Left: ECRH power deposition position waveform input. Right: ECRH power waveform input.

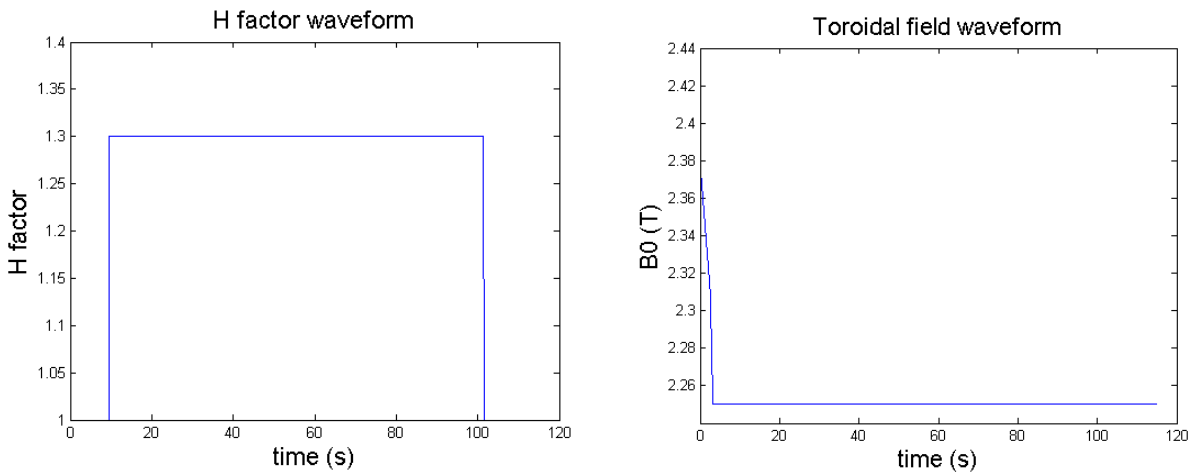


Figure 3.65 - Left: H factor waveform input. Right: toroidal field waveform input.

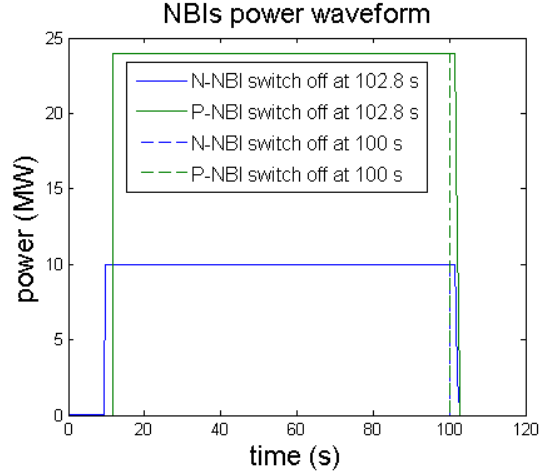


Figure 3.66 - NBIs waveforms inputs for both case. In first case, NBIs are switched off later in order to avoid the disruption; in the second case, NBIs are switched off at 100 s in order to avoid possible damage to the first wall.

In order to better understand the following figures, table 3.8 reports the main times of the discharge.

Table 3.8 – Main times of simulation.

	Time (s)
X-point	3.227
End of ramp-up	11.627
ECRH switch-on	1.226
N-NBI and P-NBI switch-on	9.63/11.73
H-mode transition	9.63
End of flattop/L-mode transition	100
End of ramp-down	114

As it is possible to predict from figures 3.53 and 3.54, CS2 and CS3 current coils could exceeded the value of lower limits of the current. For this reason, a third simulation is made using an ECRH and N-NBI efficiency of 1.3 in order to reduce the flux consumption. The NBIs and ERCH injections are switched off at 100s, as the first case, while all the other parameters are still the same.

In all cases the coil currents are computed using FEEQS, then the new LCFSs are uploaded in METIS and codes are run again. In all the runs, the flux offset is fixed in manual mode with value 10 Wb and the regulation weight is 10^{-15} . The last configuration of coil currents are plotted in the following figures (from 3.67 to 3.71) in order to stress the differences between the three cases.

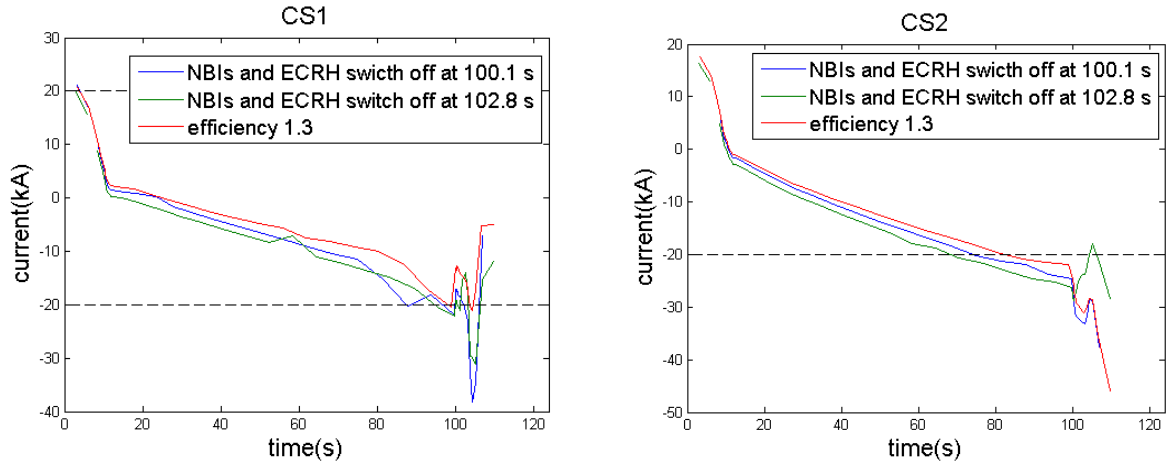


Figure 3.67 - Left: CS1 currents comparison. Right: CS2 currents comparison.

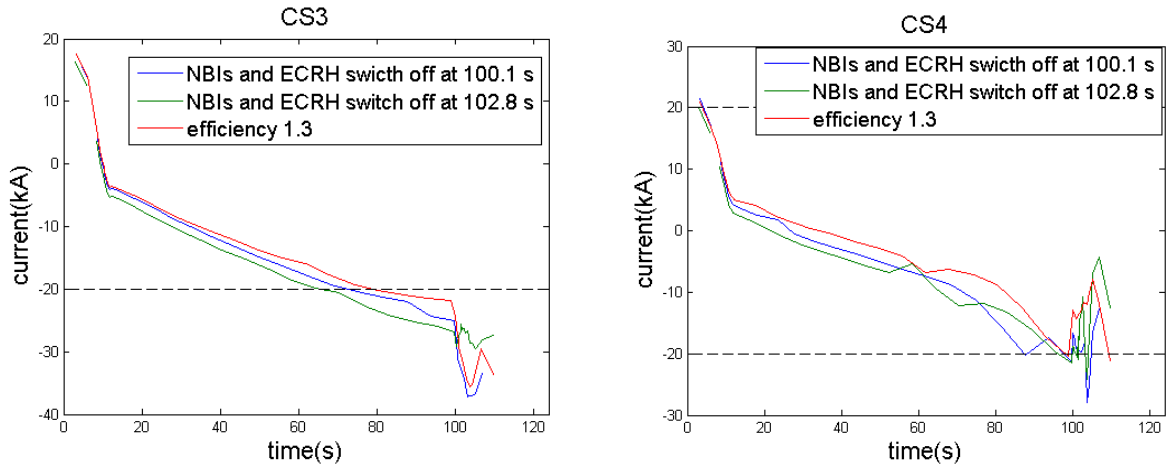


Figure 3.68 - Left: CS3 currents comparison. Right: CS4 currents comparison.

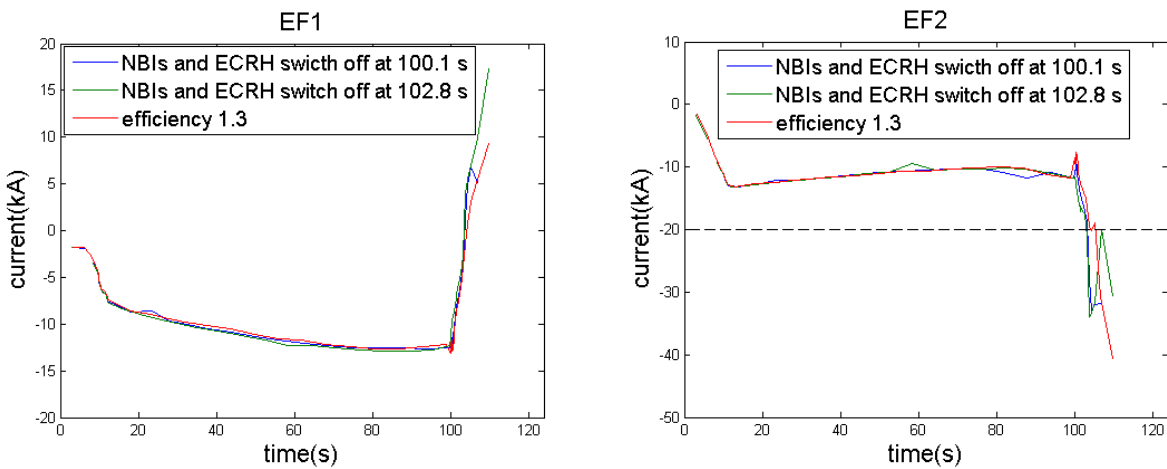


Figure 3.69 - Left: EF1 currents comparison. Right: EF2 currents comparison.

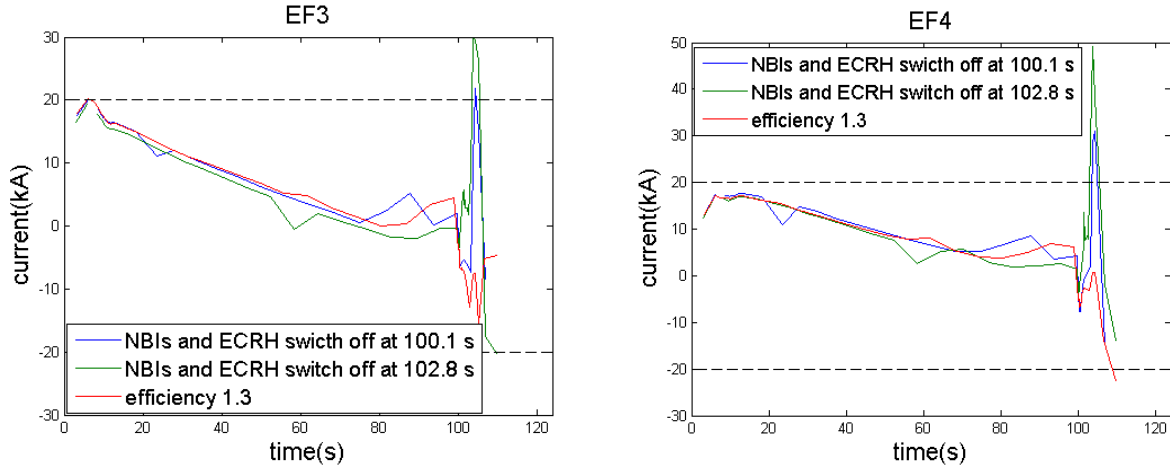


Figure 3.70 - Left: EF3 currents comparison. Right: EF4 currents comparison.

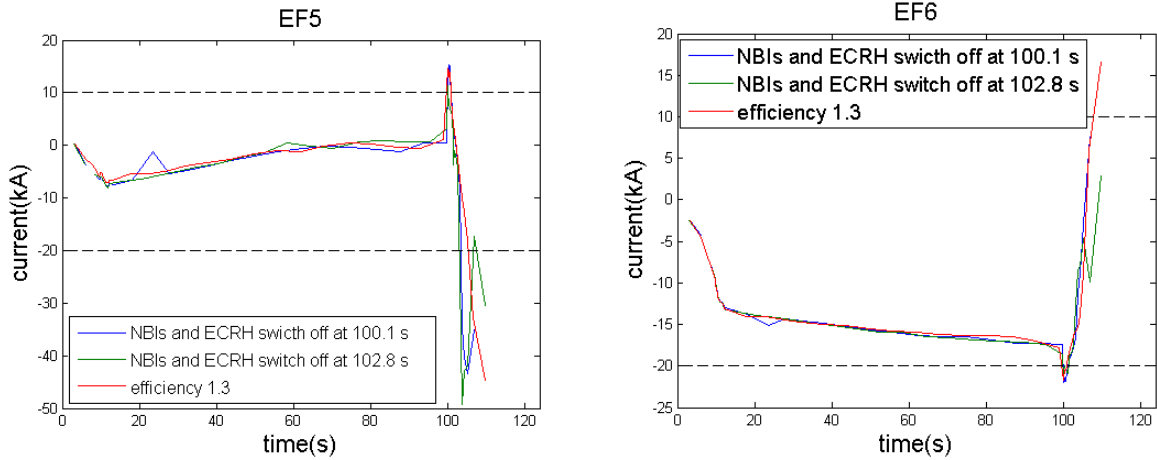


Figure 3.71 - Left: EF5 currents comparison. Right: EF6 currents comparison.

As it is possible to notice from the figures, an increase of the multiplication factor for N-NBI and ECRH current drive efficiency leads to a better behavior of coil currents, but it is not a controllable parameter. It is just assumed that, in view of the uncertainties in the physics models, some parameters could be considered as adjustable in the simulations. Therefore, this case shows a better convergence, in fact points of non-convergence are not present.

Moreover, in the cases in which the efficiency multiplication factor is set to 1, the peaks in EF3 and EF4 depend from the time at which the externals heating are switched off, while the peaks in EF5 and EF6 are due to the loss of the H-mode. Therefore, it is difficult to optimize the simulation in this respect and these peaks are still present for any value of the efficiency.

The continuous fluctuations during the ramp-down phase stress the need to make additional efforts to optimize this delicate phase.

In order to check if the scenario is well optimized, volume-averaged and central electron temperatures, volume-averaged and central electron densities are plotted in order to check if they sufficiently close to the typical values reported in table 3.6 (see figure 3.72 and 3.73).

Figures are referred to the case in which the ramp-up rate is set to 1.3 MA/s and the NBIs are switched off at 100 s.

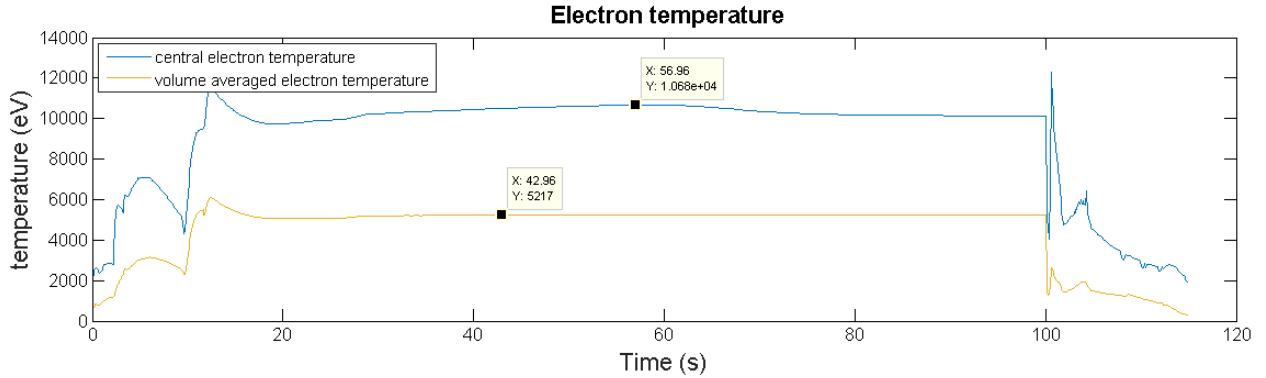


Figure 3.72 – The central electron temperature (blue line) taken as reference value in the Research Plan [17] is 13.5 KeV while the value of the volume averaged electron temperature (yellow line) is 6.3 KeV.

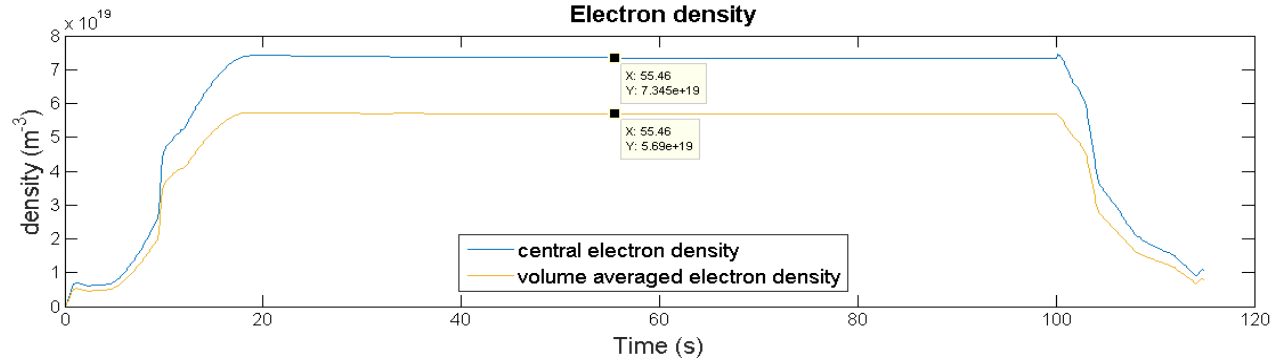


Figure 3.73 - The central electron density (blue line) taken as reference value in the Research Plan [17] is $7.7 \times 10^{19} \text{ m}^{-3}$, while the value of the volume averaged electron density (yellow line) is $5.6 \times 10^{19} \text{ m}^{-3}$.

The last step in the optimization process is to check the hoop forces, the vertical forces and the voltages generated in the coils through the plasma discharge. The figures from 3.74 to 3.78 report the results obtained by the FEEQS calculation. The hoop forces on coils are not sensitive to the efficiency changing, therefore they are plotted only once and they are valid for all the cases analyzed.

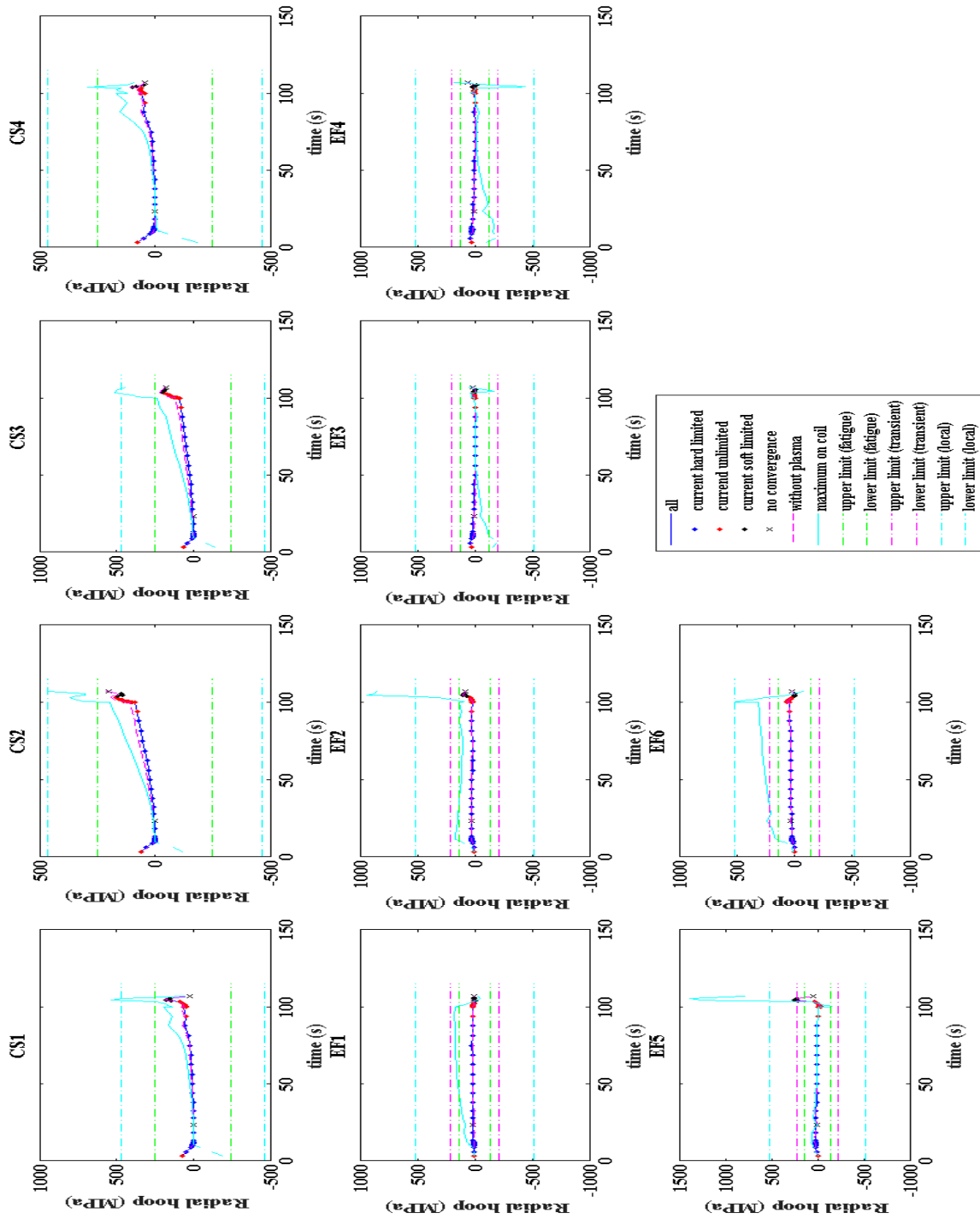


Figure 3.74 - Radial hoop forces computed by FEEQS using the case in which ECRH and NBIs are turned off at 100s. Green lines represent the upper and the lower limits on each coils. They are still valid for all the cases analyzed due to the weak sensitivity to changes in N-NBI and ECRH efficiency. All of the hoop forces are between the upper and the lower limits.

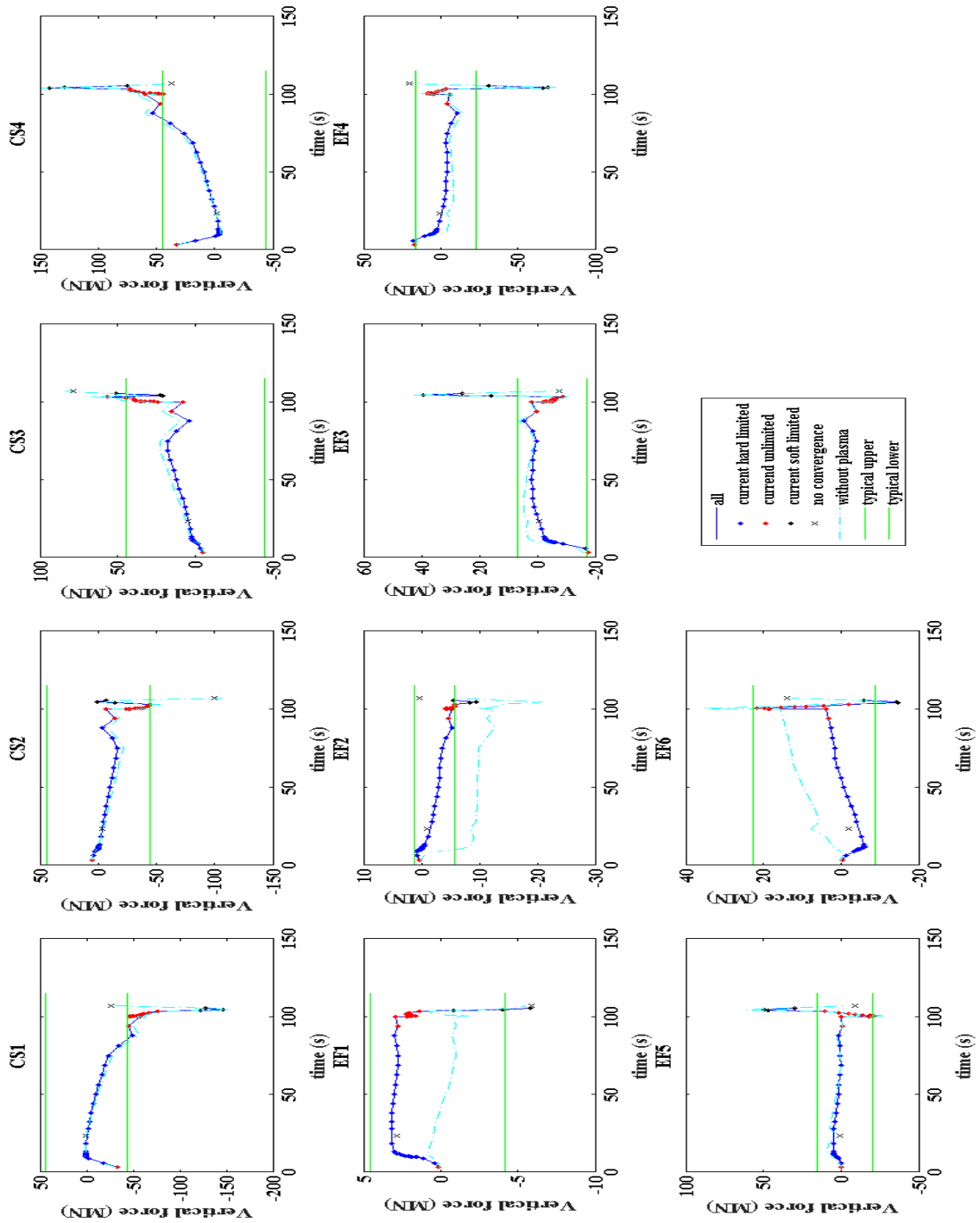


Figure 3.75 – Vertical forces computed by FEEQS using the case in which ECRH and NBIs are turned off at 100s. Green lines represent the upper and the lower typical values on each coils. Before the starting of the ramp-down phase, all the vertical forces are within the limits. The peaks in the last part are due to the loss of H-mode.

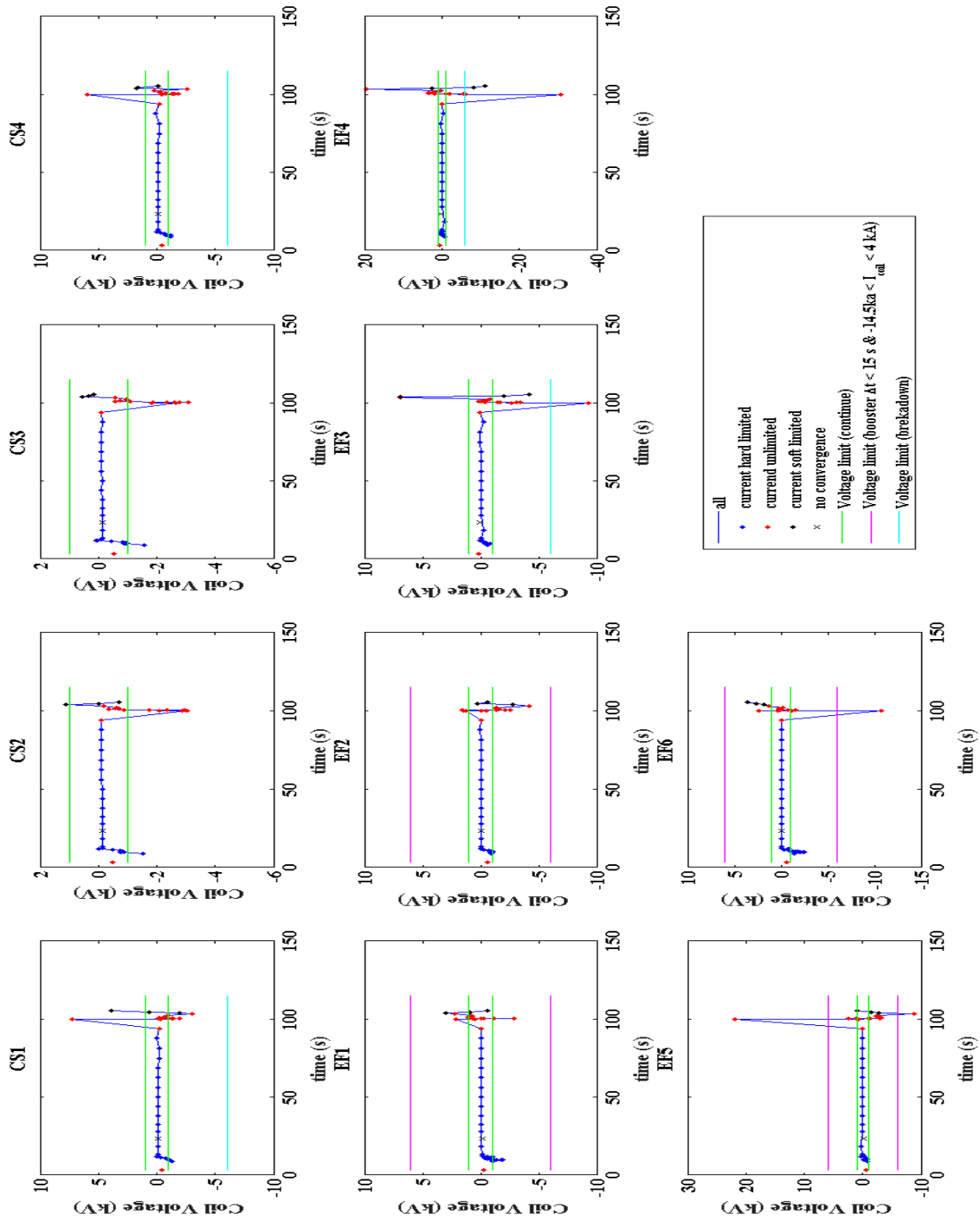


Figure 3.76 – Coil voltages computed by FEEQS using the case in which ECRH and NBIs are turned off at 100s. Green lines represent the upper and the lower limits on each coils. The first peaks are due to the reaching of H-mode, while the second peaks are due to the loss of the H-mode. During the flattop phase all the voltages applied to the coils lie between the limits.

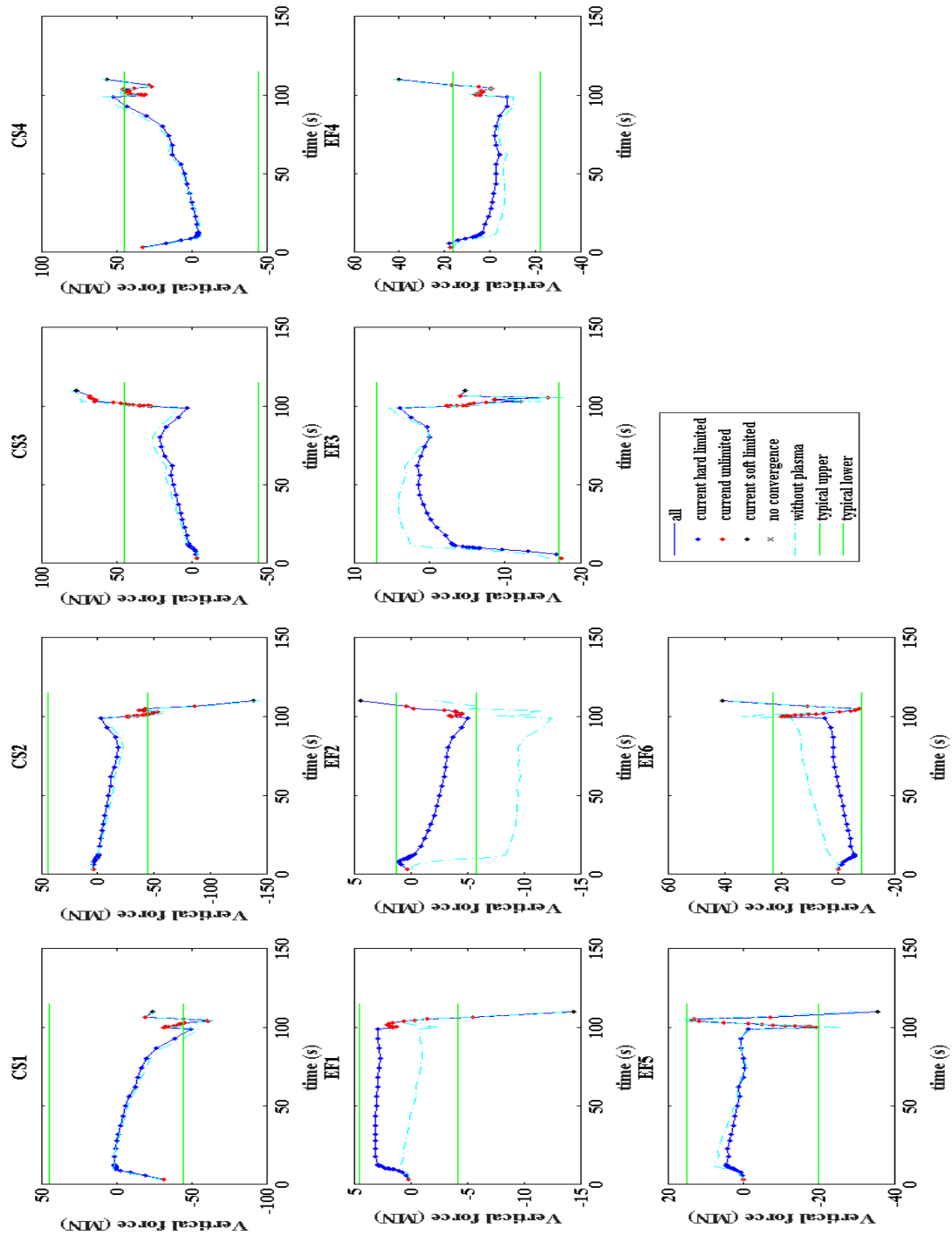


Figure 3.77 - Vertical forces computed by FEEQS using the case in which ECRH and NBIs are turned off at 100s and their efficiency are set to 1.3. Green lines represent the upper and the lower typical values on each coils. Before the starting of the ramp-down phase, all the vertical forces are within the limits. The peaks in the last part are lower with respect to the previous case.

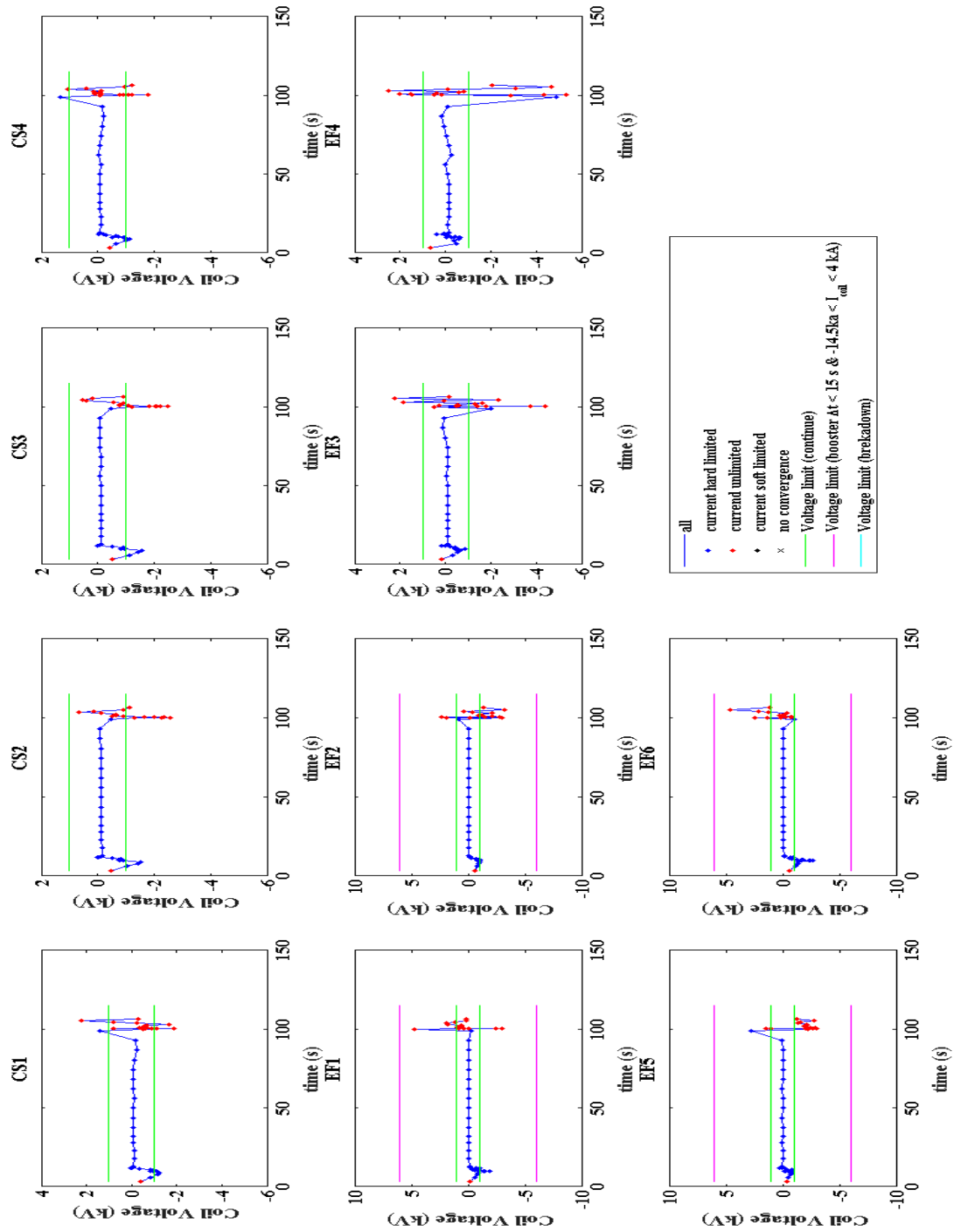


Figure 3.78 - Coil voltages computed by FEEQS using the case in which ECRH and NBIs are turned off at 100s and their efficiency is set to 1.3. Green lines represent the upper and the lower limits on each coils. The peaks are lower with respect to the previous case. During the flattop phase, all the voltages applied to the coils lie between the limits.

All the efforts done in order to reduce the peaks are useless, this means that they are related to the transition from H-mode to L-mode.

To conclude, both cases are well optimized up to the beginning of ramp-down. Of course, more efforts are needed to analyze the last phase of the plasma discharge in which the simulation becomes very sensitive to every change in parameters.

The optimization process is also useful to highlight which are the parameters that have the largest influence on the plasma and the currents behavior. Having established that the ECRH has to be used for the x-point formation and the N-NBI are necessary to assist the H-mode transition, the other fundamental parameters are the plasma current ramp-up rate and the parameters that regulate the transition to the H-mode. In fact, they are related to each other: in order to reach the H-mode as soon as possible, the ramp-up has to be quick. This leads to a lower flux consumption, but the currents and the forces generated into the coils could present some peaks or jumps. On the other hand, a lower ramp-up rate produces a bigger flux consumption and the coil current could exceed the limits. Another parameter that can be adjusted to prevent plasma disruptions is the line-averaged electron density. As the plasma behaves as a perfect gas, an increase of density leads to a decrease of temperature. Also the heating depositions have an important role. Moving the positions at which the external heatings are applied, the heat is able to diffuse into the plasma at different times and therefore, the plasma has different properties.

3.3.2 Scenario #4-2

Fully inductive operation scenario or standard H-mode scenario of ITER is necessary to demonstrate a fusion gain of 10 for 400s. However, inductive current drive uses magnetic flux variations, therefore the scenario is pulsed. In order to operate in steady-state or (even partially) non-inductively, other types of plasma scenario have been developed, which are known as advanced tokamak scenarios. To achieve the steady-state operation external current drive systems will be used, such as EC waves and NBI. However, plasma itself through the so-called bootstrap mechanism provides the main component of non-inductive current drive in advanced scenarios. This source of current drive is generated by the pressure gradients in the magnetic geometry of a tokamak and it is maximized at high plasma pressure and low plasma current. In the presence of a radial pressure gradient, adjacent trapped particle orbits provided a momentum imbalance that can be transferred to the passing particles by collisions. A large bootstrap fraction can be obtained increasing the normalized pressure. Therefore, the current can become hollow and the q profile can change from monotonic to a configuration with off-axis minimum q . This creates a zone of negative magnetic shear. To have a magnetic shear close to zero, the q profile has to be as flatter as possible. A core region of negative or reversed magnetic shear reduces turbulence and could produce an internal transport barrier (ITB) with temperature and density peaking. However, by varying the q profile shape, different types of plasma scenarios can be obtained. Experiments have focused on the development of two scenarios: non-inductive scenario for continuous operation and hybrid scenario for long pulse operation. [\[30\]](#)

The advanced scenario analyzed in this chapter is known as hybrid scenario for long pulse operation. In order to maximize the neutron fluence and, therefore, the fusion burn duration, a reduced plasma current and auxiliary current drive systems are needed to provide a significant fraction of non-

inductive current. A low current also provides an increase in bootstrap current fraction. The optimum current is expected to lie between that of the steady-state scenario and the baseline scenario, therefore this mode of operation is known as hybrid scenario. It is characterized by a value of q in the plasma core slightly above 1 with the magnetic shear close to zero (see figure 3.79).

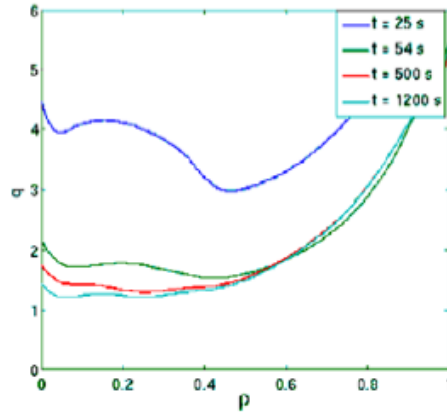


Figure 3.79 – q -profile time-slices computed by CRONOS. The LCFS is prescribed as a result of simulations performed for the ITER H-mode scenario. [31]

One of the benefits of this scenario consists of the low level or absence of sawtooth activity and related instabilities. Moreover, it is attractive because the impact of disruptions would be reduced due to the lower energy stored in the poloidal magnetic field. [28] The sawtooth oscillation is a periodic collapse phenomenon. It develops in the plasma core when the safety factor on-axis is below 1. In the core, the temperature and density ramp up slowly over most of the sawtooth period while they rapidly crash down in the remainder. In extreme cases, this may lead to a rapid termination of the plasma by disruption. [32]

Therefore, one major challenge is to sustain the safety factor profile over a long duration in a desired shape with $q > 1$ and with a wide zone of low magnetic shear in the core in order to avoid the ITBs formation and an high beta after H-mode transition, which could lead to deleterious MHD phenomena. [33]

An important role is played by the section ‘MHD and ITB’ in the section list of METIS parameters. First, the sawtooth model does not play a role any more, because the desired q profile should stay above 1. ITB with null or negative magnetic shear, rotation effect on ITB and ELMs are taken into account. [34]

Table 3.9 - Typical parameters of scenario #4-2.

Plasma current I_p (MA)	3.5
Toroidal magnetic field B_T (T)	2.28
Major radius R (m)	2.93
Minor radius a (m)	1.14
Flat-top duration (s)	100

N-NBI power (MW)	10
P-NBI power (MW)	20
ECRH power (MW)	7
Volumetric averaged electron temperature (KeV)	3.7
Central averaged temperature (KeV)	7.5
Volumetric averaged electron density (10E20/m³)	0.62
Line-averaged electron density (10E20/m³)	0.69
Central averaged electron density (10E20/m³)	0.84
H factor	1.2

In order to simulate this scenario, deuterium is used, the plasma current has to be of 3.5MA, the vacuum magnetic field is imposed to 2.28T as reported in table 3.9, the duration is set to 100s and full CS current is considered. In addition, the value of H_H factor (1.2), PNBI_N (10MW), PNBI_P (20MW) and PECCD (7MW) are chosen following the table 3.9. The breakdown and ITB formation are taken into account, while recycling and runaway effects are neglected. Matthews scaling law is considered to model the line radiative power in the core plasma and the LFCS electron temperature and density are computed using scaling law models. The value of the multiplication factor applied to edge density scaling law (edge_density_factor) is 1. All of the simulations have been made setting a high voltage in order to reduce the values of the two voltage peaks and setting the line-averaged density to $6.9 \times 10^{19} \text{ m}^{-3}$ that is the value reported in the table 3.9. Some simulation is carried out in order to determinate the value of ECRH power for assisted breakdown (PBREAK) and the maximum ECRH power at the end of the ramp-up (PRAMPUP). The first parameter is set to 0.1 MW because a higher value leads to a very large electron temperature at the beginning of the shot. The second one is set to 0 because the scenario has to have a fraction of non-inductive current drive of 0.58.

The plasma current ramp-up and ramp-down rate are chosen taking into account the consideration made for the scenario 2. In order to have the H-mode transition as soon as possible and a low flux consumption, the ramp-up is set to 1.9 MA/s and the ramp-down is set to 1.5 MA/s. The density peaking factor increases the pressure gradient and the bootstrap current, therefore it helps both to reduce the flux consumption and to delay the occurrence of the $q=1$ surface [31]. For this reason, the peaking factor is set to 1.5. As the scenario 2, ECRH is used to assist the x-point formation ($t=2.418 \text{ s}$) and N-NBI is used to reach the H-mode configuration. The ECRH deposition poloidal location is set to 90 and the ECRH deposition width is set to 0.2. The vertical shift at the center of the plasma of the neutral beam trajectory is set to 0.35 and tangency radius of NBIs are imposed to 2.85. The current drive efficiency multiplication factor of N-NBI and of ECRH are set to 1.3. A very important parameter is the ECRH radial deposition position waveform, which is set in order to keep the q factor above 1 and its waveform is reported in figure 3.80.

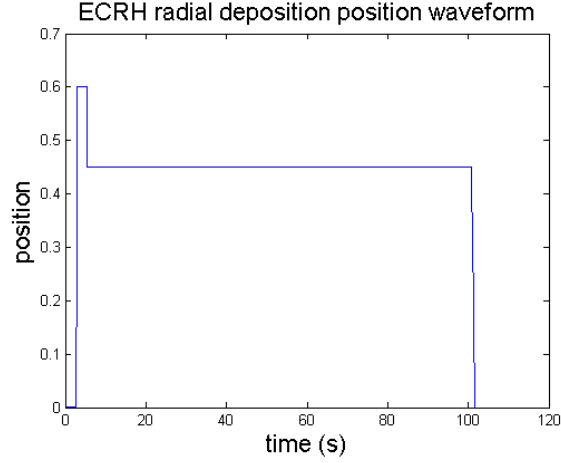


Figure 3.80 - ECRH radial deposition position for ramp-up rate of 1.9 MA/s.

Also for this scenario it is possible to switch off the NBIs at $t=100$ s, in order to avoid damage to the first wall, or at $t=104$ s in order to prevent plasma disruptions.

At this point FEEQS is used to compute the coil currents generated into the magnets. The code shows problems of convergence probably due to the value of density peaking and to the ramp-up rate. In order to keep the density peaking factor constant, another simulation is carried out using the same parameters of the previous one, but the plasma current ramp-up rate is set to 1.5 MA/s. Also in this case there is a problem of convergence. Therefore, the density peaking is shifted to the value 1.3. For this case there are no problems of convergence using the FEEQS code. The figures from 3.81 to 3.84 show the input parameters used to optimize the scenario. Also for this scenario, two final solutions have been chosen. In the first case the P-NBI and N-NBI are switched off at 105.1 s, in order to avoid plasma disruption. In the second case, NBIs are turned off at 100 s and this leads to a plasma disruption.

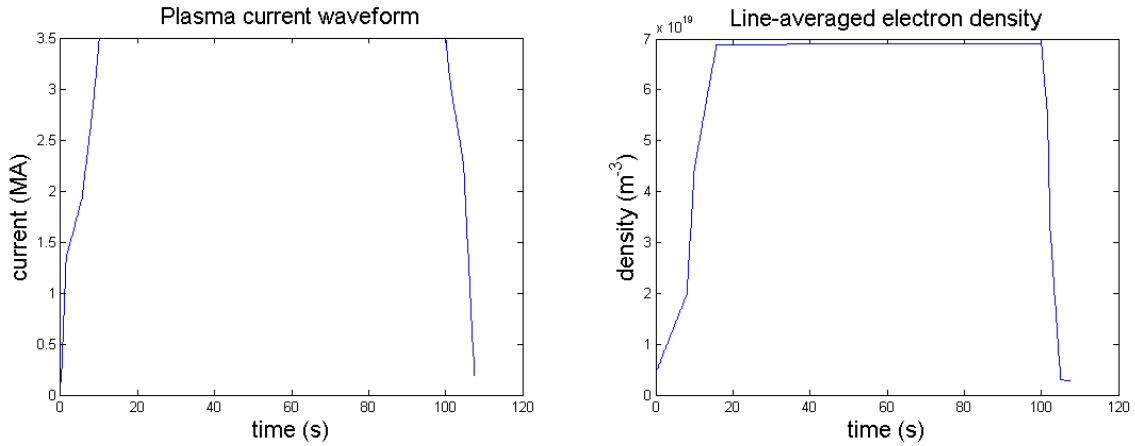


Figure 3.81 - Left: plasma current waveform input. Right: line-averaged electron density waveform input.

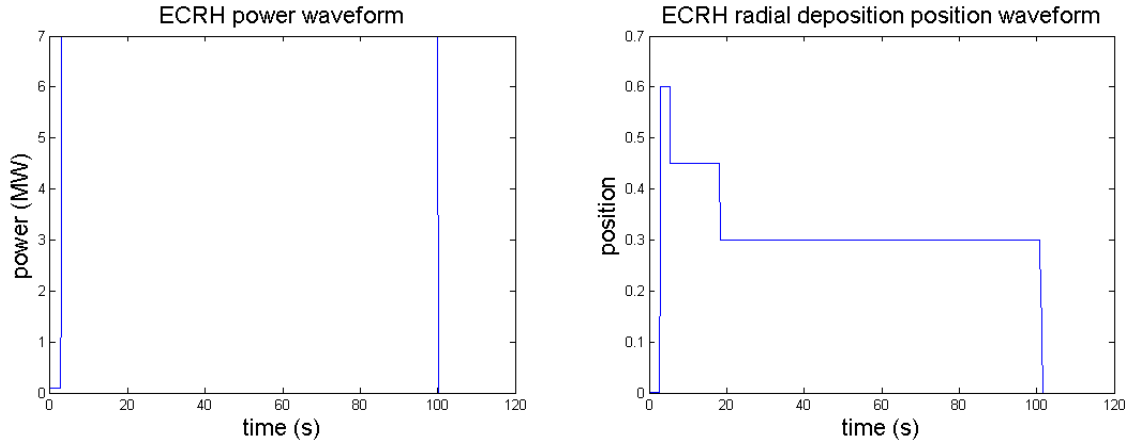


Figure 3.82 - Left: ECRH power deposition position waveform input. Right: ECRH power waveform input.

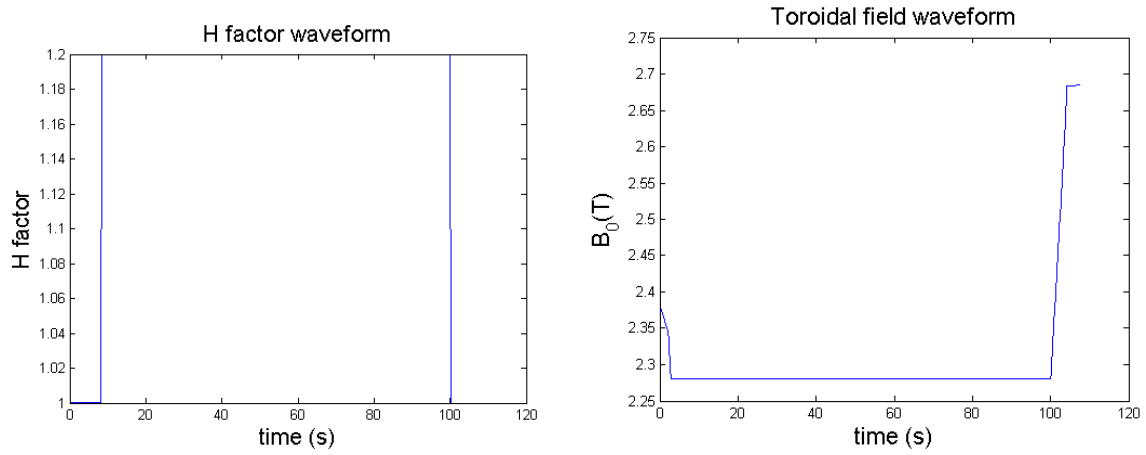


Figure 3.83 - Left: H factor waveform input. Right: toroidal field waveform input.

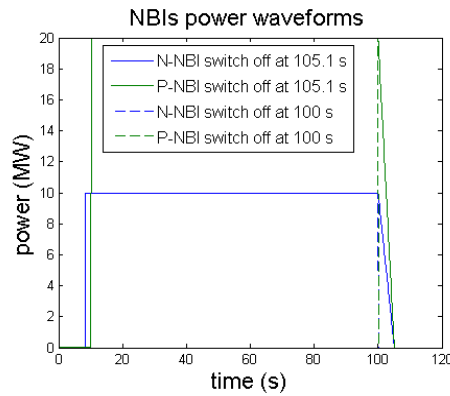


Figure 3.84 - NBIs waveforms inputs for both case. In first case, NBIs are switched off at 105.1 s in order to avoid the disruption; in the second case, NBIs are switched off at 100 s in order to avoid possible damage to the first wall.

In order to better understand the following figures, table 3.10 reports the main times of the discharge.

Table 3.10 – Main times of simulation.

	Time (s)
X-point	3.227
End of ramp-up	10.043
ECRH switch-on	2.74
N-NBI and P-NBI switch-on	8.343/10.14
H-mode transition	8.343
End of flattop/L-mode transition	100
End of ramp-down	108

In the two cases the coil currents are computed using FEEQS, then the new LCFs are uploaded in METIS and the codes are run again. In all the runs, the flux offset is fixed in manual mode with value 7 Wb and regulation weight is 10^{-15} . The last configuration of coil currents are plotted in the following figures (from 3.85 to 3.89) in order to stress the differences between the three cases.

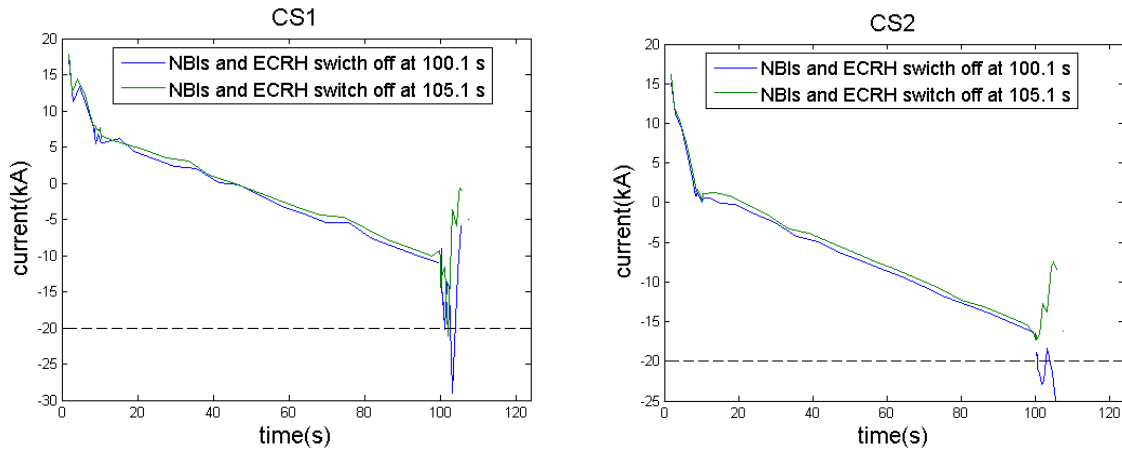


Figure 3.85 - Left: CS1 currents comparison. Right: CS2 currents comparison.

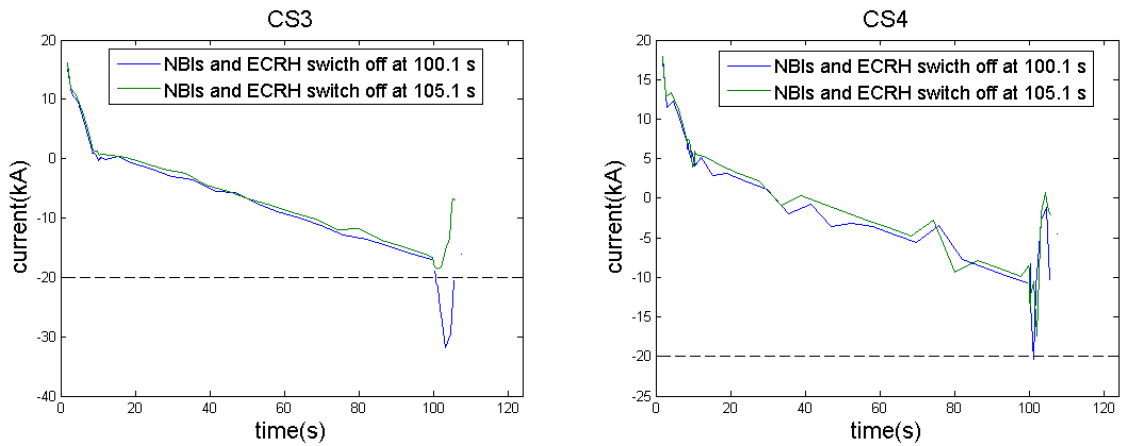


Figure 3.86 - Left: CS3 currents comparison. Right: CS4 currents comparison.

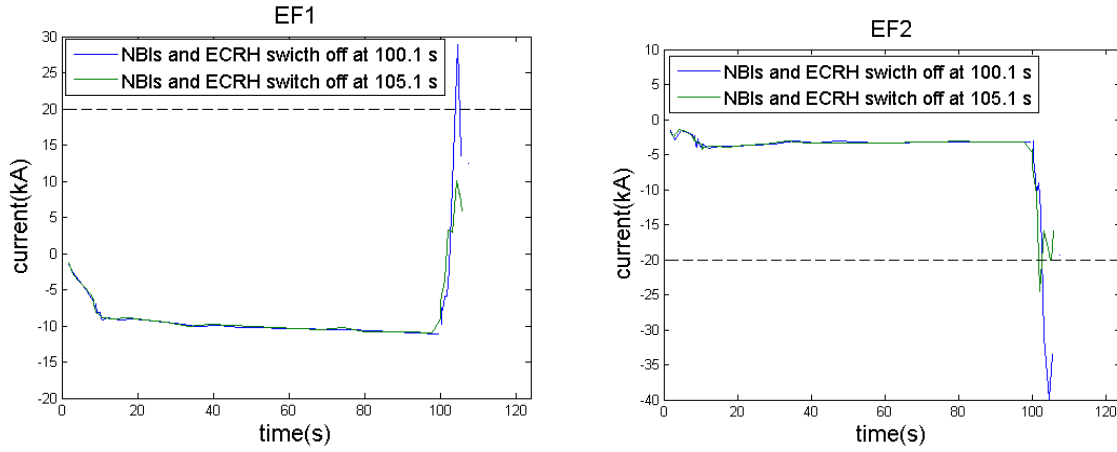


Figure 3.87 - Left: EF1 currents comparison. Right: EF2 currents comparison.

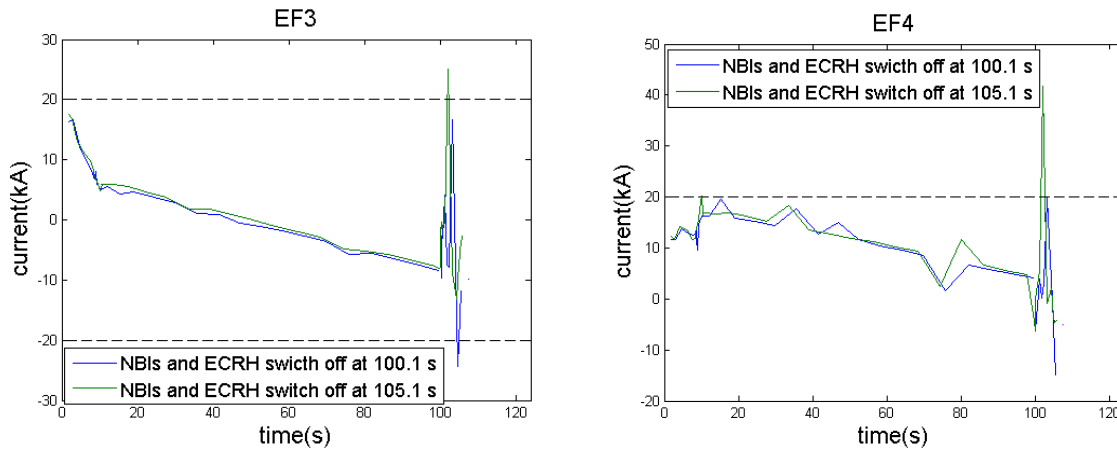


Figure 3.88 - Left: EF3 currents comparison. Right: EF4 currents comparison.

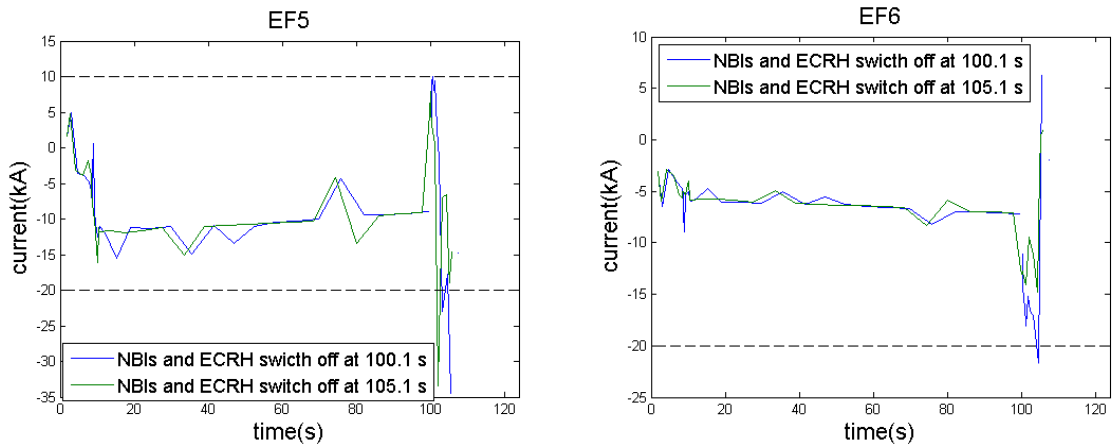


Figure 3.89 - Left: EF5 currents comparison. Right: EF6 currents comparison.

The case in which the NBIs are switched off at 105.1 s shows a better behavior of coil current in CS, especially for the ramp-down phase, in fact all the currents are contained in the limits. Moreover, this case does not present plasma disruptions during the shot. Nevertheless, some damages to the first

wall have to be considered due to the NBIs that could heat the wall once the plasma starts moving down.

Figures from 3.90 to 3.92 show the hoop forces, the vertical forces and the voltages applied on coils and computed by FEEQS. For both cases the results computed for the case in which the NBIs are switched off at 105.1 s are reported, because the computed behavior of forces and voltages are very similar. As it is possible to notice, all the radial hoop forces and the vertical forces are between the limits, excepted for some points belonging to the ramp-down phase. Concerning the voltage applied to the coils, some peaks are present due to the H and L-mode transition.

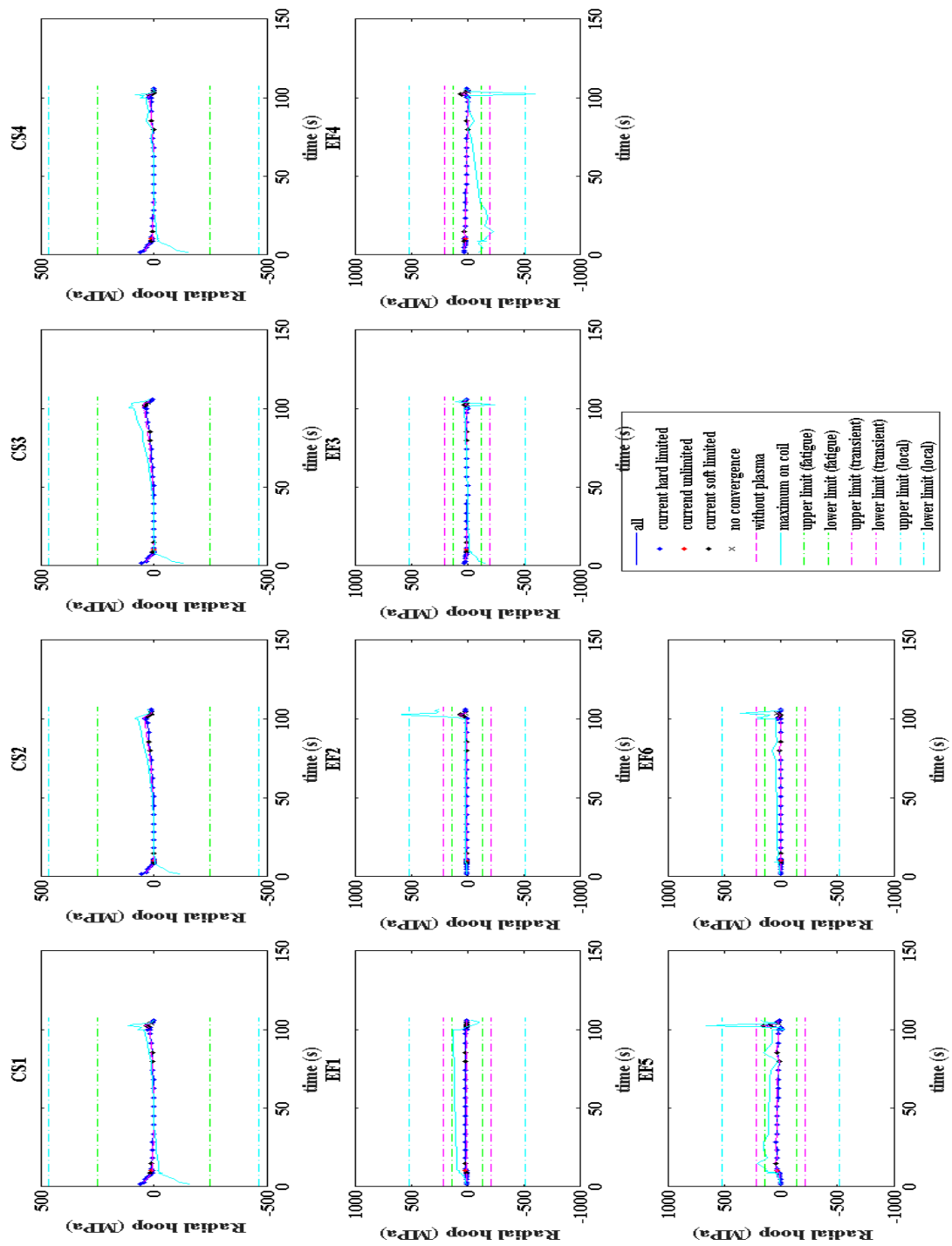


Figure 3.90 - Radial hoop forces computed by FEEQS using the case in which NBIs are turned off at 105.1 s. Green lines represent the upper and the lower limits on each coils. They are still valid for both cases analyzed due to the weak sensitivity to changes in NBIs and ECRH switching off. All of the hoop forces are between the upper and the lower limits.

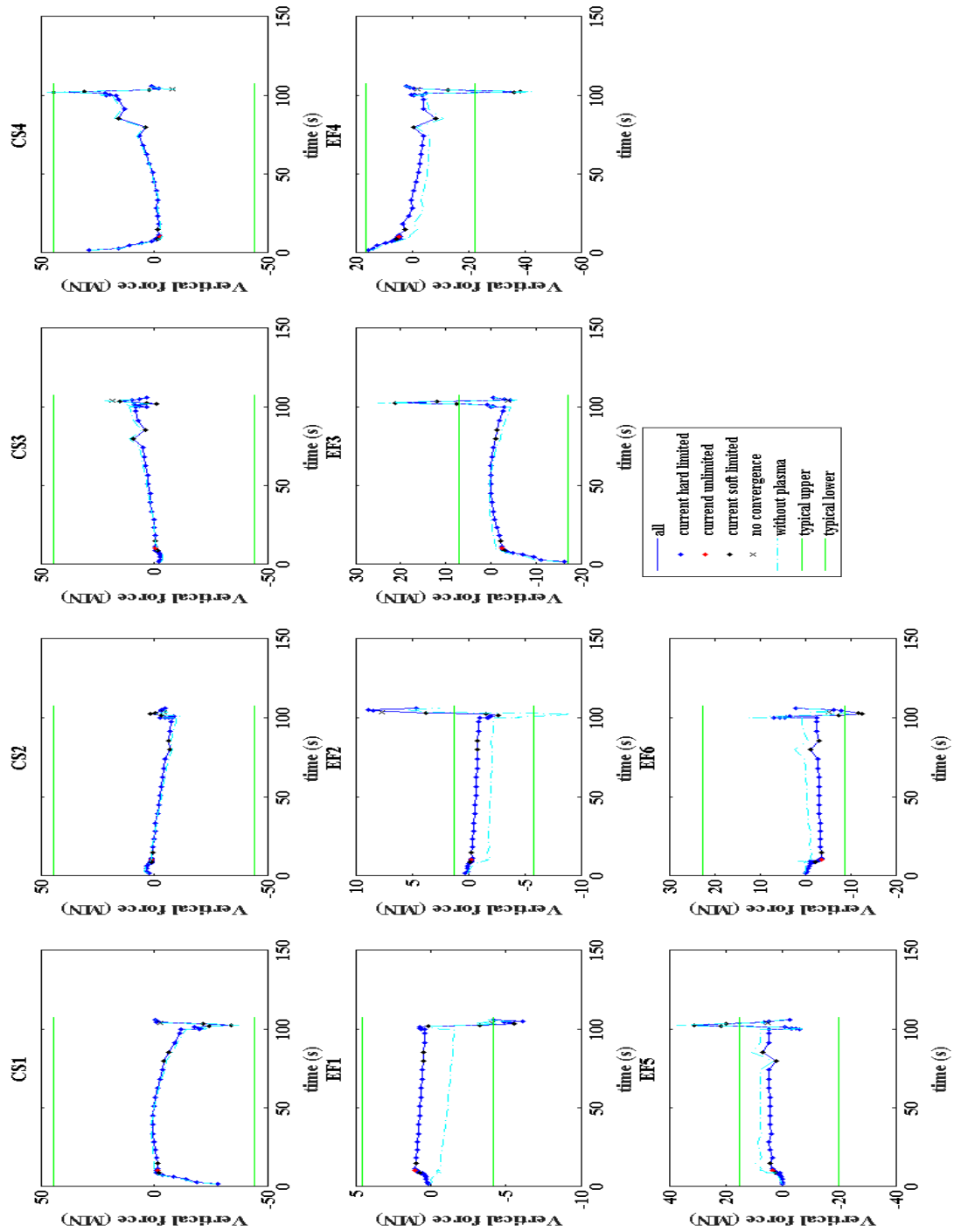


Figure 3.91 - Vertical forces computed by FEEQS using the case in which NBIs are turned off at 105.1 s. Green lines represent the upper and the lower typical values on each coils. Before the starting of the ramp-down phase, all the vertical forces are within the limits. The peaks in the last part are due to the loss of H-mode.

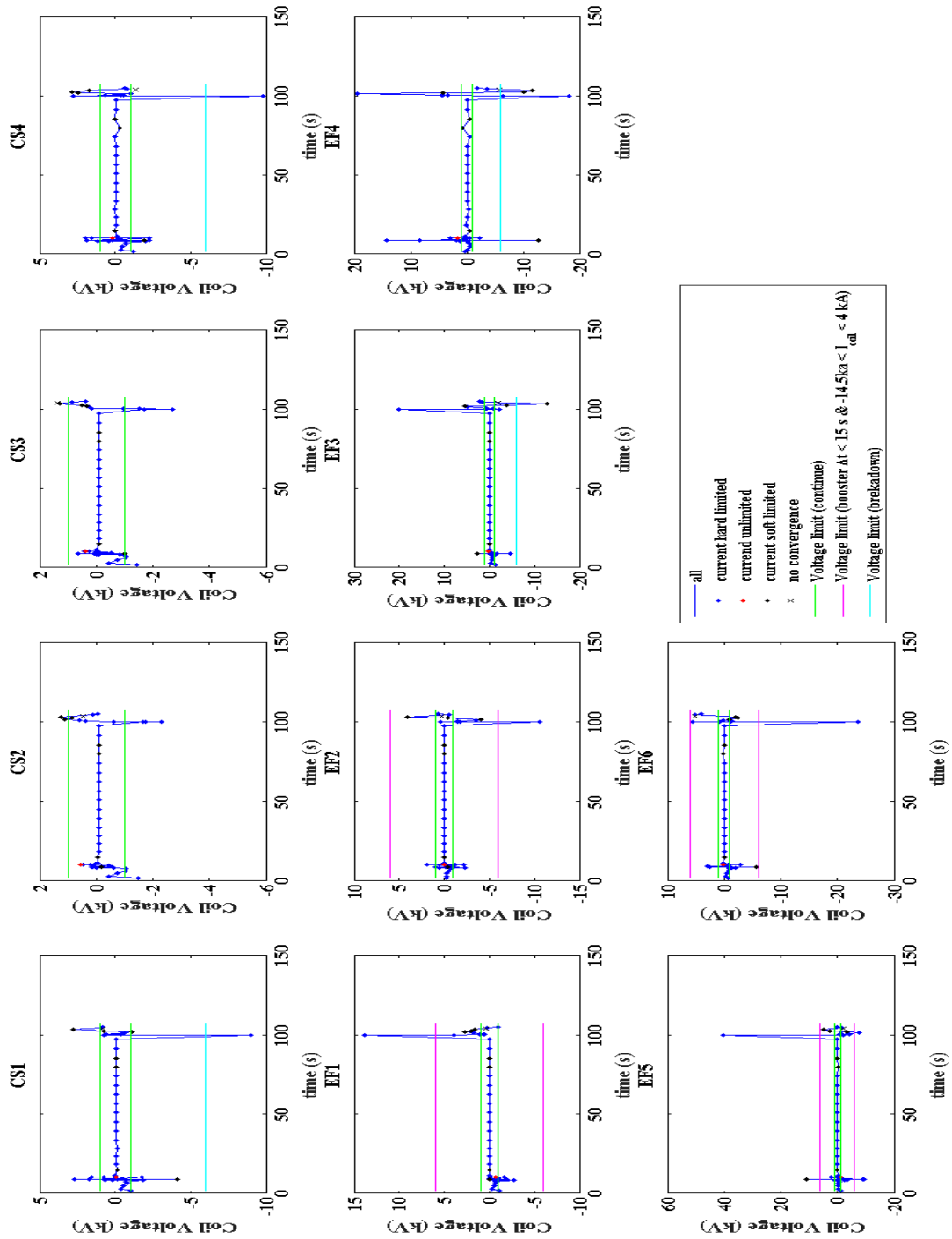


Figure 3.92 - Coil voltages computed by FEEQS using the case in which NBIs are turned off at 105.1 s. Green lines represent the upper and the lower limits on each coils. The first peaks are due to the transition to H-mode, while the second peaks are due to the loss of the H-mode. During the flattop phase all the voltages applied to the coils lie between the limits.

For this scenario it is important to check that the bootstrap current fraction (bootstrap current/plasma current) and the non-inductive fraction (non-inductively driven current/plasma current) are close to the target values of 0.4 and 0.58, respectively. In order to show it, the bootstrap current (blue line), the ECRH driven current (yellow line), the NBI driven current (green line), the total non-inductively driven current (red line) and the plasma current (orange line) are plotted in figure 3.93.

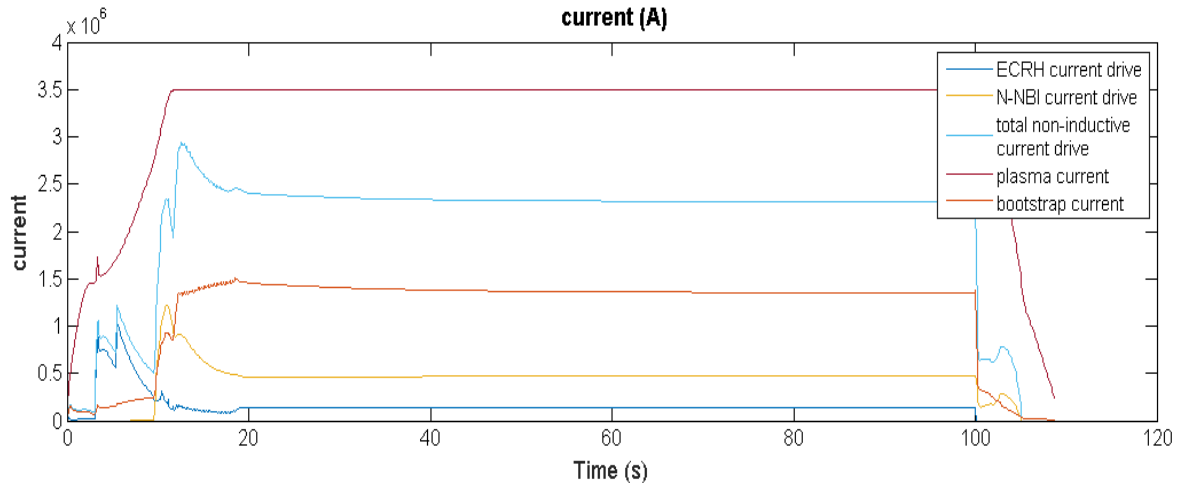


Figure 3.93 – The orange line is the bootstrap current, the blue line is the ECRH drive current, the yellow line is the N-NBI drive current, the cyan line is the total non-inductively drive current and the red line is the plasma current.

The fraction of bootstrap current is about 0.4 and non-inductive fraction is about 0.66. Therefore, the expected values for the scenario #4-2 are obtained.

As for the scenario #2, volume-averaged and central electron temperature, volume-averaged and central electron densities are plotted in order to compare them to the expected values reported in table 3.9 (see figure 3.94 and 3.95).

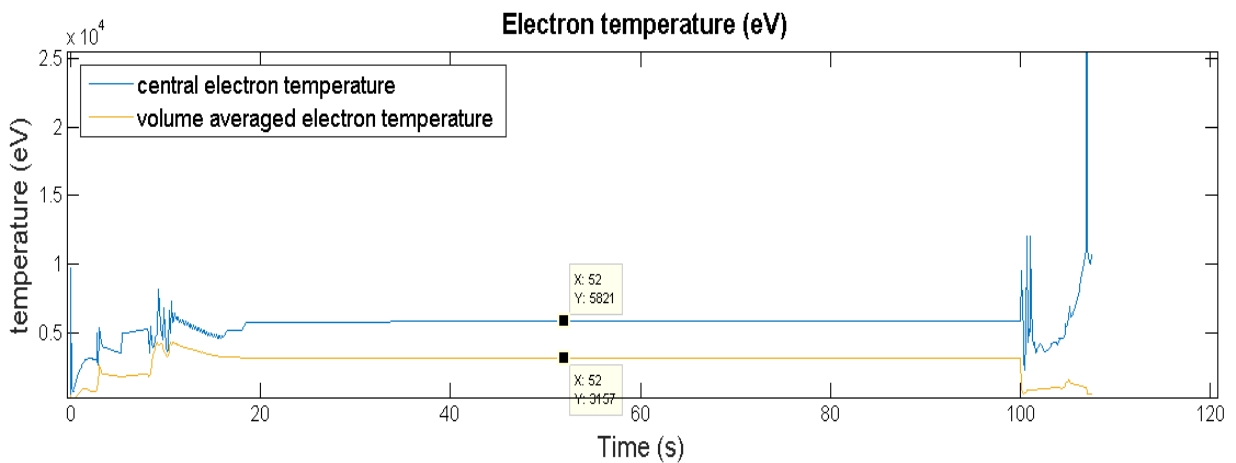


Figure 3.94 - The central electron temperature (blue line) taken as reference value into the Research Plan [\[17\]](#) is 7.5 KeV while the value of the volume averaged electron temperature (yellow line) is 3.7 KeV.

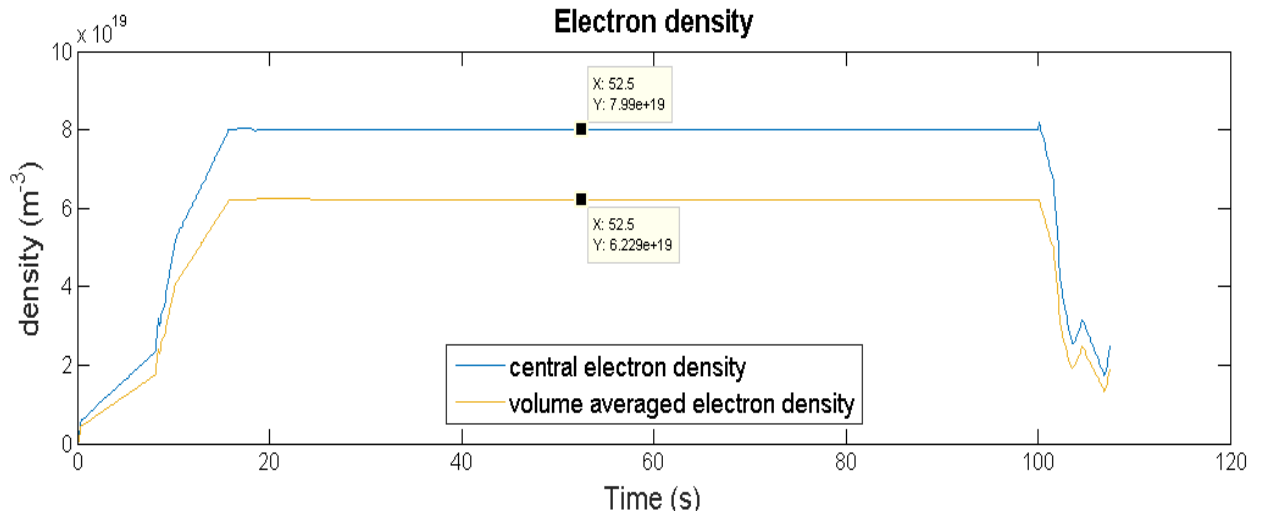


Figure 3.95 - The central electron density (blue line) taken as reference value into the Research Plan [17] is $8.4 \times 10^{19} \text{ m}^{-3}$, while the value of the volume averaged electron density (yellow line) is $6.2 \times 10^{19} \text{ m}^{-3}$

Finally, also the q factor has to be checked, its profile being a distinctive feature of the hybrid scenario. Figure 3.96 shows the q factor behavior at time 3.225 s (after x-point formation), 8.6 s (H-mode transition), 11.87 s, 33.697 s and 91.308 s.

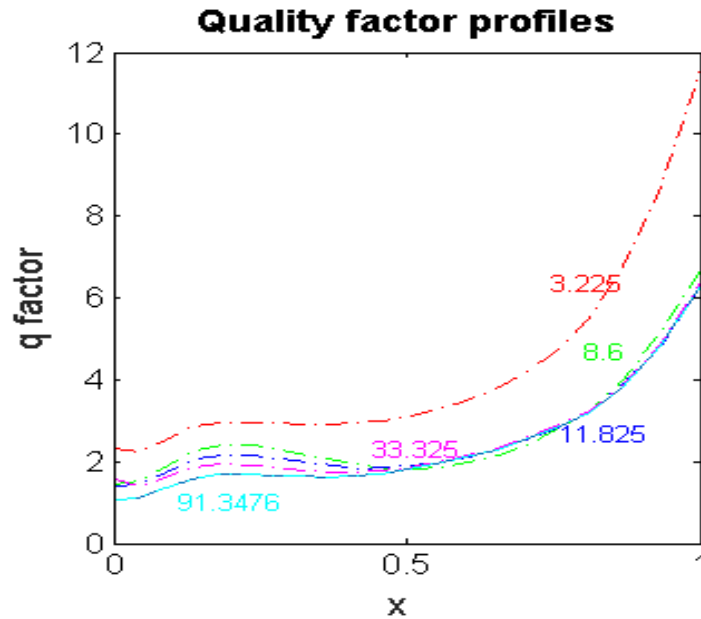


Figure 3.96 - q factor profile at 3.225 s (after x-point formation, red line), 8.6 s (H-mode transition, green line), 11.87 s (blue), 33.697 s (magenta line) and 91.308 s (cyan line).

The scenario is well optimized since the q factor value is always above 1, therefore sawtooth formation is avoided.

In order to try to reduce the voltage peaks, the same simulation parameters are used but with a ramp-up rate of 1.3MA/s. This attempt does not show particular advantages, therefore the peaks are due

to the reaching and the loss of the H-mode. The peaks are higher than those generated in scenario #2, a plausible reason is that in the hybrid scenario higher values of β_N and β_P are reached, therefore a fast transition to a very low beta might exceed the coil voltage limits.

For this scenario the same parameters play a fundamental role. It is important to reach as soon as possible a certain fraction of non-inductive current in order to drive profiles that generate a large fraction of bootstrap current. For this reason, the current ramp-up rate has to be quick. In this way also a flat or weakly reversed q profile is obtained rapidly. This helps to avoid the formation of ITBs after the transition to the H-mode. It is also important to reach the H-mode before the end of the current ramp-up in order to have a q profile flat in the core. Therefore, ECRH and N-NBI injections have to assist the ramp-up. As already mentioned, the density peaking factor is a key parameter and it has to be as high as possible in order to increase the pressure gradient and therefore the bootstrap current. Finally, the ECRH radial deposition position has to be adjusted in order to obtain a q value always above 1. Heating and driving current at different radial positions, the heat and current density diffuse differently and this leads to q profile changing. In order to keep it flat and as near as possible to 1, radial deposition is shifted progressively toward the plasma center.

4. Conclusions

The objectives of this work of thesis are multiple. How the different plasma parameters affect the plasma discharge was analyzed with the purpose to optimize two of the operational scenarios of JT-60SA. In order to achieve that, two different codes are used together for the first time. It means that the validation of their combination is an essential step to have feasible plasma scenarios. From the computational results obtained, it is possible to conclude that:

- FEEQS code used in inverse magnetostatic mode is able to make a static analysis of residual transverse magnetic field. Therefore, running it, it is possible to define the plasma breakdown area, the maximum value of magnetic field and the coil current distribution in the pre-magnetization phase;
- FEEQS results (without coupling with METIS) match well TOSCA data, which means that the two codes have the same contents and similar accuracy. Therefore, it is possible to conclude that the difference in the coil currents is due to the difference in plasma shape and in P' and in FF' plasma profiles. This highlights how much the plasma discharge is sensitive to the geometrical plasma parameters and to radial profiles of plasma quantities. Therefore, developing a coupled system of codes, such as METIS-FEEQS, is well motivated and is expected to yield a much more accurate description of the plasma discharges;
- From section 3.3 is possible to underline several aspects:
 - Parameters reported in Ref [\[17\]](#) are achievable, therefore the two scenarios analyzed are expected to be feasible;
 - The plasma current ramp-up rate is the most sensitive parameter in the plasma discharge since it is responsible to the x-point formation and the H-mode transition. It is also related to the flux consumption that is needed to ensure a plasma discharge duration of 100 s;
 - The external heatings are used in order to help the x-point formation and the H-mode transition, in order to reduce as possible the voltage and coil currents. As a consequence, also the forces and the stresses on coils are reduced;
 - The radial deposition position of the auxiliary heating plays an important role especially for the scenario #4-2. In this case, this parameter is adjusted in order to obtain the desirable q shape.

Moreover, this kind of analysis is also useful to understand the points of the computation that could be improved. It is possible to summarize them as follows:

- More efforts are needed to better analyze the ramp-down phase. This part of the plasma discharge is the most sensitive to change parameters. Moreover, a controlled plasma is essential in order to reduce the disruption occurrence and to avoid possible damage on the machine;
- The very beginning of the simulation is not accurately described, therefore, this stresses the need of detailed modelling to have a more precise simulation of the breakdown phase;
- So far, the only way to match the current diffusion LCFS poloidal flux computed by METIS with the LCFS poloidal flux computed by FEEQS is to set manually the value of the flux offset. Therefore, a code improvement could consist of finding a model to make this part automatic.

- This point is important to match automatically the upper coils current limits with the coils current corresponding to the first time slice that the code is able to compute;
- A next step in the development of a combined simulator is to couple CREATE-NL and METIS in order to simulate a full tokamak discharge. Using as constraint the METIS prediction for plasma current, I_i and β_p , CREATE-NL provides the last closed flux surface shape to METIS for the flattop and allows closed-loop simulations by a set of appropriate controllers.

Bibliography

- [1] A. Pironti and M. Walker, "Control of Tokamak Plasmas", IEEE Control Systems Magazine, pp. 24-29. Oct. 2005.
- [2] https://en.wikipedia.org/wiki/Thorium-based_nuclear_power
- [3] EFDA, Fusion Electricity, "A roadmap to the realization of fusion energy", 2012
- [4] European Research Roadmap to the Realization of Fusion Energy, 2018
- [5] Alexander Zerrahn, Wolf-Peter Schill, Claudia Kemfert. "On the economics of electrical storage for variable renewable energy sources". In: European Economic Review 108 (2018) 259–279.
- [6] Annette Evans, Vladimir Strezov, Tim J. Evans. "Assessment of utility energy storage options for increased renewable energy penetration". In: Renewable and Sustainable Energy Reviews 16 (2012) 4141– 4147.
- [7] <https://www.iea.org/topics/nuclear/>
- [8] G. De Tommasi¹, R. Albanese¹, G. Ambrosino¹, M. Ariola², P.J. Lomas³, A. Pironti¹, F. Sartori⁴ and JET EFDA contributors. "Plasma Current, Position and Shape Control in Tokamak. Proc. 22nd IAEA Fusion Energy Conference, Geneva, Switzerland (2008)
- [9] A. Pironti and M. Walker, "Fusion, Tokamaks and Plasma Control", IEEE Control Systems Magazine, pp. 30-43. Oct. 2005.
- [10] Jure Maglica. "Plasma heating with neutral beam injection". University in Ljubljana Faculty of mathematics and physics Department of physics.
- [11] Hyeon K. Park. "Role of Radio Frequency and Microwaves in Magnetic Fusion Plasma Research". In: Journal of Electromagnetic Engineering and Science 2017;17(4):169-177.
- [12] J. Blum, C. Boulbe, B. Faugeras. "Reconstruction of the equilibrium of the plasma in a Tokamak and identification of the current density profile in real time". In: Journal of Computational Physics 231 (2012) 960–980; doi:10.1016/j.jcp.2011.04.005.
- [13] G. Giruzzi, M. Yoshida, J.F. Artaud, Ö. Asztalos, E. Barbato, P. Bettini, A. Bierwage, A. Boboc, T. Bolzonella, S. Clement-Lorenzo, S. Coda, N. Cruz, Chr. Day, G. De Tommasi, M. Dibon, D. Douai, D. Dunai, M. Enoeda, D. Farina, L. Figini, M. Fukumoto, K. Galazka, J. Galdon, J. Garcia, M. Garcia-Muñoz, L. Garzotti, C. Gil, C. Gleason-Gonzalez, T. Goodman, G. Granucci, N. Hayashi, K. Hoshino, S. Ide, R. Imazawa, P. Innocente, A. Isayama, K. Itami, E. Joffrin, Y. Kamada, K. Kamiya, Y. Kawano, H. Kawashima, T. Kobayashi, A. Kojima, H. Kubo, P. Lang, Ph. Lauber, E. de la Luna, P. Maget, G. Marchiori, S. Mastrostefano, G. Matsunaga, M. Mattei, D.C. McDonald, A. Mele, Y. Miyata, S. Moriyama, A. Moro, T. Nakano, R. Neu, S. Nowak, F.P. Orsitto, G. Pautasso, B. Pégourié, L. Pigatto, A. Pironti, P. Platania, G.I. Pokol, D. Ricci, M. Romanelli, S. Saarelma, S. Sakurai, F. Sartori, H. Sasao, M. Scannapiego, K. Shimizu, K. Shinohara, J. Shiraishi, S. Soare, C. Sozzi, W. Stępniewski, T. Suzuki,

Y. Suzuki, T. Szepesi, M. Takechi, K. Tanaka, D. Terranova, M. Toma, H. Urano, J. Vega, F. Villone, V. Vitale, T. Wakatsuki, M. Wischmeier, R. Zagórski. "Physics and operation oriented activities in preparation of the JT-60SA tokamak exploitation". In: Nuclear Fusion **57**, 085001.

[14] G. Ambrosino and R. Albanese. "Magnetic Control of Plasma Current, Position and Shape in Tokamaks", IEEE Control Systems Magazine, pp. 76-92. Oct. 2005.

[15] Y. Liang and JET EFDA contributors. "Overview of Edge Localized Modes Control in Tokamak Plasmas". Proc. 22nd IAEA Fusion Energy Conference, Geneva, Switzerland (2008).

[16] H. Shirai, P. Barabaschi, Y. Kamada and the JT-60SA Team. "Recent progress of the JT-60SA project". In: Nuclear Fusion **57**, 102002.

[17] JT-60SA Research Plan, Sept. 2018, www.jt60sa.org/pdfs/JT-60SA_Res_Plan.pdf

[18] J.F. Artaud, V. Basiuk, F. Imbeaux, M. Schneider, J. Garcia, G. Giruzzi, P. Huynh, T. Aniel, F. Albajar, J.M. Ané, A. Bécoulet, C. Bourdelle, A. Casati, L. Colas, J. Decker, R. Dumont, L.G. Eriksson, X. Garbet, R. Guirlet, P. Hertout, G.T. Hoang, W. Houlberg, G. Huysmans, E. Joffrin, S.H. Kim, F. Köchl, J. Lister, X. Litaudon, P. Maget, R. Masset, B. Pégourié, Y. Peysson, P. Thomas, E. Tsitrone and F. Turco. "The CRONOS suite of codes for integrated tokamak modelling". In: Nucl. Fusion **50** (2010), 043001 (25pp).

[19] T. Takeda and S. Tokuda. "Computation of MHD Equilibrium of Tokamak Plasma". In: journal of computational physics **93**, 1-107 (1991).

[20] J.F. Artaud, F. Imbeaux, J. Garcia, G. Giruzzi, T. Aniel, V. Basiuk, A. Bécoulet, C. Bourdelle, Y. Buravand, J. Decker, R. Dumont, L.G. Eriksson, X. Garbet, R. Guirlet, G.T. Hoang, P. Huynh, E. Joffrin, X. Litaudon, P. Maget, D. Moreau, R. Nouailletas, B. Pégourié, Y. Peysson, M. Schneider and J. Urban. "Metis: a fast integrated tokamak modelling tool for scenario design". In: Nucl. Fusion **58** (2018) 105001 (25pp).

[21] J. Blum, H. Heumann, E. Nardon, X. Song. "Automating the design of tokamak experiment scenarios". In: Journal of Computational Physics, volume 394, 1 October 2019, pages 594-614.

[22] M. Gaël SELIG. "équilibre évolutif à frontière libre et diffusion résistive dans un plasma de tokamak". PhD. Thesis. Université Nice Sophia Antipolis. 20 décembre 2012.

[23] C. Johnson. Numerical Solution of Partial Differential Equation by the Finite Element Method. Mineola, New York, 2009.

[24] A. Quarteroni, F. Saleri and P. Gerasio. Scientific Computing with MATLAB and Octave. Springer Heidelberg New York Dordrecht London, 2014.

[25] Holger Heumann, Jacques Blum, Cedric Boulbe, Blaise Faugeras, Gael Selig, et al.. "Quasistatic Free-Boundary Equilibrium of Toroidal Plasma with CEDRES++: Computational Methods and Applications". In: Journal of Plasma Physics, Cambridge University Press (CUP), 2015, pp.35.

[26] M. MATSUKAWA, T. TERAOKA, K. YAMAUCHI, K. SHIMADA, P. CARA, E. GAI, L. NOVELLO, A. FERRO, R. COLETTI, M. Santinelli and A. COLETTI. "Optimization of Plasma Initiation Scenarios in JT-60SA". In: J. Plasma Fusion Res. SERIES, Vol. 9 (2010).

[27] H. Urano, T. Fujita, S. Ide, Y. Miyata, G. Matsunaga, M. Matsukawa. “Development of operation scenarios for plasma breakdown and current ramp-up phases in JT-60SA tokamak”. In: Fusion Engineering and Design 100 (2015) 345–356.

[28] https://en.wikipedia.org/wiki/Tikhonov_regularization

[29] L. Garzotti, E. Barbato, J. Garcia, N. Hayashi, I. Voitsekhovitch, G. Giruzzi, P. Maget, M. Romanelli, S. Saarelma, R. Stankiewicz, M. Yoshida and R. Zagórski. “Analysis of JT-60SA operational scenarios”. In: Nucl. Fusion 58 (2018) 026029 (13pp).

[30] E. Joffrin and JET EFDA contributors. “Advanced Tokamak Scenario Developments for the Next Step”, Proc. 21st IAEA Fusion Energy Conference, Chengdu, China (2006).

[31] K. Besseghir, J. Garcia, J.-F. Artaud, F. Imbeaux, R. R. Khayrutdinov, J. B. Lister, V. E. Lukash and P. Maget. “Achieving and sustaining advanced scenarios in ITER modelled by CRONOS and DINA-CH”. In: Plasma Phys. Control. Fusion 55 (2013) 125012 (25pp).

[32] T.C. Luce, C.D. Challis, S. Ide, E. Joffrin, Y. Kamada, P.A. Politzer, J. Schweinzer, A.C.C. Sips, J. Stober, G. Giruzzi, C.E. Kessel, M. Murakami, Y.-S. Na, J.M. Park, A.R. Polevoi, R.V. Budny, J. Citrin, J. Garcia, N. Hayashi, J. Hobirk, B.F. Hudson, F. Imbeaux, A. Isayama, D.C. McDonald, T. Nakano, N. Oyama, V.V. Parail, T.W. Petrie, C.C. Petty, T. Suzuki, M.R. Wade, the ITPA Integrated Operation Scenario Topical Group Members and Experts, the ASDEX-Upgrade Team, the DIII-D Team, JET EFDA Contributors and the JT-60U Team. “Development of advanced inductive scenarios for ITER”. In: Nucl. Fusion 54 (2014) 013015 (15pp).

[33] T. Fujita and the JT-60 team. “Steady state operation research in JT-60U with extended pulse length”. In: Nucl. Fusion 46 (2006) S3–S12.

[34] G. Papp, G. I. Pokol, G. Por, A. Magyarkuti, N. Lazanyi, L. Horvath, V. Igochine, M. Maraschek and ASDEX Upgrade Team. “Low frequency sawtooth precursor activity in ASDEX Upgrade”. In: Plasma Phys. Control. Fusion 53 (2011) 065007 (17pp).

Acknowledgments

I would like to thank the IRFM institute for making possible the experience just ended and for giving me the possibility of having a professional improvement and personal growth. In particular, I would like to express my sincere gratitude to my advisor Jean-Francois Artaud for having followed me throughout my training and for his constant availability. A special thanks to Dr. Gerardo Giruzzi for having included me in the internship project, for helping me in all the difficulties, for sharing his scientific knowledge with me and for being an important point of reference for my training. I would like to thank all the people in the lab who made pleasant my six months of work in a totally unknown environment. A special thanks to the "Italian group" for not making me feel the lack of home.

I would like to express my deep gratitude to Professor Fabio Subba for his advice, assistance and for his useful and constructive recommendations on this project.

I would like to thank Giorgio for having always been close to me during these six months, especially in times of greatest difficulty, for having endured all my complaints and all my problems. Specially, I am grateful to him for having believed in me more than I believe in myself. A special thanks for having taught me to face everything with more serenity, to risk more often and to have let me out of my "comfort zone".

Thanks to my "Turin family", in particular to Selenia, Riccardo, Daniele and Beppe, for having been part of my university career once again, for encouraging me to undertake this course and for having been present morally even at a long distance.

Finally, sincere thanks to my true family, always present (sometimes too much) and always available. Thank you for satisfying any wish I had, for accepting all my choices and for letting me to bang freely my head everywhere. For helping me to get up always, for having taken part in every steps of my life, for giving me confidence, for never having underestimated my capabilities. My biggest fear has been to disappoint you and I hope that my course up to now will make you proud of me.

Ringraziamenti

Vorrei ringraziare l'istituto IRFM per aver reso possibile l'esperienza appena conclusa e per avermi dato la possibilità di un'importante crescita lavorativa e personale. In particolare vorrei ringraziare il mio tutor Jean-Francois Artaud per avermi seguito durante tutto il mio percorso e per la sua costante disponibilità. Un ringraziamento speciale al Dr. Gerardo Giruzzi per avermi inserito nel progetto di stage, per avermi aiutata in tutte le difficoltà, per aver condiviso con me le sue conoscenze scientifiche e per essere stato un punto di riferimento importante del mio percorso. Vorrei ringraziare tutte le persone del laboratorio che hanno reso piacevoli i miei sei mesi di lavoro in un ambiente totalmente sconosciuto. Un ringraziamento speciale al "gruppo degli italiani" per non avermi fatto sentire la mancanza di casa.

Vorrei esprimere la mia profonda gratitudine al professor Fabio Subba per i suoi consigli, assistenza e per le sue raccomandazioni utili e costruttive su questo progetto.

Vorrei ringraziare Giorgio per essermi stato sempre vicino in questi sei mesi, soprattutto nei momenti di maggiore difficoltà, per aver sopportato ogni mio lamento e ogni mio problema. Ma, soprattutto per aver creduto in me più di quanto ci creda io stessa. Un grazie particolare per avermi insegnato ad affrontare tutto con più serenità, a osare più spesso e avermi fatto uscire dalla mia "comfort zone".

Un ringraziamento alla mia "famiglia torinese", in particolare a Selenia, Riccardo, Daniele e Beppe, per aver fatto parte ancora una volta della mio percorso universitario, per avermi spronato a intraprendere questo percorso e per essere stati moralmente presenti anche a distanza.

Infine, un ringraziamento sincero alla mia vera famiglia, sempre presente (a volte anche troppo) e sempre disponibile. Grazie per aver assecondato ogni mio desiderio, aver accettato ogni mia scelta e per avermi lasciata libera di sbattere la testa ovunque. Per avermi aiutato a rialzarmi, sempre, per esserci stati in ogni tappa fondamentale della mia vita, per avermi dato fiducia, per non aver mai sottovalutato le mie capacità. La mia paura più grande è sempre stata quella di potervi deludere e spero che il mio percorso fatto fin'ora vi renda fieri di me.